

Incoherent Scatter Measurements  
of E- and F-Region Density, Temperatures,  
and Collision Frequency  
at Millstone Hill

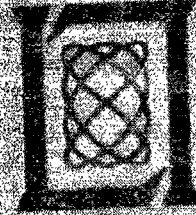
W. L. Oliver  
J. E. Salah  
R. H. Wand  
J. V. Evans

23 February 1979

Sponsored by the National Science Foundation  
Grant Number ATM 782107

## Lincoln Laboratory

MASSACHUSETTS INSTITUTE OF TECHNOLOGY  
LINCOLN, MASSACHUSETTS



## ABSTRACT

The Millstone Hill incoherent (Thomson) scatter radar system has been operated since 1963 to perform a synoptic study of F2-region electron densities, and electron and ion temperatures. These measurements have been conducted by transmitting single long pulses and performing digital sweep integration and spectrum analysis of the reflected signals. This report describes changes made to the system in 1969 to permit extensions of the measurements to altitudes below 200 km (i.e., the E- and F1-regions). These changes include modifications to the radar timing equipment to permit the transmission of close-spaced pairs of pulses from which the echo autocorrelation function can be determined in the computer by processing appropriately spaced pairs of echo samples. By operating the radar coherently, it has also been possible to subtract the unwanted (stronger) clutter signals from the ionospheric echoes. Samples are presented of the results that can now be obtained from these programs.

# CONTENTS

Abstract	iii
Symbols and Abbreviations	vi
I. INTRODUCTION	1
II. OPERATING MODES	5
A. General	5
B. Mode E	5
C. Mode F	5
D. Mode G	10
E. Mode H	10
F. Mode I	10
G. Observing Program	11
H. Mode Modifications	11
III. EQUIPMENT	21
A. General	21
B. Frequency Control	21
C. Receiver	25
D. Data Sampling	25
E. Timing Equipment	26
IV. OPERATING PROCEDURE	29
A. Equipment Timing Control	29
1. Transmitter Control - Mode E	29
2. Transmitter Control - Mode F	29
3. Transmitter Control - Mode G	36
4. Transmitter Control - Mode H	36
5. Transmitter Control - Mode I	37
6. Transmitter Modulator Control	37
7. Receiver Control	37
8. Data-Sampling Control	39
B. Real-Time Computer Operations	39
1. General	39
2. Computer Operations - Mode E	41
3. Computer Operations - Mode F	44
4. Computer Operations - Mode G	46
5. Computer Operations - Mode H	47
6. Computer Operations - Mode I	47
C. Real-Time Computer Output	48
1. General	48
2. Computer Output - Modes E and I	48
3. Computer Output - Mode F	49
4. Computer Output - Modes G and H	49

V. ANALYSIS	53
A. General	53
B. Power-Profile Analysis	53
1. Mode E - Routine Analysis	53
2. Mode E - RASEM Analysis	55
3. Mode I	56
C. Correlation-Function Analysis	58
1. General	58
2. Phase Analysis	58
3. Magnitude Analysis - Library Search	59
4. Ion-Composition Problem	61
5. Collisional Region - $h < 118$ km	63
6. Temperature Equality Region - $118 < h < 130$ km	63
7. Ion-Composition Transition Region - $130 < h < 225$ km	65
8. $O^+$ Region - $225$ km $< h$	65
D. Neutral-Atmosphere Deductions and Ion-Composition Profile	65
1. General	65
2. $T_n$ , [O] Profile	65
3. Ion-Composition Profile	66
4. Electron-Density-Profile Corrections	67
E. Debye-Length Corrections	68
Acknowledgments	69
References	70
APPENDIX A - Systematic Distortions in Correlation-Function Measurements	71
APPENDIX B - Statistical Errors in Correlation-Function Measurements	79

## SYMBOLS AND ABBREVIATIONS

$A^*$	complex conjugate of complex number $A$
$A*B$	convolution of $A$ and $B$
$ A $	magnitude of complex number $A$
$[A]$	concentration (number density, density) of gas species $A$
$[A]_x$	$[A]$ at altitude $x$ in kilometers
acf	autocorrelation function
$c$	speed of light in free space
$f$	frequency
$f_0$	radar center frequency
$h$	altitude (height) above the earth's surface
$\text{Im}(A)$	imaginary part of complex number $A$
$k$	Boltzmann's constant
$m_e$	electron mass
$m_i$	ion mass
$N_e$	electron density
$\text{Re}(A)$	real part of complex number $A$
$S/N$	signal-to-noise ratio
$T$	pulse length
$T_e$	electron temperature
$T_i$	ion temperature
$T_n$	neutral temperature
$T_\infty$	exospheric temperature
$T_{120}$	$T_n$ at $h = 120$ km
$V_d$	drift velocity
$\Delta h$	height resolution
$\lambda$	radar wavelength
$\nu_{in}$	ion-neutral collision frequency
$\tau$	correlation lag

INCOHERENT SCATTER MEASUREMENTS OF E- AND F-REGION  
DENSITY, TEMPERATURES, AND COLLISION FREQUENCY  
AT MILLSTONE HILL

I. INTRODUCTION

This report is intended to complement an earlier one<sup>1</sup> that described the manner in which the Millstone Hill, Westford, Massachusetts (42.6°N, 71.5°W) vertically directed incoherent (Thomson) scatter radar system is operated for studies of the F2-region. These studies commenced in 1963 and have provided synoptic measurements of F-region electron density and electron and ion temperatures.<sup>2</sup> The results obtained during 1963 through 1970 have been published in earlier Lincoln Laboratory Technical Reports as well as in a number of journal articles, as listed in Table I.

These F2-region studies have been conducted using single long pulses together with echo-power sweep integration performed in a digital computer. The height resolution  $\Delta h$  afforded by the measurements is determined by the pulse length  $T$  according to

$$\Delta h = cT/2 \quad (1)$$

where  $c$  is the speed of light. Adequate height resolution can be achieved for electron-density measurements by reducing  $T$  to a suitable value. However, the determination of the electron and ion temperatures  $T_e$  and  $T_i$  requires a spectrum analysis of the signals, and this places constraints on the pulse length that may be used. The overall doppler broadening of the signals is approximately  $3\Delta f_i$  (Ref.9), where

$$\Delta f_i = \frac{1}{\lambda} \sqrt{\frac{8kT_i}{m_i}} \quad (2)$$

is the doppler shift produced by an ion of mass  $m_i$  approaching a radar at its mean thermal speed,  $k$  is Boltzmann's constant, and  $\lambda$  is the radar wavelength. In order to recover most of the information on the frequency spectrum of the returns, it is necessary that the spectral width of the pulse ( $\sim 1/T$ ) be restricted to about one-fifth to one-sixth of the overall doppler broadening. Thus, the minimum acceptable pulse length is

$$T_{\min} > 2/\Delta f_i \quad (3)$$

As discussed in Ref.9, this restriction on the minimum useful pulse length limits the range of altitudes over which single long-pulse observations provide adequate height resolution for measurements of electron and ion temperatures. For the 68-cm-wavelength vertically directed radar system, this useful range is approximately  $250 \leq h \leq 1000$  km depending upon ionospheric conditions. In order to extend the measurements to lower altitudes, one may reduce the wavelength (thereby increasing  $\Delta f_i$ ) and/or make the measurements at oblique incidence. Using a fully steerable 23-cm-wavelength radar operated with the beam directed obliquely, it has been possible to achieve a height resolution of 35 km and extend the measurements to cover the altitude range  $130 \leq h \leq 260$  km approximately. Using this radar, information has been obtained on the transition between the molecular ions ( $O_2^+$ ,  $NO^+$ ) in the E-region and atomic ions ( $O^+$ ) in the F-region, and on horizontal drifts in the E- and F-regions; these results are published in the papers listed in Table II.

TABLE I  
PUBLICATIONS CONCERNING THE MILLSTONE HILL UHF  
(68-cm WAVELENGTH) THOMSON SCATTER RESULTS

Year	Months Covered	Publication
1963	March, July, August, September December, April, July, November February 1963 to January 1964	Ref. 3 Ref. 4 Technical Report 374, Lincoln Laboratory, M.I.T. (22 January 1965), DDC AD-616607
1964	April, July, November January through December	Ref. 5 Technical Report 430, Lincoln Laboratory, M.I.T. (15 November 1967), DDC AD-668436
1965	January, April, August January through December	Ref. 6 Technical Report 474, Lincoln Laboratory, M.I.T. (8 December 1969), DDC AD-707501
1966	January through December	Ref. 7; Technical Report 481, Lincoln Laboratory, M.I.T. (19 January 1971), DDC AD-725742
1967	January through December	Ref. 7; Technical Report 482, Lincoln Laboratory, M.I.T. (22 July 1971), DDC AD-735727
1968	January through December	Technical Report 499, Lincoln Laboratory, M.I.T. (23 January 1973), DDC AD-767251/2
1969	January through December	Ref. 8; Technical Report 513, Lincoln Laboratory, M.I.T. (23 July 1974), DDC AD-A008505/0
1970	January through December	Technical Report 522, Lincoln Laboratory, M.I.T. (11 May 1976)

TABLE II PUBLICATIONS CONCERNING THE MILLSTONE HILL L-BAND (23-cm WAVELENGTH) THOMSON SCATTER RESULTS	
Period Covered	Publication
April-November 1964	Ref. 10
October 1965 - May 1968	Ref. 11
September 1968 - September 1969	Ref. 12
November 1968 - September 1969	Ref. 13

Unfortunately, the sensitivity of the L-band radar system is barely adequate for oblique-incidence Thomson scatter measurements, and useful data can be gathered only during the daytime. Therefore, we have sought to obtain information on the E- and F1-regions employing the vertical-incidence radar. As outlined in Ref. 9, this may be achieved by transmitting pairs of pulses of length  $T$  separated by an interval  $\tau$  and measuring the correlation between pairs of echo samples taken with the same separation. This approach is routinely employed at the incoherent scatter radar stations located at Jicamarca, Peru, and at Arecibo, Puerto Rico.<sup>9</sup> Using this scheme, the height resolution can be set via Eq.(1) to any desired value subject only to limitations imposed by S/N considerations. The spectrum resolution is set independently by the maximum spacing between the pulses.

This 2-pulse technique has now been implemented at Millstone Hill, permitting measurements of density and temperature at altitudes between about 90 and 600 km with far better height resolution than could be achieved before. This report describes the Millstone Hill 2-pulse incoherent scatter program as it existed from its implementation in November 1969 through December 1975. A major hardware modification (addition of a hard-wired correlator) in January 1976 necessitated some changes to the 2-pulse program. These modifications will be the subject of a future report.

Section II of this report describes the various modes of operation of the 2-pulse experiments and their purposes for ionospheric measurement. In Sec. III, the modifications to the original 1-pulse radar equipment needed for operation in the 2-pulse modes are discussed. Section IV describes equipment timing and computer operations performed upon the received signals. The analysis procedures applied to the data to derive physical results are presented in Sec. V.

All 2-pulse analysis results are available on request to outside users. A program exists for producing contour plots of the various physical parameters (altitude-time contours), but it has not been applied to the data on a routine basis.



## II. OPERATING MODES

### A. GENERAL

The goal of the 2-pulse experiments is to gain improved height resolution in the bottomside ionosphere, where height gradients become larger and scale heights smaller compared with those encountered at greater heights. A number of experiments – designated Modes E, F, G, H, and I – have been devised for this purpose, each designed to probe efficiently a specific altitude range for specific experimental purposes. Table III lists the altitude ranges, measurements, and other characteristics for these modes, while Figs. 1(a) through (c) give more detailed information on the acf measurements; this table and the figures are referenced frequently in the following sections.

Modes E and I are designed to study electron density; hence, they measure scattered-power profiles. Modes F, G, and H are designed to study ionospheric temperatures, motions, collision frequencies, and composition; hence, they measure the acf of the scattered power. The magnitude of the acf yields the temperature, collision frequency, and composition information while the phase provides plasma drift information. Each mode has been designed to probe with a height resolution comparable to the local ionospheric scale height. The acf measurements are designed to extend out to at least the second zero-crossing of the function (except at lower altitudes where collisions severely smear the correlation function). This is needed in order to include a first zero-crossing and minimum of the function, from which considerable information is derived.

All measurements below about 160 km altitude (E, F, and I Modes) are contaminated with ground-clutter echoes, which are reflections from neighboring mountains entering through the antenna sidelobes. Removal of these echoes is necessary, and is accomplished by filtering digitally those returns which are stationary for a period of several milliseconds – a time long enough for ionospheric scatter to decorrelate completely, but short enough such that the clutter path length does not vary appreciably due to variation of the atmospheric refractive index. We do not believe that perfect clutter subtraction is achieved in practice owing to slight phase path length variations; tests suggest that 99 percent of the total clutter signal is normally removed.

The following sections discuss these new Modes E through I in more detail, and indicate the manner in which they have been used in experimental programs.

### B. MODE E

Mode E is designed to yield a complete ionospheric E- and F-region profile of electron density.

A 100- $\mu$ sec pulse is used, giving a height resolution  $\Delta h = 15$  km. The sample interval varies from 6 km at the lower altitudes to 15 km at the higher altitudes (Table III); samples with less than 15-km spacing, however, are not independent.

### C. MODE F

Mode F is designed to yield profiles of electron and ion temperatures  $T_e$  and  $T_i$  in the vicinity of the ionospheric E-region, and also a profile of ion-neutral collision frequency  $\nu_{in}$  in the lower part of that region. Due to the need for clutter subtraction, the calculation of the imaginary part of the correlation function is omitted to avoid doubling the integration time. All

TABLE III  
OPERATING MODES AND THEIR FUNCTIONS

Mode	Altitude Range* (km)	Sample Interval (km)	Height Resolution† (km)	Measurement	Range of Spacing‡ $\tau$ ( $\mu\text{sec}$ )	Step Interval $\Delta\tau$ ( $\mu\text{sec}$ )	Clutter Subtraction
E	92 to 176	6	15	Total power	NA	NA	Yes No No
	176 to 347	9	15				
	347 to 677	15	15				
F	106 to 124	3 <sup>§</sup>	6 <sup>§</sup>	Real part of correlation function	0 to 380	20	Yes Yes
	124 to 166	6	6 to 12				
G	167 to 317	15	15 to 27	Complex correlation function	0 to 380	20	No
H	215 to 515	30	30 to 42	Complex correlation function	0 to 190	10	No
I	56 to 140	1.5	3	Total power	NA	NA	Yes

\* Slightly different altitude ranges apply for data collected prior to December 1971: add 10 km to all altitudes in Mode E, -2 km in Mode G, and 0 km in Mode H.

† Height resolution is a function of lag - see Fig. 1.

‡ The maximum lag measured is a function of altitude - see Fig. 1.

§ A 6-km sample interval and 6- to 12-km height resolution apply for data taken before 30 December 1970.

TIME-BASE DELAY* (msec)	CENTER HEIGHT† (km)	$\tau$ ( $\mu$ sec)																			
		0	20	40	60	80	100	120	140	160	180	200	220	240	260	280	300	320	340	360	380
0.74	106	•	•	•	•	•	•	•	•	•	•	•	•	•	•	•	•	•	•	•	•
0.76	109‡	AS ABOVE																			
0.78	112	AS ABOVE																			
0.80	115‡	AS ABOVE																			
0.82	118	AS ABOVE																			
0.84	121‡	AS ABOVE																			
0.86	124	AS ABOVE																			
0.88	130	•	•	•	•	•	•	•	•	•	•	•	•	•	•	•	•	•	•	•	•
0.90		•	•	•	•	•	•	•	•	•	•	•	•	•	•	•	•	•	•	•	•
0.92		•	•	•	•	•	•	•	•	•	•	•	•	•	•	•	•	•	•	•	•
0.92	136	AS ABOVE																			
0.94		AS ABOVE																			
0.96		AS ABOVE																			
0.96	142	AS ABOVE																			
0.98		AS ABOVE																			
1.00		AS ABOVE																			
1.00	148	AS ABOVE																			
1.02		AS ABOVE																			
1.04		AS ABOVE																			
1.04	154	AS ABOVE																			
1.06		AS ABOVE																			
1.08		AS ABOVE																			
1.08	160	AS ABOVE																			
1.10		AS ABOVE																			
1.12		AS ABOVE																			
1.12	166	AS ABOVE																			
1.14		AS ABOVE																			
1.16		AS ABOVE																			

• Indicates computation of real part of signal correlation and clutter intensity for this ( $t, \tau$ ) position.

\* Data samples are taken at time-base delays  $t + \tau$ . Subtract 100  $\mu$ sec from  $t$  for  $\tau \geq 200$   $\mu$ sec (wide-spaced pair).

† See Table III regarding altitude changes.

‡ These altitudes added 30 December 1970, prior to which the computation scheme below 130 km was same as that shown for 130 km (three time-base delays per lag for  $\tau \geq 100$   $\mu$ sec), with 380- $\mu$ sec lag measured also.

(a) Mode F.

Fig. 1(a-c). Diagrams showing time-base delay  $t$  of first sample of each pair for computing correlation for different pulse spacings  $\tau$ .

TIME-BASE DELAY* (msec)	CENTER HEIGHT † (km)	$\tau$ ( $\mu$ sec)																				
		0	20	40	60	80	100	120	140	160	180	200	220	240	260	280	300	320	340	360	380	
1.14	167																					
1.16					o	o	o	o	o	o	o	o	x	x	x	x	x	x	x	x	x	x
1.18		o	o	o	o	o	o	o	o	o	o	o	x	x	x	x	x	x	x	x	x	x
1.20					o	o	o	o	o	o	o	o	x	x	x	x	x	x	x	x	x	x
1.22													o	x	x	x	x	x	x	x	x	x
1.28	182	AS ABOVE																				
1.34	197																					
1.36					o	o	o	o	o	o	o	o	x	x	x	x	x	x	x	x	x	x
1.38		o	o	o	o	o	o	o	o	o	o	o	x	x	x	x	x	x	x	x	x	x
1.40					o	o	o	o	o	o	o	o	x	x	x	x	x	x	x	x	x	x
1.42													o	x	x	x	x	x	x	x	x	x
1.48	212	AS ABOVE																				
1.54	227																					
1.56					o	o	o	o	o	o	o	o	x	x	x	x	x	x	x	x	x	x
1.58		o	o	o	o	o	o	o	o	o	o	o	x	x	x	x	x	x	x	x	x	x
1.60					o	o	o	o	o	o	o	o	x	x	x	x	x	x	x	x	x	x
1.62													o	x	x	x	x	x	x	x	x	x
1.68	242	AS ABOVE																				
1.74	257																					
1.76					o	o	o	o	o	o	o	o	x	x	x	x	x	x	x	x	x	x
1.78		o	o	o	o	o	o	o	o	o	o	o	x	x	x	x	x	x	x	x	x	x
1.80					o	o	o	o	o	o	o	o	x	x	x	x	x	x	x	x	x	x
1.82													o	x	x	x	x	x	x	x	x	x
1.88	272	AS ABOVE																				
1.94	287																					
1.96					o	o	o	o	o	o	o	o	x	x	x	x	x	x	x	x	x	x
1.98		o	o	o	o	o	o	o	o	o	o	o	x	x	x	x	x	x	x	x	x	x
2.00					o	o	o	o	o	o	o	o	x	x	x	x	x	x	x	x	x	x
2.02													o	x	x	x	x	x	x	x	x	x
2.08	302	AS ABOVE																				
2.14	317																					
2.16					o	o	o	o	o	o	o	o	x	x	x	x	x	x	x	x	x	x
2.18		o	o	o	o	o	o	o	o	o	o	o	x	x	x	x	x	x	x	x	x	x
2.20					o	o	o	o	o	o	o	o	x	x	x	x	x	x	x	x	x	x
2.22													o	x	x	x	x	x	x	x	x	x

o Indicates computation of complex correlation at this (t,  $\tau$ ) location.

x Indicates computation of real part of correlation at this (t,  $\tau$ ) location.

\*Data samples are taken at time-base delays  $t + \tau$ . Subtract 100  $\mu$ sec for  $\tau \geq 200$   $\mu$ sec (wide-spaced pair). Full set of time-base delays is not listed where  $\tau$  column is labeled AS ABOVE.

† See Table III regarding altitude changes.

(b) Mode G.

Fig. 1(a-c). Continued.

TIME-BASE DELAY* (msec)	CENTER HEIGHT (km)	$\tau$ ( $\mu$ sec)																				
		0	10	20	30	40	50	60	70	80	90	100	110	120	130	140	150	160	170	180	190	
1.51	215											o	o	o	o	o	o	o	o	o	o	
1.53							o	o	o	o	o	o	o	o	o	o	o	o	o	o	o	
1.55		o	o	o	o	o	o	o	o	o	o	o	o	o	o	o	o	o	o	o	o	
1.57							o	o	o	o	o	o	o	o	o	o	o	o	o	o	o	o
1.59													o	o	o	o	o	o	o	o	o	o
1.75	245	AS ABOVE																				
1.95	275	AS ABOVE																				
2.15	306	AS ABOVE																				
2.31	335											o	o	o	o	o	o	o	o	o	o	
2.33							o	o	o	o	o	o	o	o	o	o	o	o	o	o	o	o
2.35		o	o	o	o	o	o	o	o	o	o	o	o	o	o	o	o	o	o	o	o	o
2.37							o	o	o	o	o	o	o	o	o	o	o	o	o	o	o	o
2.39													o	o	o	o	o	o	o	o	o	o
2.58	365	AS ABOVE																				
2.71	395											o	o	o	o	o	o	o	o	o	o	
2.73							o	o	o	o	o	o	o	o	o	o	o	o	o	o	o	o
2.75		o	o	o	o	o	o	o	o	o	o	o	o	o	o	o	o	o	o	o	o	o
2.77							o	o	o	o	o	o	o	o	o	o	o	o	o	o	o	o
2.79													o	o	o	o	o	o	o	o	o	o
2.95	425	AS ABOVE																				
3.11	455											o	o	o	o	o	o	o	o	o	o	
3.13							o	o	o	o	o	o	o	o	o	o	o	o	o	o	o	o
3.15		o	o	o	o	o	o	o	o	o	o	o	o	o	o	o	o	o	o	o	o	o
3.17							o	o	o	o	o	o	o	o	o	o	o	o	o	o	o	o
3.19													o	o	o	o	o	o	o	o	o	o
3.35	485	AS ABOVE																				
3.51	515											o	o	o	o	o	o	o	o	o	o	
3.53							o	o	o	o	o	o	o	o	o	o	o	o	o	o	o	o
3.55		o	o	o	o	o	o	o	o	o	o	o	o	o	o	o	o	o	o	o	o	o
3.57							o	o	o	o	o	o	o	o	o	o	o	o	o	o	o	o
3.59													o	o	o	o	o	o	o	o	o	o

o Indicates computation of complex correlation at this (t,  $\tau$ ) location.

\*Data samples are taken at time-base delays  $t + \tau$ . Full set of time-base delays is not listed where  $\tau$  column is labeled AS ABOVE.

(c) Mode H.

Fig. 1(a-c). Continued.

plasma-drift information is thus lost. Analysis of these data therefore also neglects the small difference between the magnitude and real part of the acf.

A 40- $\mu$ sec pulse is used, giving  $\Delta h = 6$  km. In the lower altitude portion of Mode F, the sample interval is 3 km, but adjacent 3-km samples are not independent (Table III); in the upper portion, the sample interval is 6 km, but  $\Delta h$  is degraded to 12 km at some correlation lags due to a scheme of averaging neighboring samples along the time base (Fig. 1). Such averaging improves the statistics of the acf's, but results from adjacent 6-km height regions are no longer completely independent.

The acf is measured from 0 to 380  $\mu$ sec, but a shorter maximum lag applies at the higher altitudes (Fig. 1). The spacing between lags is 20  $\mu$ sec.

#### D. MODE G

This mode is designed to yield  $T_i$ ,  $T_e$ , and drift velocity  $V_d$  as a function of height in the region above that covered by Mode F as high as the layer peak. Ground-clutter echoes were not expected to extend to these ranges, and its filtering is not attempted. (The lowest Mode G altitude, however, is often seen to be contaminated with clutter, and in very adverse situations this clutter has been seen out to ranges of 200 km.)

A 100- $\mu$ sec pulse is used, giving  $\Delta h = 15$  km, but averaging of neighboring time-base samples, as in Mode F, degrades this to 27 km at some correlation lags (Fig. 1). Therefore, results from adjacent 15-km intervals are not completely independent.

The correlation function is measured from  $\tau = 0$  to 380  $\mu$ sec, but a shorter maximum lag applies at the higher altitudes (Fig. 1). The spacing between lags is 20  $\mu$ sec.

#### E. MODE H

Mode H is designed to yield  $T_i$ ,  $T_e$ , and  $V_d$  profiles in the topside ionospheric F-region, to as high an altitude as can usefully be studied with this mode. This mode is also specifically designed to include enough of the region below the F2 peak from which useful nighttime returns are obtained so that Modes F and G may be omitted at these times.

A 200- $\mu$ sec pulse is used, giving  $\Delta h = 30$  km, but averaging of neighboring time-base samples, as in Modes F and G, degrades this to 42 km at some correlation lags (Fig. 1). Accordingly, results from adjacent 30-km intervals are not completely independent.

Over the altitude region examined by Mode H, the echo power spectrum widens owing to the increase in ionospheric temperature and decrease in ion mass;<sup>9</sup> this causes the interesting range of correlation to be reduced in comparison with the Mode F and G values. Accordingly, the acf is measured only from  $\tau = 0$  to 190  $\mu$ sec, but a shorter maximum lag applies at the higher altitudes (Fig. 1). The spacing is then reduced to 10  $\mu$ sec.

#### F. MODE I

Mode I is designed to yield an electron density profile in the ionospheric D-region. The region covered extends upward into the lower E-region to allow normalization of the density values using ionosonde determinations of  $f_oE$ .

A 20- $\mu$ sec pulse is used, giving  $\Delta h = 3$  km. The sample interval is 1.5 km; adjacent samples, however, are not independent.

Mode I signals are very weak, and below the D-region "ledge" weak clutter returns are observed which are thought to be caused by aircraft. These essentially set a lower limit to the height region that can be studied.

The D-region Mode I observations have been the subject of a separate paper,<sup>14</sup> but are included here for completeness.

#### G. OBSERVING PROGRAM

The observing program that can be established using Modes E, F, G, H, and I is flexible in that any sequence of modes and choice of integration times may be used. A typical operation might use a repeated EFGH sequence with integration times of 4, 10, 8, and 4 min., respectively, during the day and a repeated EH sequence with integration times of 8 and 20 min., respectively, at night. Such a scheme has the merit of maintaining a complete observing sequence of 30-min. duration. The integration times are made unequal to offset the S/N differences achieved in these modes. Operations such as this have been run about once a month since November 1969.

Besides these routine observations, more specialized programs have been run from time-to-time. For observations of E-region atmospheric tides, the typical sequence has been modified to concentrate on Mode F (e.g., EFFFFGH), completing a sequence every hour. Occasional observations have been made during an overhead pass of a scientific satellite. One eclipse has been observed. A few operations consisting of E Modes run in rapid succession (e.g., 2-min. runs), have been conducted to observe traveling ionospheric disturbances with fine time resolution. These were termed Rapid Sequence E Mode (RASEM).

Mode I has been run only a few times, usually in coordination with Wallops Island rocket launches. The Mode I signals are very weak and require long integration times (typically 15 min. by day and 30 min. by night).

Tables IV, V, and VI provide lists of regular 2-pulse, RASEM, and Mode I operations obtained from November 1969 through December 1975. Some RASEM results have been presented in Ref. 15.

#### H. MODE MODIFICATIONS

The evolution of the 2-pulse program at Millstone Hill has seen three major modifications to existing modes that affect collection, analysis, and quality of the data. These modifications, their dates of implementation, and the locations in the text dealing with them are given below:

- (1) 6 November 1970 - the manner of noise measurement was modified (Sec. IV-B and Table XI).
- (2) 20 December 1970 - three additional lower E-region altitudes were added to Mode F (Sec. V-A, Fig. 1(a), and Table III).
- (3) 16 December 1971 - timing changes modified the altitudes of measurement (Table III).

This report is written to apply specifically to data collected commencing 16 December 1971, but many comments have been included to cover the operations prior to that date.

TABLE IV  
TWO-PULSE UHF OBSERVATIONS PRIOR TO 1976

Date	Start (GMT)	End (GMT)	Comments
<u>1969</u>			
28-29 November	1440	1410	Modes F, G only
19-20 December	0200	0200	Modes F, G, H only
30 December	1445	2050	Modes F, G, H only
<u>1970</u>			
13-14 January	1350	1450	Modes F, G, H only
30 January	1420	2040	
5-6 February	1420	1440	
5 March	1500	2250	Pre-eclipse run
6 March	1500	2215	Pre-eclipse run
7 March	1350	2400	Eclipse observations
9 March	1415	1940	
9 April	1415	1940	
1 May	1330	2050	
2 July	1215	1900	
25-26 July	1305	0225	Low transmitter power
9-10 August	1255	0140	
25 August	2105	2240	Modes E, G, H only
26 August	0345	0510	Modes E, G, H only
19 September	1130	2320	
6 November	1400	2100	
30-31 December	2010	0400	First Mode F with correlation functions every 3 km ( $h \leq 127$ km)



TABLE IV (Continued)			
Date	Start (GMT)	End (GMT)	Comments
<u>1971</u>			
6 January	1430	2100	Mode F with 20- $\mu$ sec pulse
29-30 January	0105	0200	
8-9 February	2240	0400	Modes E, G, H only
23-24 February	1625	1650	
25-26 March	1525	1540	
13-14 April	2135	2050	
10-11 May	2015	2015	Only Mode E good
3-4 June	2100	2100	
26-27 July	2005	0900	
27 July	1410	2010	
28 July	0045	1415	
30-31 August	2045	2000	
21-22 September	1610	1625	Adalart sudden commencement Adalart magstorm
23-24 October	1135	1120	
16-17 November	1600	1640	
21-22 December	1535	1755	
27 December	1415	2135	Modes E, F only (tidal studies)
28 December	1310	2115	Modes E, F only (tidal studies)
29 December	1330	1900	Modes E, F only (tidal studies)
30 December	1330	2045	Modes E, F only (tidal studies)

TABLE IV (Continued)

Date	Start (GMT)	End (GMT)	Comments
<u>1972</u>			
11-12 January	1710	1820	
7-8 February	2200	0500	
1-2 March	1600	1700	
28-29 March	1600	1640	
3 April	1300	2100	EFFFFGH (tidal studies)
4 April	1300	2330	EFFFFGH (tidal studies)
5 April	1505	2330	EFFFFGH (tidal studies)
6 April	1250	2100	EFFFFGH (tidal studies)
7 April	1500	2320	EFFFFGH (tidal studies)
16 May	1025	2400	EFFFFGH (magstorm alert)
17 May	1020	2345	EFFFFGH (magstorm alert)
18 May	1010	2350	EFFFFGH (magstorm alert)
20-21 June	1515	1600	
24-25 July	1810	2205	
17-18 August	1135	1615	
20-21 September	1000	1340	
21-22 September	1430	2330	EFFFFGH (tidal studies)
23 September	0955	2400	EFFFFGH (tidal studies)
24 September	1000	2300	EFFFFGH (tidal studies)
24-25 October	1340	1550	
21-22 November	1415	2205	
12-13 December	1155	1200	
13 December	1215	2345	EFFFFGH (tidal studies)
14 December	1200	2305	EFFFFGH (tidal studies)

TABLE IV (Continued)

Date	Start (GMT)	End (GMT)	Comments
<u>1973</u>			
24-25 January	1720	2145	
6-7 March	2225	2235	
13-14 April	1640	1940	Magstorm alert and AEROS transit
8-9 May	1730	2320	
10 May	1715	1955	AEROS transit
5-6 June	1835	2100	ISIS II transit
18-19 June	1450	2200	Magstorm alert
20 June	1145	2020	
21 June	1150	2230	EFFFFGH (tidal studies)
22 June	1125	2230	EFFFFGH (tidal studies)
23 June	1210	1910	EFFFFGH (tidal studies)
10 July	1805	1925	AEROS transit
30-31 July	2005	2155	AEROS transit
28-29 August	1530	2210	
24-25 September	1835	2315	
26 September	1200	2230	EFFFFGH (tidal studies)
27 September	1150	2200	EFFFFGH (tidal studies)
28 September	1150	2210	EFFFFGH (tidal studies)
25 October	1200	2040	
6 November	1915	2145	
8 November	1955	2200	
10 November	1915	2145	
23 November	1225	2135	
6 December	1135	1300	
17-18 December	2030	2150	
19 December	1235	2145	
20 December	1235	2130	EFFFFGH (tidal studies)
21 December	1540	2120	

TABLE IV (Continued)

Date	Start (GMT)	End (GMT)	Comments
<u>1974</u>			
3 January	1215	2235	
4 January	1225	2248	
5 January	1205	2230	
16 January	1115	2115	EEEEFGH (tidal studies)
14 February	1545	1745	
15 February	1540	1755	
22 February	1135	2144	EEEEFGH (tidal studies) (unable to read data tape)
4 March	1225	1350	
18 March	1110	2205	EEEEFGH (tidal studies)
19 March	1115	2240	EEEEFGH (tidal studies)
20 March	1105	2300	EEEEFGH (tidal studies)
19 April	0220	0450	
30 April	1055	1915	EEEEFGH (tidal studies)
17 May	1450	1750	
28 May	1015	2340	EEEEFGH (tidal studies)
2 June	1045	2355	EEEEFGH (tidal studies)
18 June	0940	2240	EEEEFGH (tidal studies)
19 June	1005	0015	EEEEFGH (tidal studies)
29-30 June	1545	1715	
2 July	0315	0920	Modes E, H only
1 August	1025	2350	EEEEFGH (tidal studies)
10 August	1130	2325	EEEEFGH (tidal studies)
11 August	1050	2245	EEEEFGH (tidal studies)
12 August	1040	0005	EEEEFGH (tidal studies)
13 August	1050	0015	EEEEFGH (tidal studies)
14 August	1105	0005	EEEEFGH (tidal studies)
15 August	1110	2330	EEEEFGH (tidal studies)
17-18 September	1040	2105	EEEEFGH (tidal studies)
30-31 October	1455	1535	
12-13 November	1210	2215	EEEEFGH (tidal studies)
10-11 December	1250	2150	EEEEFGH (tidal studies)
13-14 December	1205	2125	EEEEFGH (tidal studies)

TABLE IV (Continued)

Date	Start (GMT)	End (GMT)	Comments
<u>1975</u>			
15-16 January	1330	1400	
12-13 February	1150	2305	EEEEFGH (tidal studies)
21-22 March	1725	2040	
15-16 April	1440	2150	
2-4 May	2145	0230	
7 May	2155	2400	
23-24 May	2320	2345	
10 June	1055	2240	EEEEFGH (tidal studies)
11 June	1035	2305	EEEEFGH (tidal studies)
12 June	1030	2245	EEEEFGH (tidal studies)
16-18 July	2130	2000	
11 August	1125	2250	EEEEFGH (tidal studies)
12 August	1100	1605	EEEEFGH (tidal studies)
13 August	1945	2250	EEEEFGH (tidal studies)
24-25 September	1215	1355	
13 October	1110	2205	EEEEFGH (tidal studies)
14 October	1535	2130	EEEEFGH (tidal studies)
15 October	1040	2140	EEEEFGH (tidal studies)
16 October	1210	1910	EEEEFGH (tidal studies)
17 October	1040	2210	EEEEFGH (tidal studies)
21-22 November	2200	2400	
13 December	1210	2310	EEEEFGH (tidal studies)
16 December	1210	2120	EEEEFGH (tidal studies)

TABLE V  
 RASEM OPERATIONS PRIOR TO 1976

Date	Start (GMT)	End (GMT)	Comments
<u>1970</u>			
13 March	1400	2000	Interrupted 1448-1520; 1700-1820
10 April	1420	2200	Interrupted 1430-1442
8-9 May	1545	0405	Interrupted 0000-0002
15-16 May	1555	0330	Interrupted 1758-1808; 2052-2110; and 0000-0014
22-23 May	1700	0400	Interrupted 0000-0241
28-29 May	1540	0320	Interrupted 0000-0002
8-9 August	1345	2400	
26 September	1110	2330	
<u>1971</u>			
20-21 May	1730	0340	Interrupted 0000-0008
10-11 June	2010	2020	Interrupted 0000-0003; 0041-0044
30 November - 1 December	2300	0400	

TABLE VI  
MODE I OPERATIONS PRIOR TO 1976

Date	Start (GMT)	End (GMT)	Comment
<u>1970</u>			
27-28 November	2110	2130	Operated with separate recovery channel
31 December	1600	2100	
<u>1971</u>			
23-24 April	1545	0040	
<u>1972</u>			
20 January	1730	1800	Coordinated with Wallops Island rocket launches
31 January	1715	1900	Coordinated with Wallops Island rocket launches
<u>1973</u>			
15 January	1605	1810	Coordinated with Wallops Island rocket launches
16 January	1645	2000	Coordinated with Wallops Island rocket launches
<u>1974</u>			
15 January	1355	1850	

### III. EQUIPMENT

#### A. GENERAL

The system parameters of the 68-cm radar system have been presented in Ref. 1 together with a brief description of the apparatus; this is not repeated here. The antenna, shown in Fig. 2, directs a pencil beam  $2^\circ$  south of the zenith; this slight offset allows the radio star Cygnus to pass through the radar beam for calibration purposes. Since the antenna is on a hill, there is a virtual absence of natural screening that would prevent reflections from distant hills. In normal operations, strong ground returns are observed in the antenna sidelobes out to ranges of the order of 100 km, and again near 150 km. During very adverse conditions, clutter echoes can be detected out to 200 km range. By transmitting short pulses and searching with the steerable radar antenna, we have been able to locate the ranges and directions of the offending regions. Figure 3 shows a PPI display of returns obtained in this manner, with the main beam of the steerable antenna at an elevation of  $0.2^\circ$ . The range markers on this display denote intervals of 8 nmi (14.8 km). The most distant returns appear to be extended in range and come from the north. Nearly all can be identified with mountains in New Hampshire, those at 150 km being the White Mountains. Smaller returns to the south are not permanent and are probably caused by aircraft.

One scheme that has been considered for combatting the clutter returns is the construction of an anti-clutter fence over a  $60^\circ$  sector of the northern side of the antenna. Unfortunately, such a fence would need to be over 100 ft high and several hundred feet long and thus far has been ruled out on the basis of cost. A number of less-expensive solutions have been attempted, however. These include the addition of a large conical skirt to the antenna feed horn to reduce the intensity of echoes observed directly from the horizon. Additional returns are believed to come via reflections off the tripod feed support legs (Fig. 2). In an effort to reduce these, absorbing netting has been placed along each of the three legs a distance of approximately  $\lambda/4$  from the inside face. In addition, the size of the feed horn has been increased so that more energy is directed toward the center of the reflector, i.e., the taper of the illumination over the aperture has been increased from 10 to 20 dB. This last change was accomplished by adding to the feed horn an extension that incorporated a quarter-wave choke round its edge. The choke appears to have improved the efficiency of the feed horn, with the result that the effective collecting area of the antenna does not appear to have decreased despite the increase in beamwidth.<sup>1</sup>

One final step that may have contributed to improving the radiation pattern of the antenna has been a reworking and strengthening of the surface that has reduced the rms surface tolerance to about an inch ( $\lambda/24$ ).

#### B. FREQUENCY CONTROL

The modifications described above have reduced the intensity of the ground returns to the point where, as a rule, they no longer saturate the receiver at its normal gain setting. This makes it possible to consider removing the echoes from the data by filtering in frequency, as the ground returns are expected to be coherent. Accordingly, modifications have been made to the radar equipment so that phase coherence of the ground returns will be preserved. This has required that all the receiver local oscillator frequencies, as well as those generated in the exciter, be obtained from a single coherent oscillator as shown in Fig. 4. Also, the received signals must be applied to phase-sensitive rectifiers in place of a simple linear rectifier employed



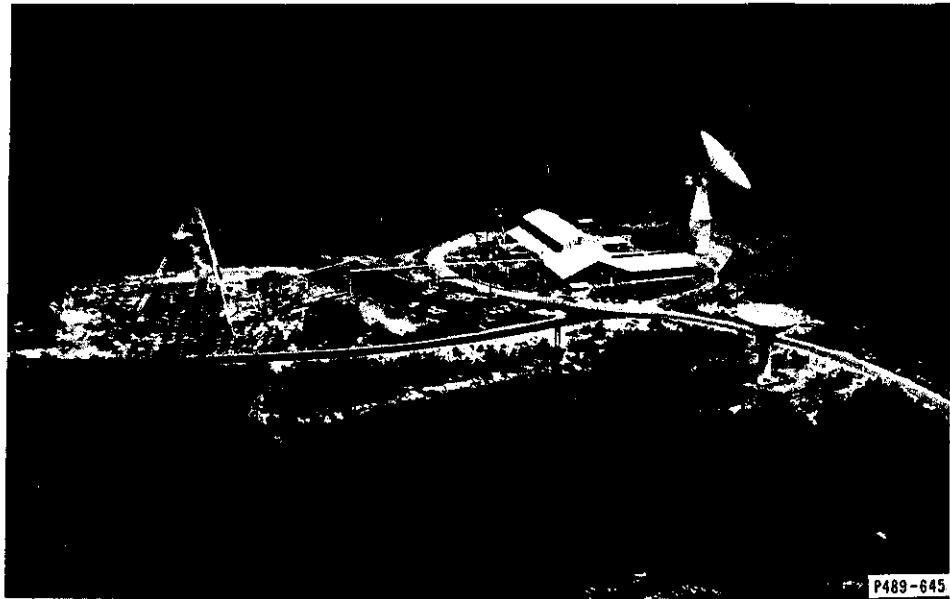


Fig. 2. Millstone Hill Field Station. To left is 220-ft vertically pointing UHF antenna. Tripod supports horn feed at focus. Building to right contains transmitting and receiving equipment. Larger, fully steerable antenna operates at L-band and has been employed for ionosphere studies at oblique incidence.

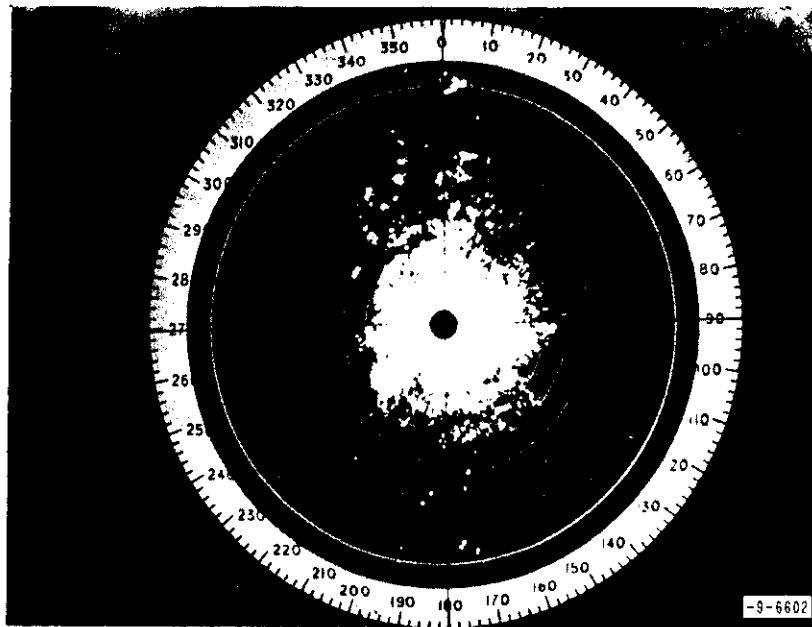


Fig. 3. PPI display of ground-clutter returns observable from Millstone. Range marks are 14.8 km apart.

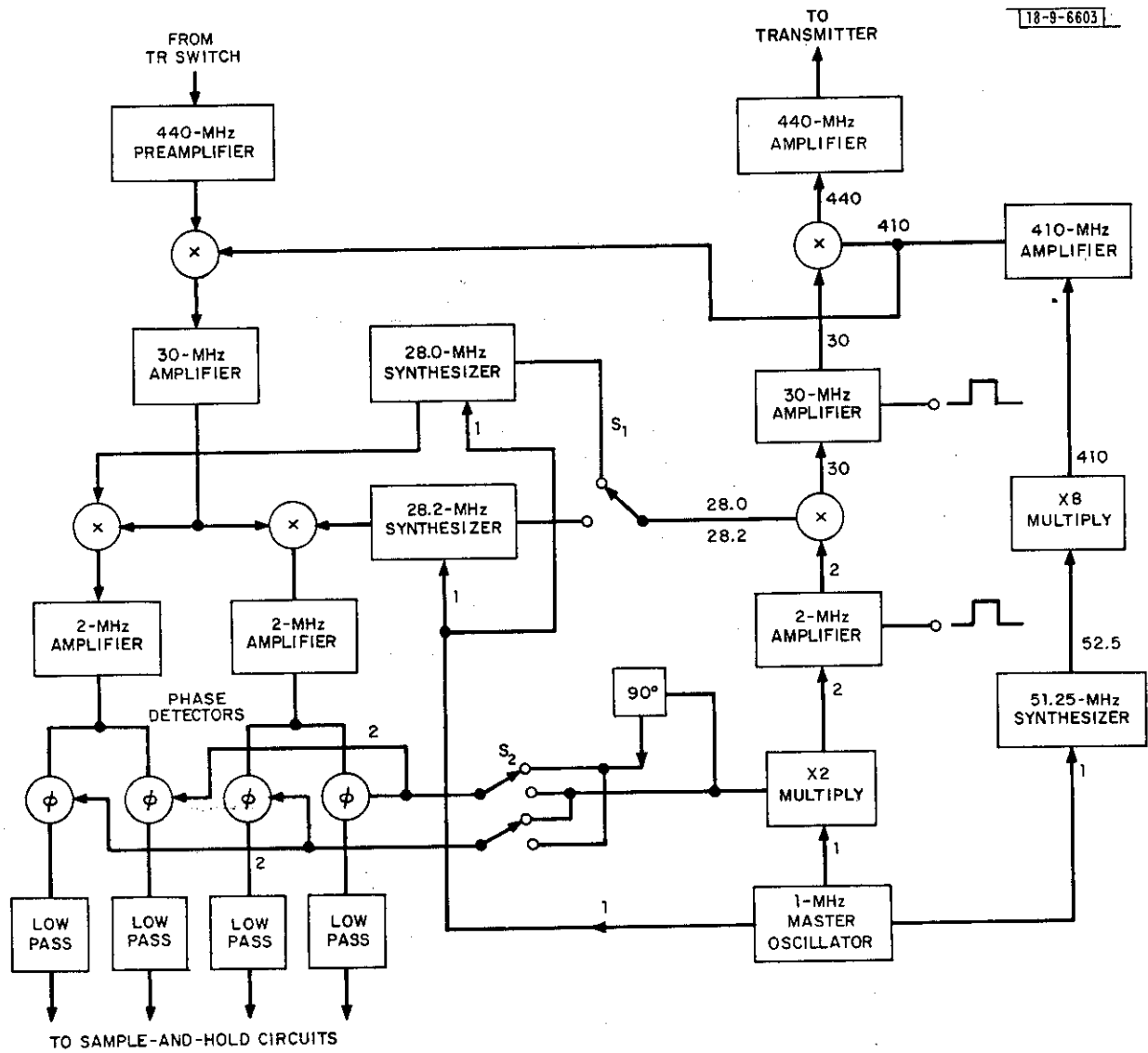


Fig. 4. Block diagram showing frequency control system for radar employed for measurements described in this report.

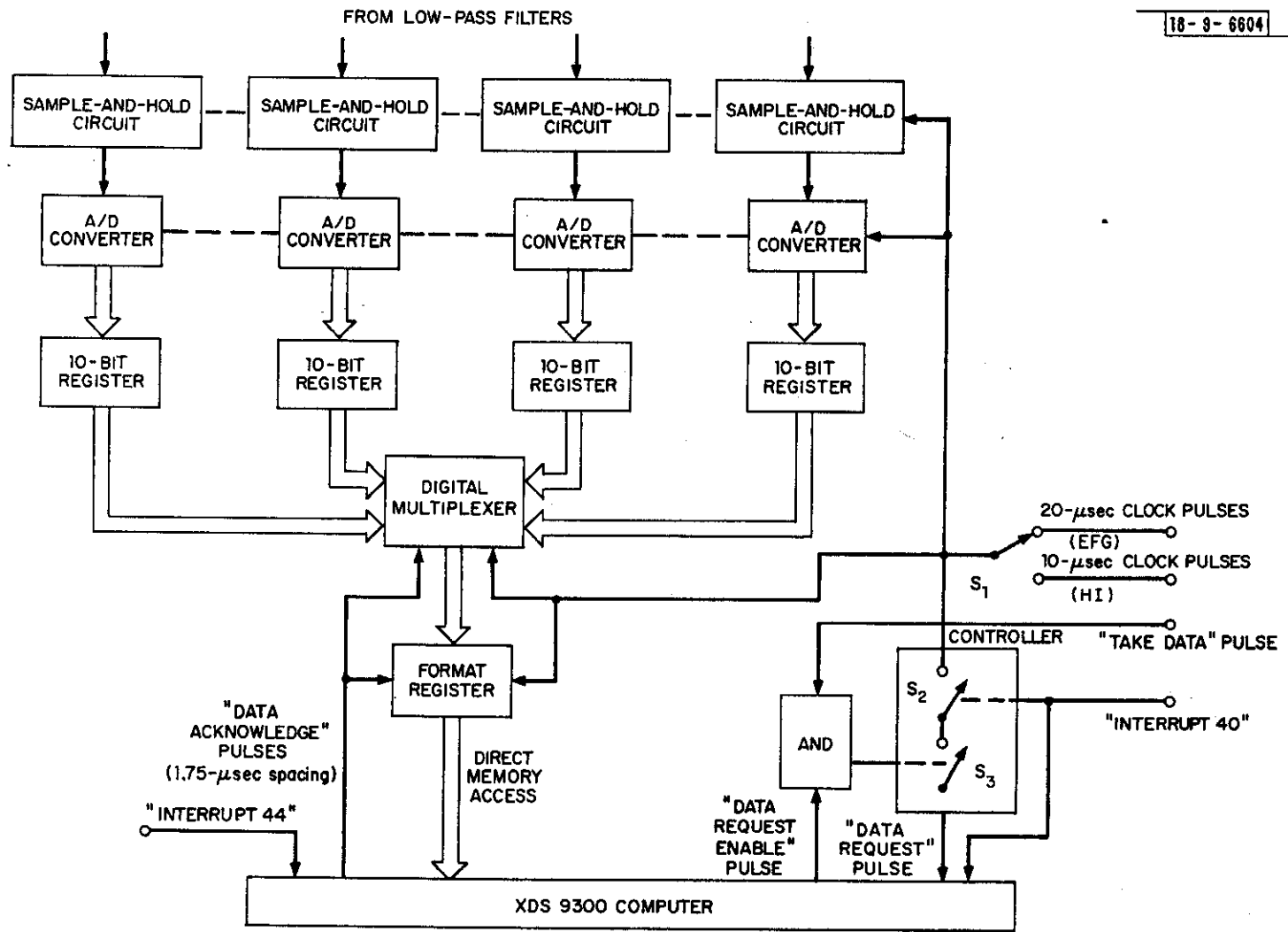


Fig. 5. Block diagram showing data-sampling and data-transfer equipment employed to measure signal voltages (Fig. 4) and communicate these to computer.

hitherto. With these changes it is possible to monitor the phase of the more distant clutter returns and see that this does indeed vary only slowly with time.

The new frequency control system (Fig. 4) provides the capability of switching the transmitter frequency rapidly via the solid-state switch  $S_1$ . This provision permits the radar frequency to be changed between adjacent pulses and, in effect, permits two experiments to be performed during the course of a single sweep of the radar.

### C. RECEIVER

In order to receive separately pulses transmitted on adjacent frequencies, the receiver has been modified to provide two IF channels tuned to the correct frequencies as shown in Fig. 4. The spacing between the frequencies may be varied by altering the setting of the 28.2-MHz frequency synthesizer, but the separation must be kept to a value that can be accepted by the common 30-MHz IF amplifier. Each receiver channel drives a pair of phase-sensitive rectifiers operated in quadrature. These rectifiers, in turn, drive low-pass filters having a time constant of 10  $\mu$ sec. The sine and cosine channels of the phase-sensitive rectifiers can be reversed by throwing switch  $S_2$ . By commutating the role played by the two phase detectors in each channel, any systematic effects due to differences in their gain or incomplete phase separation can be removed. This is of particular importance in attempting to determine the ionospheric drift velocity accurately.

In order to minimize the time over which the noise in the receiver is correlated, it is necessary to employ a wide receiver bandwidth. Thus, the overall pre-detector bandwidth has been set at 50 kHz and the post-detector bandwidth at 100 kHz, yielding an effective overall bandwidth of the order of 45 kHz. This value represents a compromise between the desire to keep the bandwidth as narrow as possible (and thus minimize the unwanted noise power in the receiver) and the need to limit the distortion of the spectral data produced by a receiver of finite bandwidth (see Appendix A).

In order to make measurements at altitudes below 100 km, additional modifications have been necessary to improve the receiver recovery time, i.e., the time interval between the transmitter pulse and the restoration of the receiver to its normal operating condition. As originally designed, the UHF transmitter modulator required about 200  $\mu$ sec to turn off the transmitter. The modulator has since been rebuilt to reduce the turn-off time to approximately 2  $\mu$ sec. A second change has been to replace the original gas-discharge tube TR switch by one employing solid-state diodes. The gas-discharge tube in the older switch had a cleanup time of 200 to 300  $\mu$ sec, but the new switch is restored to normal in a few microseconds. Finally, the gating of the receiver has been changed. The original receiver employed vacuum tubes, and suppression was accomplished by applying pulses to short-suppressor-base pentodes in various IF stages. The time constant for recovery was about 100  $\mu$ sec. A solid-state receiver is now employed, and suppression is achieved by inserting diode gates between various amplifier stages. In this way, the recovery time is reduced to  $\sim 10$   $\mu$ sec.

### D. DATA SAMPLING

Data sampling is carried out in the manner indicated in Fig. 5. The video signal voltages appearing at the outputs of the low-pass filters (Fig. 4) are applied to four "sample-and-hold" circuits. On command from a clock pulse (normally every 20  $\mu$ sec), the applied voltages are sampled for an interval of 100 nsec, and this voltage is then stored. A digital voltmeter operating over a range of  $\pm 5$  V assigns any applied voltage a sign and one of 512 levels. The digital

words representing the sampled voltages are stored in registers and transferred one at a time to the computer via a digital multiplexer (switch) and a format register. The function of the format register is to move the sign bit from first position in a 10-bit word to first position in a 24-bit word, i.e., place it in the location required by the computer for immediate multiplication. Transfer of the samples into the memory is carried out at the computer clock rate, namely, one word per 1.75  $\mu$ sec. In order to alert the computer to the presence of the data, two cycles are required (3.5  $\mu$ sec) so that the total transfer time is 10.5  $\mu$ sec.

In two of the operating modes (H, I), only a single receiver channel is employed at a time (see Secs. IV-A-4 and -5). In this case, only one pair of the available digital samples is transferred into the computer. The data transfer time is now 7  $\mu$ sec and is carried out every 10  $\mu$ sec instead of every 20  $\mu$ sec.

#### E. TIMING EQUIPMENT

New timing-generator equipment was constructed to control the transmitter pulse length and spacing and to synchronize the computer to the radar system. This timing generator was known as the B timer to distinguish it from that described in Ref. 1 (A timer), which provided for single-pulse operations. The B timer provided for the four preset operating Modes E, F, G, and H. A second, experimental version of the B timer allowed a variety of pulse lengths, spacings, etc., and was initially employed for measurements made in Mode I. Subsequently, all these units were combined into a single unit.

The new timing equipment was constructed from commercially available logic cards. Selection between modes is provided by push buttons, but can be transferred to the computer. In this case, the computer selects the desired operating mode by loading an output register with an appropriate word.

In order to synchronize the data-acceptance operations at the computer with the radar operations, a synchronizing pulse ("Interrupt 40") is transmitted to the digital interface equipment on each sweep of the radar time base. In Modes H and I, a second synchronizing pulse ("take-data pulse") is required to alert the computer to accept samples from the alternate channel for the remainder of the sweep (see Secs. IV-A-4 and -5). A third synchronizing pulse ("Interrupt 44") alerts the computer to the end of a cycle of pulse spacings. This pulse is transmitted to the data interface 200  $\mu$ sec in advance of the next "Interrupt 40" synchronization pulse.

Modes E and I include a noise-calibration pulse inserted at the receiver terminals via a coaxial coupler at the end of each sweep. This pulse raises the noise level in the receiver by 100 K, allowing signal intensity conversion to absolute (temperature) units.

In some of the modes provided by the new timing equipment, as many as four separate RF pulses are required (2-pulse measurement on each of two frequencies). As shown in Fig. 4, the transmitter RF pulses are generated by an exciter which is an inverse superheterodyne system. Gating is applied to amplifiers at the 2- and 30-MHz levels (Fig. 4) and to the 51.25-MHz signal as well (not shown in Fig. 4). The gating is carried out using solid-state (diode) switches manufactured by Sanders Associates. These gates require separate ON and OFF triggers. For some modes and spacings, the timing generator yields coincident ON and OFF pulses leading to improper operation of the gates. Accordingly, it is necessary to employ the trigger pulses to generate the required modulator pulses and connect these through "OR" gates in such a manner that any one modulator pulse can hold the exciter ON. This arrangement is indicated schematically in Fig. 6.

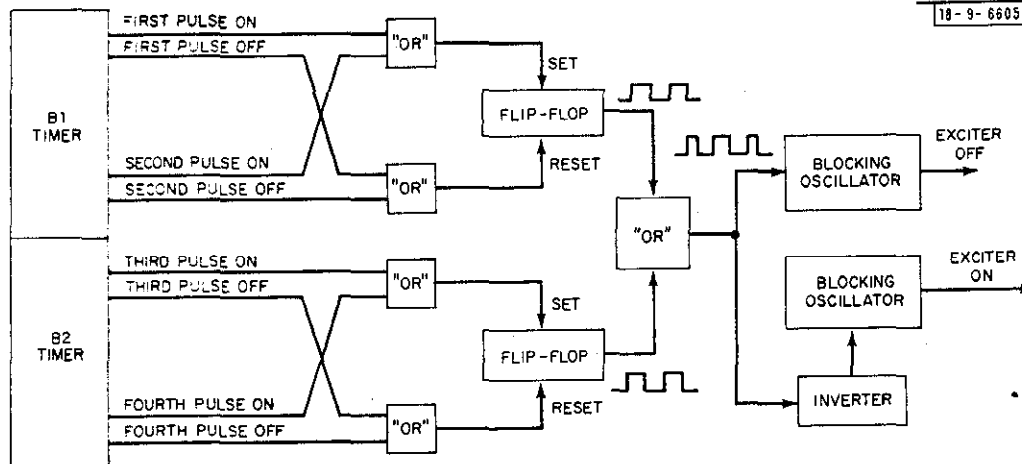


Fig. 6. Block diagram showing manner in which separate transmitter exciter ON and OFF triggers are mixed to control RF pulses generated.

Changes of the exciter frequency are made during the train of pulses under control of the timing equipment via switch  $S_1$  in Fig. 4. Not shown in Fig. 4 is a "commutate" switch which reverses the frequencies arriving at  $S_1$ ; it is under the control of the computer and is used to reverse the order in which the frequencies appear in the pulse train. This effectively commutates the role played by the receiver channels and thereby allows any gain difference between the two channels to be averaged out in the sweep integration performed by the computer. All Modes E, F, G, H, and I use this capability (E-Mode frequency commutation accomplishes no useful purpose, but is retained for simplicity of timer operation).

## A. EQUIPMENT TIMING CONTROL

## 1. Transmitter Control - Mode E

Mode E transmitter timing characteristics are shown in Table VII and Fig. 7(a). Two adjacent 100- $\mu$ sec pulses are transmitted on each sweep of the time base, one on each radar frequency. These pulses separately yield estimates of the echo power vs altitude. The roles of the receiver channels are reversed every 20 sweeps by changing the order in which the pulses are transmitted at the two frequencies. This is under control of the computer, and causes a given receiver channel to handle the returns from the first pulse for 20 sweeps and then returns from the second for 20 sweeps. Returns from the first pulse are summed together irrespective of frequency, so that any differences in the gains of the two channels and/or differences in the powers transmitted at the two frequencies will be averaged out. This commutation performs no useful function in the E Mode (it is essential for all other modes) but is retained for simplicity of timer operation. Figure 7(a) shows the relationship between the transmitter and sync pulses in Mode E. Frequency commutation is performed by the computer on receipt of the "Interrupt 44" pulse (Fig. 5).

## 2. Transmitter Control - Mode F

Mode F transmitter timing characteristics are shown in Table VII and Fig. 7(b). A pair of pulses is transmitted on each of two frequencies each sweep of the time base - one pair for delays  $0 \leq \tau \leq 180 \mu\text{sec}$  (close-spaced pair), the other for delays  $200 \leq \tau \leq 380 \mu\text{sec}$  (wide-spaced pair). The wide-spaced pair is made to surround the close-spaced pair as shown in Fig. 7(b). The first two pulses that are transmitted are controlled by a time-base generator (B1 timer) operating at a fixed interpulse period of 8.00 msec. A second time-base generator (B2 timer), operating at an interpulse period of 8.02 msec, generates the last two pulses of the series as shown in Fig. 8(a). These four pulses are passed through the logic summing network shown in Fig. 8(a) to control the transmitter exciter. Owing to the difference in time-base length, the second two pulses appear 20  $\mu$ sec further displaced from the first two each successive sweep. In this way, the spacing for each pair is made to increase by 20  $\mu$ sec per sweep. A pulse counter operating on the output of the B1 timer counts the number of sweeps and resets the B2 counter into coincidence with the B1 [Fig. 8(a)] every 10 sweeps. Thus, the maximum spacing between pulses is set by counting the number of sweeps, since the two timers were forced into coincidence.

At the instant the B1 and B2 timers are forced into coincidence, the second of the B1 and first of the B2 pulses coincide ( $\tau = 0$ ). The wide-spaced pair of pulses is then separated by 200  $\mu$ sec. Thus, on the first sweep the correlation is measured at  $\tau = 0$  and  $\tau = 200 \mu\text{sec}$ . On the second sweep one obtains the correlation at 20 and 220  $\mu$ sec, and this continues until  $\tau = 180$  and 380  $\mu$ sec. The B2 timer is then resynchronized to the B1 timer. In this way, all possible values of  $\tau$  are obtained in 10 sweeps.

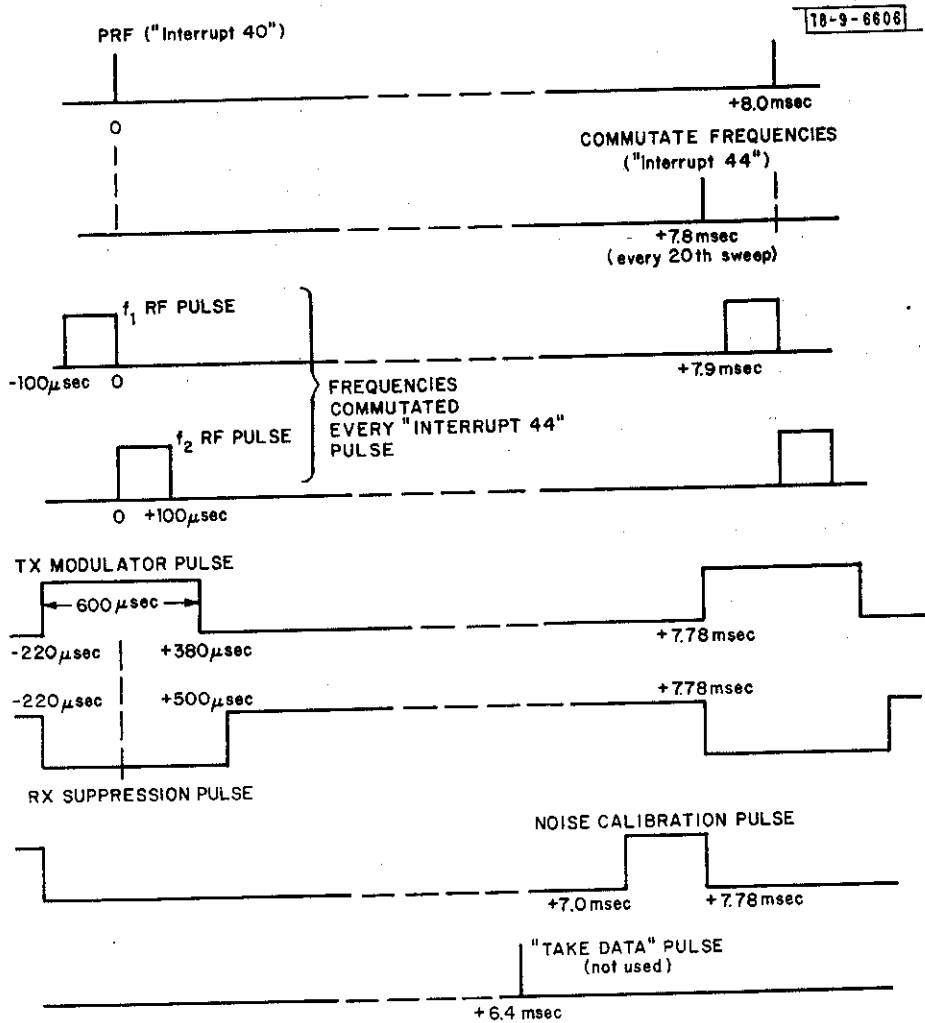
A complication is introduced by the need to remove clutter echoes (Sec. III-A). The clutter subtraction procedure is basically a simple digital filter that removes echoes that appear to be coherent from sweep-to-sweep. For this reason, it is necessary to repeat each sweep at least

TABLE VII  
TRANSMITTER TIMING CHARACTERISTICS

Parameter	Mode				
	E	F	G	H	I
Pulse Length (nominal) ( $\mu\text{sec}$ )	100	40	100	200	20
Interpulse Period (nominal) (msec)	8	8	8	8	5
Transmitted Pulse Mode*	Two pulses per sweep, one on each frequency	Two pairs of pulses per sweep, one on each frequency	Two pairs of pulses per sweep, one on each frequency	One pair of pulses per sweep	One pulse per sweep
Spacing Between Pulses† ( $\mu\text{sec}$ )	100	0 to 180 inner pair, 200 to 380 outer pair	0 to 180 inner pair, 200 to 380 outer pair	0 to 190	NA
Number of Pulse Spacings	1	20	20	20	NA
Step Size ( $\mu\text{sec}$ )	NA	20	20	10	NA
Order of pulses ( $\mu\text{sec}$ ) $f_1$		0, 0, 20, 20, 40, ...	0, 0, 20, 20, 40, ...	0, 10, 20, 30, ...	
$f_2$	NA	200, 200, 220, ...	200, 200, 220, ...	0, 10, 20, 30, ...	NA
Separation Between Close- and Wide-Spaced Pairs ( $\mu\text{sec}$ )	NA	100	100	NA	NA
Number of Sweeps Between Frequency Commutation	20	20	20	1	1
Location of Sync Pulse ("Interrupt 40")	Coincident with start of second pulse	Coincident with start of second pulse	Coincident with start of second pulse	Coincident with start of first pulse	Coincident with start of pulse
Modulator Pulse Length (nominal) ( $\mu\text{sec}$ )	600‡	600	600	600	220
Modulator Pulse Location	Starts 220 $\mu\text{sec}$ before sync	Starts 220 $\mu\text{sec}$ before sync	Starts 220 $\mu\text{sec}$ before sync	Starts 220 $\mu\text{sec}$ before sync	Starts 200 $\mu\text{sec}$ before sync

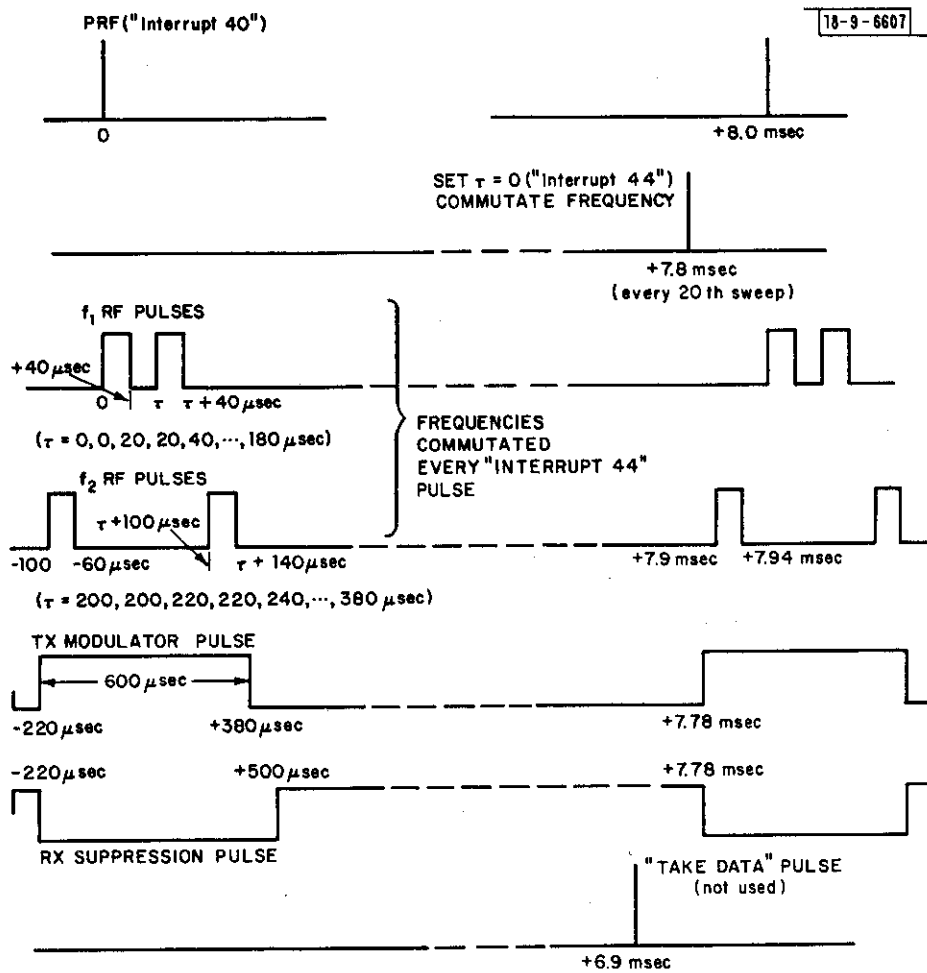
\* Some of these pulse pairs overlap.  
† Maximum spacing is a function of altitude — see Fig. 1.  
‡ 320  $\mu\text{sec}$  in RASEM.





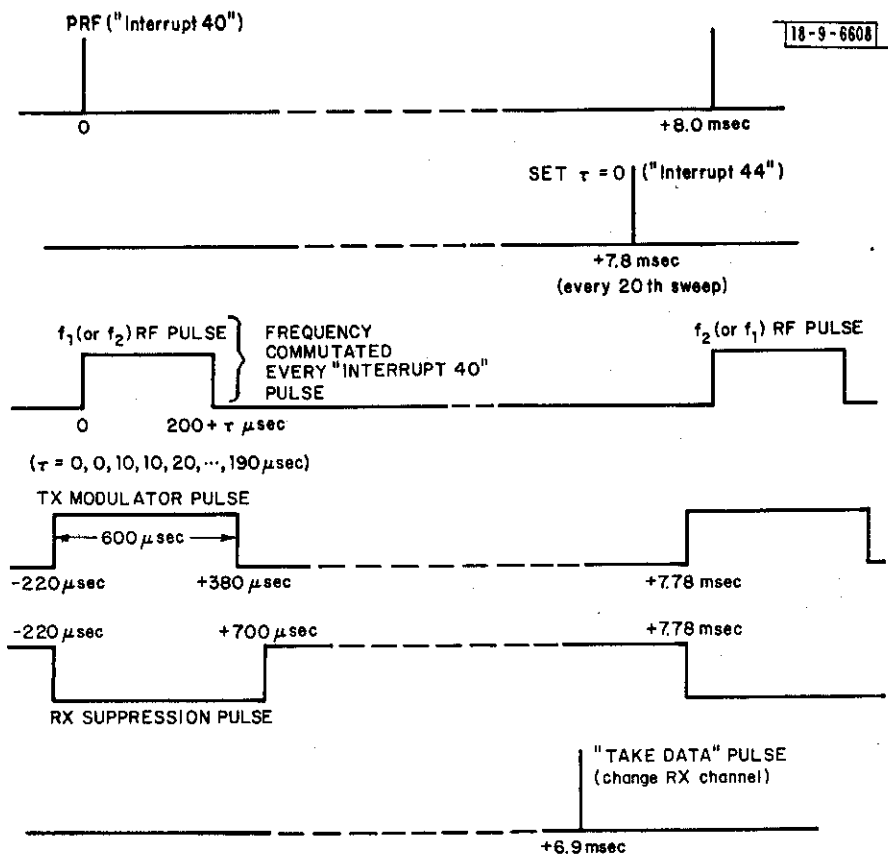
(a) Mode E.

Fig. 7(a-d). Timing diagrams (not to scale) for Modes E, F, H, and I. Mode G differs from Mode F only in that all four RF pulses are 100 μsec in length.

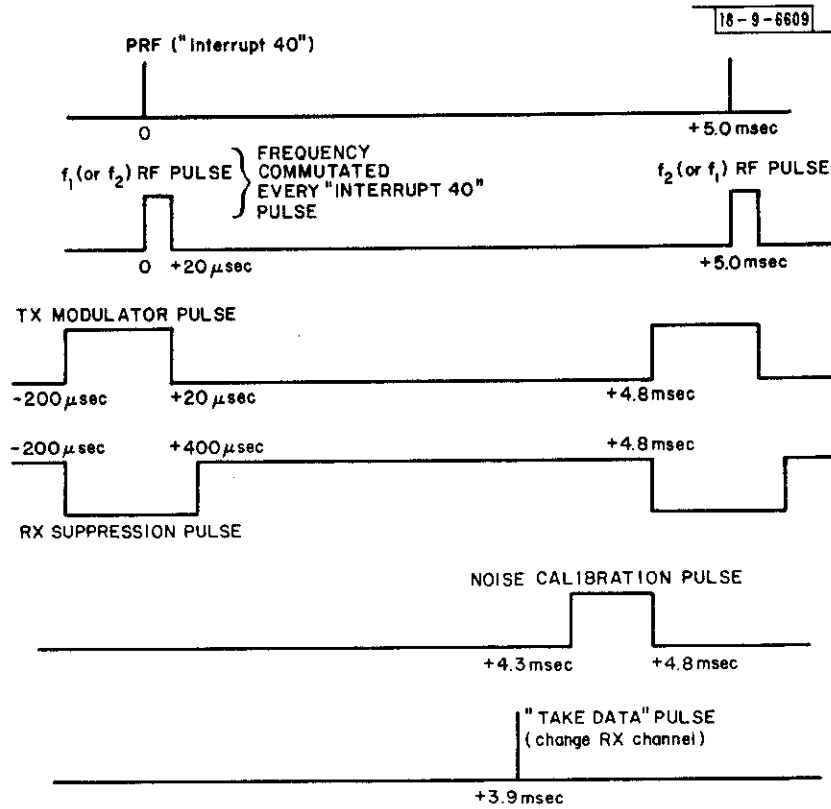


(b) Mode F.

Fig. 7(a-d). Continued.

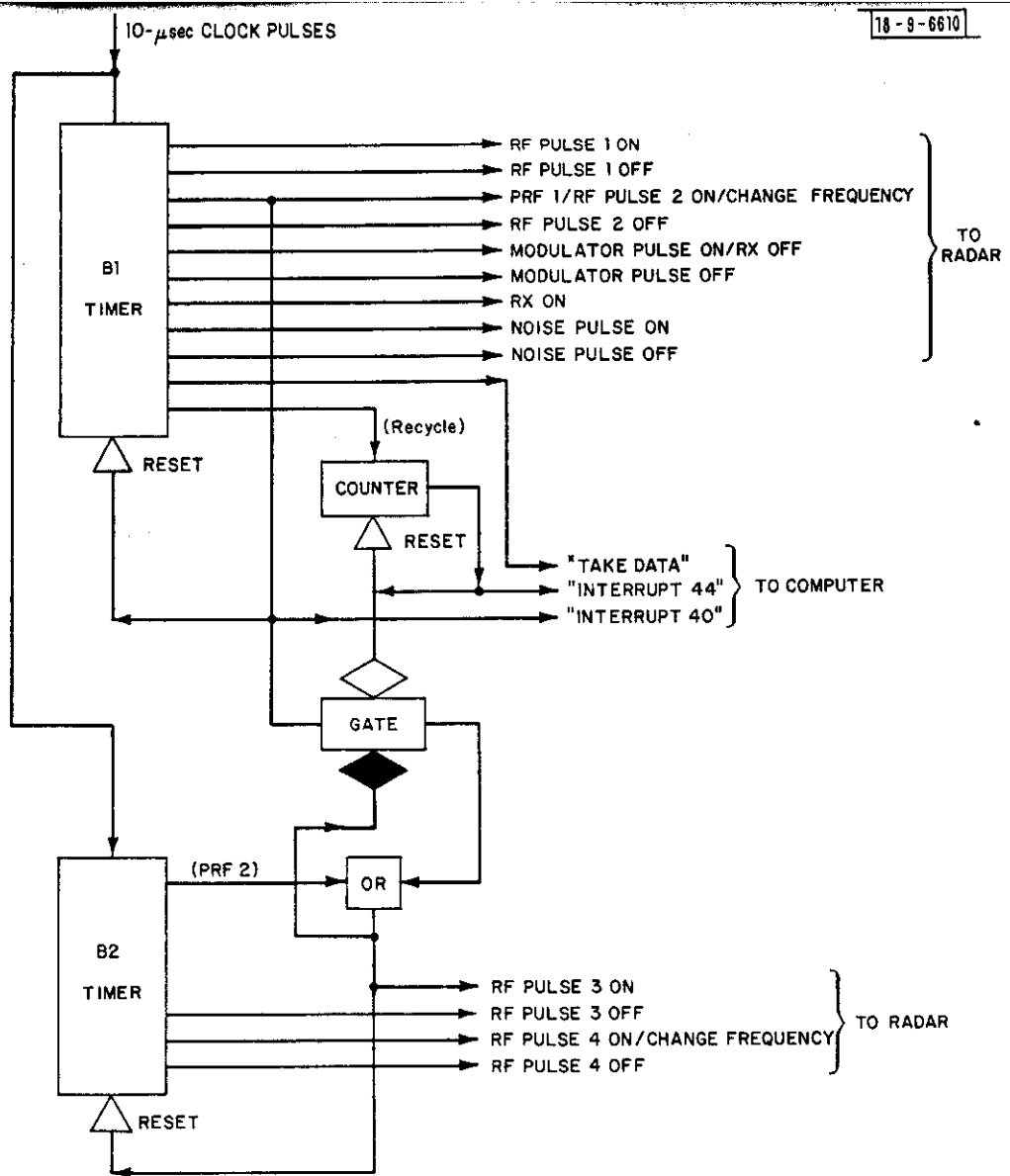


(c) Mode H.



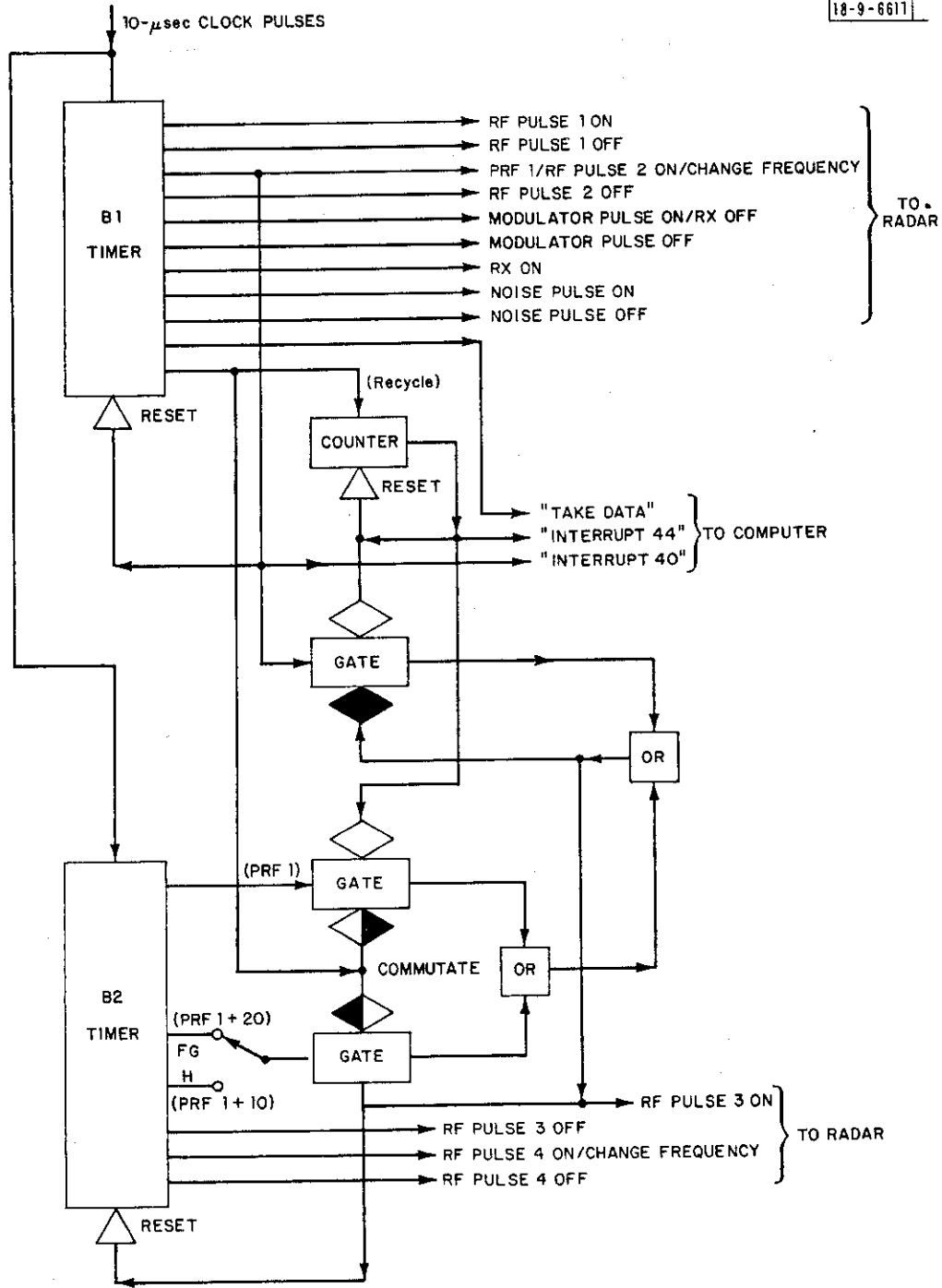
(d) Mode I.

Fig. 7(a-d). Continued.



(a) Original scheme; spacing increases after every sweep.

Fig. 8(a-b). Block diagrams showing method of generating RF pulses with right spacing (Fig. 6).



(b) Final scheme; spacing increases after every second sweep.

Fig. 8(a-b). Continued.

once in order to get an estimate of the clutter. Thus, the actual spacings employed are 0, 0, 20, 20, 40, 40, . . .  $\mu\text{sec}$  for the close-spaced pair of pulses and 200, 200, 220, 220, 240, 240, . . .  $\mu\text{sec}$  for the wide-spaced pair [Fig. 7(b)].

This change to the basic scheme of Fig. 8(a) is accomplished by arranging for the B2 timer to provide a pulse at 8.00 and 8.02 msec and commutating the reset-pulse generator between these two on alternate sweeps [Fig. 8(b)]. Thus, the B2 timer is made to retard with respect to the B1 timer only on every second radar sweep, and a total of 20 sweeps is now required to step through all spacings. Commutation of the frequencies is carried out at the end of each cycle of spacings. As in Mode E, this is performed by the computer on receipt of an "Interrupt 44" pulse (Figs. 5, 7, and 8). In Modes F and G, this frequency commutation prevents the close-spaced lags from being measured always on one frequency and the wide-spaced lags on the other. This would cause the two parts of the correlation function to be measured using different transmitter powers and receiver gains, with an inevitable disparity in the results.

### 3. Transmitter Control - Mode G

Mode G transmitter timing characteristics are shown in Table VII. Transmitter control is identical to Mode F transmitter control in all respects except that the length of all four pulses [Fig. 7(b)] is increased from 40 to 100  $\mu\text{sec}$ . As no clutter subtraction is needed in Mode G, the pulse transmissions need not be repeated as for the F Mode, but this repetition is retained for simplicity of timer operation. Mode G was the first one conceived, and the pulse lengths and spacing were then chosen to avoid overlap between pulses of different frequency and to best utilize the transmitter power available.

From Figs. 7(a) and (b) and Table VII, it can be seen that Mode E is very simply obtained from Mode G by disabling the B2 timer so that only the first pair of pulses is transmitted. This is the reason why the Mode E sync pulse is located at the leading edge of the second pulse rather than at the leading edge of the first (as in the H and I Modes). This also explains the superfluous E Mode frequency commutation and phase-detector commutation as outlined in Sec. 7 below.

### 4. Transmitter Control - Mode H

Mode H transmitter timing characteristics are shown in Table VII and Fig. 7(c). Owing to the longer pulse length and reduced maximum spacing employed, only a single pair of pulses is transmitted per sweep of the time base. Actually, since the maximum spacing (190  $\mu\text{sec}$ ) is less than the pulse length (200  $\mu\text{sec}$ ), the two pulses always overlap, i.e., a single pulse of length 200, 200, 210, 210, 220, 220, . . .  $\mu\text{sec}$ , etc., is transmitted on successive time-base sweeps as shown in the timing diagram of Fig. 7(c).

Due to the long H Mode pulse lengths, the ionospheric echoes are expected to extend out to delays where the noise samples are taken in the other modes. Accordingly, the transmitter frequency is altered on each sweep of the time base so that a pulse of a given length is transmitted first on one frequency and repeated on the second frequency. Samples free of ionospheric echoes may then be obtained by taking these from the alternate receiver channel. This change-over between channels is accomplished by controlling which pair of words from the analog-to-digital (A/D) converters (Fig. 5) is transmitted to the computer. The command to change channels is initiated by the radar timer by means of the "take-data" pulse. In effect, the radar

frequency is switched back and forth in advance of the sync pulse so that the delay between a pulse of a given frequency and the corresponding noise samples is approximately 15 instead of 7 msec.

#### 5. Transmitter Control - Mode I

Mode I transmitter timing characteristics are shown in Table VII and Fig. 7(d). These measurements were initially conducted using the original version of the B timer, which allowed adjustment of all transmitter timing parameters in the 10- $\mu$ sec steps. In this mode, only a single pulse is transmitted in order to minimize the delay required between the start of the transmission and the end of the receiver suppression. In order to compensate for the reduced number of measurements made per unit time, the interpulse period is reduced to 5 msec. This introduces the problem encountered in the H Mode that there is no place on the time base that can be considered completely free of echoes. Accordingly, the radar frequency is switched at a point along the time base defined by the "take-data" pulse [Fig. 7(d)] to the other channel. This allows samples of noise to be gathered approximately 9 msec after a pulse has been transmitted on a given frequency (instead of 4 msec). In Mode I, the "Interrupt 44" pulse is not used by the computer.

#### 6. Transmitter Modulator Control

The beam current in the klystron final amplifiers of the transmitter (and in the klystron penultimate amplifier) is controlled separately from the RF drive via a modulator pulse (Fig. 7, Table VII). In Modes E, F, G, and H, the transmitter modulator pulse is maintained a fixed length (600  $\mu$ sec) that is just long enough to encompass the widest pulse waveform used ( $\tau = 380 \mu$ sec for the G Mode). The "modulator-on" pulse precedes the sync pulse by 220  $\mu$ sec and is also used to initiate suppression of the receiver. In Mode I, the modulator pulse length is reduced to 220  $\mu$ sec (Table VII). In the RASEM mode, the long (600- $\mu$ sec) modulator pulse is wasteful, and provision is made to reduce it to 320  $\mu$ sec.

#### 7. Receiver Control

Table VIII summarizes the timing sequence insofar as it affects the receivers. As noted above, the receiver is suppressed at the time the modulator pulse is turned on. This is true for all modes. The receiver is restored to operation after the sync pulse at delays given in the table. Provision is made for manual control of the turn-on time; this is useful when the near-ground clutter returns are especially strong, causing receiver saturation.

The noise-calibration pulse, employed only in the E and I Modes, is placed at the end of the time base and turned off at the same time as the receiver. The "take-data" pulse is employed in the H and I Modes and marks the position on the time base where the computer starts accepting samples of noise, which in these modes are taken from the (alternate) channel containing noise only.

The sine and cosine channels of the phase detectors are commutated (via  $S_2$  of Fig. 4) in all modes except F. For Modes E, G, and H this commutation is carried out (by the computer) on receipt of every second Interrupt 44 pulse (i.e., every 40 sweeps for Modes E and G, every 80 sweeps for Mode H), and hence proceeds at half the rate of the frequency commutation. E Mode commutation performs no useful purpose but is implemented because of the way in

TABLE VIII RECEIVER TIMING CHARACTERISTICS					
Parameter	Mode				
	E	F	G	H	I
Interpulse Period (nominal) (msec)	8	8	8	8	5
RX ON (after sync) ( $\mu$ sec)	500	500	600	700	400
RX OFF (before sync) ( $\mu$ sec)	220	220	220	220	200
Noise Pulse ON (after sync) (msec)	7.0	NA	NA	NA	4.3
Noise Pulse OFF	At RX OFF	NA	NA	NA	At RX OFF
"Take-Data" Pulse (after sync) (msec)	NA (6.4)	NA (6.9)	NA (6.9)	6.9	3.9
Phase Detector Commutation	Every 40 sweeps	NA	Every 40 sweeps	Every 80 sweeps	Every 8 sweeps



which it is obtained by modifying Mode G timing only. In Mode I, the phase detectors are commutated every 8 sweeps. In this instance, the computer counts Interrupt 40 pulses to control commutation.

#### 8. Data-Sampling Control

The "sample-and-hold" circuits and associated digital voltmeters take samples of the signal voltages continuously at a 50-kHz rate in Modes E, F, and G. In the H and I Modes, the sample frequency is increased to 100 kHz (via  $S_1$  in Fig. 5). These clock pulses are also sent to the computer via the interface controller as requests for the computer to take data. On receipt of a "data-request" pulse, the computer sends "data-acknowledge" pulses to the digital multiplexer and format register (Fig. 5). These are spaced at 1.75- $\mu$ sec intervals, and transfer the digital words representing the sampled voltages into the computer. In Modes E, F, and G a request is made every 20  $\mu$ sec, and four words are transferred during the course of the following 10.5  $\mu$ sec. In Modes H and I the requests are at 10- $\mu$ sec intervals, and only two words are transferred into the computer during the following 7  $\mu$ sec. Choice of which pair of words is accepted governs which receiver channel is being sampled, and this is under control of the computer via the same output register (not shown in Fig. 5) used to commutate the frequencies and the phase detectors.

The interface controller (Fig. 5) serves to define the "data-request" pulses sent to the computer. In all modes, an Interrupt 40 pulse is used to initiate the train of samples via  $S_2$  in Fig. 5. The computer determines the length of the train by counting words and transmitting a "data-request-enable" pulse to the controller, which opens  $S_3$  when the correct number has been received. In Modes H and I this pulse also arranges for the "take-data" pulse to initiate a second train of "data-request" pulses so that the radar time base is sampled over two regions. The delays over which the data samples are obtained, together with the sample spacings, are listed in Table IX.

### B. REAL-TIME COMPUTER OPERATIONS

#### 1. General

In all modes of operation, the computer is required to answer requests to take data samples almost continuously. Accordingly, the functions of storing and processing data samples have been separated. The data samples for a given interval of time (defined in Table IX) are stored in one section of the memory, while the processing program is operating on the samples gathered during the previous period and stored in a different section. In other words, while data samples are being written into one area of the memory, the previous set is being processed in another area. In each mode, the length of the integration period is timed by the computer through counting Interrupt 40 pulses.

Each of the operating Modes E, F, G, H, and I uses two frequencies of transmission, each frequency corresponding to a separate, physical data channel containing an amplifier, a pair of phase detectors, a pair of low-pass filters, a pair of sample-and-hold circuits, a pair of A/D converters, and a pair of 10-bit storage registers (Figs. 4 and 5). The action of the phase detectors is to resolve the instantaneous receiver complex voltage  $\vec{v}(t)$  into orthogonal components  $|\vec{v}(t)| \cos \alpha$  and  $|\vec{v}(t)| \sin \alpha$ , where  $t$  is the time-base delay and  $\alpha$  is the phase difference between the received signal and the arbitrary phase-detector reference. Denoting the samples obtained in channel 1 as  $\vec{u}(t)$  and in channel 2 as  $\vec{v}(t)$ , the information presented to the computer on the  $i^{\text{th}}$  transmitter sweep is

**TABLE IX**  
**DATA-SAMPLING ARRANGEMENTS**

Parameter	Mode				
	E	F	G	H	I
Delay of First Data Sample Accepted by Computer (msec)	0.56	0.56	0.56	0.55	0.35
Spacing of Succeeding Samples ( $\mu$ sec)	20	20	20	10	10
Last Data Sample Accepted by the Computer for This Train of Samples (msec)	7.560	7.460	7.460	4.95	2.95
Delay to First Data Sample in Second Window (msec)	NA	NA	NA	6.90	3.9
Spacing of Succeeding Samples ( $\mu$ sec)	NA	NA	NA	10	10
Last Data Sample Accepted by the Computer for This Train of Samples (msec)	NA	NA	NA	7.50	4.59
Number of Sweeps Over Which Data Are Gathered Before Being Processed	2	2	1	1	4

**Note:** All delays are measured with respect to the Interrupt 40 pulse.

$$\begin{aligned}
x_1(t)_i &= |\vec{u}(t)_i| \cos \phi_i \\
y_1(t)_i &= |\vec{u}(t)_i| \sin \phi_i \\
x_2(t)_i &= |\vec{v}(t)_i| \cos \theta_i \\
y_2(t)_i &= |\vec{v}(t)_i| \sin \theta_i
\end{aligned} \tag{4}$$

where  $\phi_i$  and  $\theta_i$  are the phase differences from the phase-detector references on channels 1 and 2, respectively. The choice of when to take samples and how to process them depends upon the designed purposes of the individual modes. Not all the data samples gathered in Table IX are used, and Table X lists the delay intervals over which data processing is conducted and the uses to which the samples are put. The sections that follow describe the computer operations carried out while data samples are being received.

The altitudes quoted below for the various modes apply to data taken starting 16 December 1971 (see Sec. II-H). Prior to that date, it is necessary to modify these altitudes as indicated in Table III.

## 2. Computer Operations - Mode E

Mode E is employed to determine the echo power profile over the altitudes 92 to 677 km (Table III). To determine the echo power as a function of delay, the computer squares the input samples

$$\begin{aligned}
S_1(t)_i &= x_1^2(t)_i + y_1^2(t)_i = \vec{u}(t)_i \vec{u}^*(t)_i = |\vec{u}(t)_i|^2 \\
S_2(t)_i &= x_2^2(t)_i + y_2^2(t)_i = \vec{v}(t)_i \vec{v}^*(t)_i = |\vec{v}(t)_i|^2
\end{aligned} \tag{5}$$

The measured unnormalized power vs delay  $P_m(t)$  is then taken as the summation

$$P_m(t) = \sum_i S_1(t)_i + \sum_i S_2(t - 100 \mu\text{sec})_i \tag{6}$$

where the shift in delay by 100  $\mu\text{sec}$  allows for the time separation between the pulses transmitted at the two frequencies. The frequencies are actually commutated every 20 sweeps, and the 100- $\mu\text{sec}$  delay in reality alternates accordingly between channels. This complication has been ignored in the discussion in this section.

In general, the total power  $P_m(t)$  measured includes wanted ionospheric echo power, unwanted noise power, and unwanted clutter echo power. Denoting these by the subscripts s, n, and c, respectively,

$$P_m(t) = P_s(t) + P_n(t) + P_c(t) \tag{7}$$

The signal samples are correlated over intervals of the order of  $0 \leq \tau \leq \Delta f_1^{-1}$ , i.e., over an interval of less than 1 msec for the measurements described in this report. The noise samples are likewise correlated over an interval  $0 \leq \tau \leq b_{\text{eff}}^{-1}$ , where  $b_{\text{eff}}$  is the effective bandwidth of the receiver (45 kHz). It follows that the signal and noise samples are not correlated from sweep-to-sweep. Ground-clutter echoes, on the other hand, should be well correlated over an

TABLE X  
COMPUTER REAL-TIME SAMPLES

Parameter	Mode				
	E	F	G	H	I
Delay to First Echo Sample (msec)	0.68	0.74	1.18	1.55	0.35
Sample Spacing ( $\mu$ sec)	40	20	NA	NA	NA
Delay to End of This Train (msec)	1.24	0.86	NA	NA	NA
Delay to First Intermediate Echo Sample (msec)	1.30	NA	NA	NA	NA
Intermediate Sample Spacing ( $\mu$ sec)	60	NA	NA	NA	NA
Delay to End of This Train (msec)	2.38	NA	NA	NA	NA
Delay to Next Intermediate Echo Sample (msec)	2.48	0.90	NA	NA	NA
Sample Spacing ( $\mu$ sec)	100	40	100	200	10
Delay to End of This Train (msec)	4.58	1.14	2.18	3.55	0.91
First Noise Sample (msec)	6.50	6.96	6.96	6.95	4.00
Noise Sample Spacing ( $\mu$ sec)	40	20	20	10	10
Last Noise Sample (msec)	6.82	7.14	7.18	7.09	4.14
First Calibration Pulse Sample (msec)	7.20	NA	NA	NA	4.40
Calibration Pulse Sample Spacing ( $\mu$ sec)	40	NA	NA	NA	10
Last Noise Pulse (msec)	7.40	NA	NA	NA	4.49

**Note:** All delays are measured with respect to the Interrupt 40 pulse. Slight changes in these delays apply for data taken prior to 16 December 1971, resulting in small shifts in altitude - see Table III.

interval as short as 8 msec, so that an estimate of the echo power  $P_c(t)$  can be obtained by computing the amount of power that is correlated from sweep-to-sweep

$$P_c(t) = 2 \sum_i \vec{u}(t)_i \vec{u}^*(t)_{i+1} + 2 \sum_i \vec{v}(t - 100 \mu\text{sec})_i \vec{v}^*(t - 100 \mu\text{sec})_{i+1} \quad (8)$$

This expression is purely real if the clutter is perfectly correlated from sweep-to-sweep. The imaginary part of  $P_c(t)$  is not actually calculated, but is assumed to be zero. Here, the factor of 2 allows for the fact that the clutter is calculated only once for every pair of sweeps, i.e., only for  $i$  odd. The product  $\vec{u}(t)_i \vec{u}^*(t)_{i+1}$  can be expanded in terms of signal, noise, and clutter contributions

$$\begin{aligned} \vec{u}(t)_i \vec{u}^*(t)_{i+1} &= [\vec{u}_s(t)_i + \vec{u}_n(t)_i + \vec{u}_c(t)_i] \\ &\quad \cdot [\vec{u}_s^*(t)_{i+1} + \vec{u}_n^*(t)_{i+1} + \vec{u}_c^*(t)_{i+1}] \\ &= \vec{u}_s(t)_i \vec{u}_s^*(t)_{i+1} + \vec{u}_n(t)_i \vec{u}_n^*(t)_{i+1} \\ &\quad + \vec{u}_c(t)_i \vec{u}_c^*(t)_{i+1} + \text{cross products} \quad (9) \end{aligned}$$

The terms representing cross products of signal, noise, and clutter have arbitrary phase angles and hence have an expected mean value of zero. Similarly, since the signal and noise samples are uncorrelated from sweep-to-sweep, these terms also average out to zero

$$\sum_i \vec{u}_s(t)_i \vec{u}_s^*(t)_{i+1} = \sum_i \vec{u}_n(t)_i \vec{u}_n^*(t)_{i+1} \rightarrow 0 \quad (10)$$

On the other hand, the clutter echoes are essentially identical, i.e.,  $\vec{u}_c(t)_i \approx \vec{u}_c(t)_{i+1}$ . Thus,

$$\sum_i \vec{u}(t)_i \vec{u}^*(t)_{i+1} \approx \sum_i |u_c(t)_i|^2 \quad (11)$$

The simple clutter subtraction scheme proposed here represents a digital implementation of the standard moving-target-indicator (MTI) radar method of canceling reflections from stationary objects, which uses a delay line equal in length to the interpulse period to store signals from the previous sweep. The advantages of the digital approach are (a) the freedom to adjust the interpulse period to any desired value, (b) precise timing of the sampling is easier to achieve than delaying the signals by analog means, and (c) the current and delayed samples are treated identically so that there is no possibility of the receiver gain differing for the two.

The operation described above can be carried out more simply as

$$\begin{aligned} P_m(t) - P_c(t) &= \sum_i \vec{u}(t)_i [\vec{u}^*(t)_i - \vec{u}^*(t)_{i+1}] \\ &\quad + \sum_i \vec{v}(t - 100 \mu\text{sec})_i [\vec{v}^*(t - 100 \mu\text{sec})_i - \vec{v}^*(t - 100 \mu\text{sec})_{i+1}] \quad (12) \end{aligned}$$

but this has not been done. Since the clutter subtraction is performed only over the height range 92 to 176 km, it is not clear that a significant amount of computer time would be saved.

The clutter subtraction scheme described above effectively imposes a weighting of the applied signal spectrum of the form

$$H(f) = 1 - \cos(2\pi f/f_r) \quad (13)$$

where  $f$  is the frequency displacement from the radar frequency  $f_0$ , and  $f_r$  is the pulse repetition frequency (125 Hz). Thus, the admitted power will be zero at  $f_0 \pm mf_r$ , where  $m$  is any integer. If the echo power was distributed in frequency over an interval comparable to  $f_r$ , the action of this filtering would be to remove echo power selectively as a function of frequency. This occurs in Mode I, but for Mode E the echo bandwidth ( $\sim 3\Delta f_1$ ) is much larger than  $f_r$ .

Although data samples arrive at the computer every 20  $\mu$ sec (Table IX), products of the signal power for the second pulse transmitted are formed over the range  $0.68 \leq t \leq 1.24$  msec only at 40- $\mu$ sec intervals,  $1.30 \leq t \leq 2.38$  at 60- $\mu$ sec intervals, and  $2.48 \leq t \leq 4.58$  at 100- $\mu$ sec intervals, as listed in Table X. The clutter is estimated [via Eq. (8)] only over the first of these intervals.

To estimate the average noise  $\bar{P}_n(t)$ , the power is computed for nine samples at delays  $6.50 \leq t \leq 6.82$  msec spaced 40  $\mu$ sec apart. An average of these nine is taken as the mean noise level in the receiver, and this is assumed to be independent of  $t$ . A further six samples are taken of the sum of the noise and noise-calibration pulse  $P_{n+cal}(t)$  in the range  $7.20 \leq t \leq 7.40$  msec for power calibration in terms of temperature.

For the channel containing echoes from the first pulse transmitted, the same operations are carried out but for samples 100  $\mu$ sec earlier on the time base [Eqs. (6) and (8)].

An important error existed in the real-time computer operations throughout the 1969-1975 period covered by this report. The 100- $\mu$ sec delay which should be applied to the channel containing data from the first pulse transmitted was unfortunately applied to the other channel, with the result that the measured power profile was, in fact, an average of the desired measurement shifted up and down 15 km. This causes no problems in regions of linear power-profile gradient, but could be important near sharper profile features. This error was not discovered in time to attempt any correction in the analysis program.

### 3. Computer Operations - Mode F

Mode F is employed to determine the echo acf over the range  $0 \leq \tau \leq 380$   $\mu$ sec [a shorter maximum lag applies at higher altitudes - see Fig. 1(a)] for altitudes  $106 \leq h \leq 166$  km (Table III). Description of computer operations is facilitated by initially ignoring channel commutation, i.e., assume for the moment that the close-spaced pulse pair is sampled in channel 1 (u channel) and the wide-spaced pair in channel 2 (v channel). In this case, the total unnormalized measured acf can be calculated as

$$P_m(t, \tau) = \sum_i [x_1(t)_i x_1(t + \tau)_i + y_1(t)_i y_1(t + \tau)_i] \quad 0 \leq \tau \leq 180 \mu\text{sec}$$

$$P_m(t, \tau) = \sum_i \{x_2(t - 100 \mu\text{sec})_i x_2(t + \tau - 100 \mu\text{sec})_i + y_2(t - 100 \mu\text{sec})_i y_2(t + \tau - 100 \mu\text{sec})_i\} \quad 200 \leq \tau \leq 380 \mu\text{sec} \quad (14)$$

Thus, the acf's computed in Mode F are assumed to be wholly real. This amounts to assuming that the vertical drift velocity for the altitudes covered by this mode is negligibly small.

$P_m(t, \tau)$  includes contributions due to signal, clutter, and noise

$$P_m(t, \tau) = P_s(t, \tau) + P_n(t, \tau) + P_c(t, \tau) \quad (15)$$

The clutter component is computed via (see Sec. 2 above for discussion of clutter subtraction technique)

$$P_c(t, \tau) = 2 \sum_i [x_1(t)_i x_1(t + \tau)_{i+1} + y_1(t)_i y_1(t + \tau)_{i+1}] \quad 0 \leq \tau \leq 180 \mu\text{sec}$$

$$P_c(t, \tau) = 2 \sum_i [x_2(t - 100 \mu\text{sec})_i x_2(t + \tau - 100 \mu\text{sec})_{i+1} + y_2(t - 100 \mu\text{sec})_i y_2(t + \tau - 100 \mu\text{sec})_{i+1}] \quad 200 \leq \tau \leq 380 \mu\text{sec} \quad (16)$$

That is, the first sample on one sweep is multiplied by the second sample on the next sweep. The factor of 2 in Eq. (16) allows for the fact that the operation is only carried out for every pair of sweeps, i.e., only for odd  $i$ .

The noise acf is measured using samples at the end of the sweep starting at  $t = 6.96$  msec. Only the channel containing the close-spaced pair samples is used for this measurement. A sufficient number of samples is taken to form several entire noise acf's per sweep. To be specific, 10 independent complete acf's are computed per sweep when the pulse spacing is  $0 \leq \tau \leq 80 \mu\text{sec}$  and 5 per sweep for  $100 \leq \tau \leq 180 \mu\text{sec}$ , giving 75 noise acf measurements for each profile of echo acf measurements (10 time-base sweeps).

$$P_n(\tau_n)_i = \sum_{j=0}^m [x_1(t + j\Delta\tau_n)_i x_1(t + j\Delta\tau_n + \tau_n)_i + y_1(t + j\Delta\tau_n)_i y_1(t + j\Delta\tau_n + \tau_n)_i]$$

$$P_n(\tau_n) = 1/75 \sum_i P_n(\tau_n)_i \quad (17)$$

with  $m = 9$  for  $0 \leq \tau \leq 80 \mu\text{sec}$  and  $m = 4$  for  $100 \leq \tau \leq 180 \mu\text{sec}$ , and  $i$  representing sweep number. Equation (17) applies for  $0 \leq \tau_n \leq 100 \mu\text{sec}$  and  $\Delta\tau_n = 20 \mu\text{sec}$ . For  $\tau \geq 100 \mu\text{sec}$ ,  $P_n(\tau) \rightarrow 0$ , and hence there is no purpose in forming further products. Equation (17) assumes  $P_n(\tau)$  to be real. The numbers 4, 9, and 75 applying to the above equation must be changed to 0, 0, and 10 for data prior to 6 November 1970 (Table XI).

The lags of the acf from which the greatest amount of physical information may be obtained are those near the first zero crossing and first minimum of the function. In order to increase accuracy at these lags, additional sample multiplications are made near them. While it is possible to achieve this simply by repeating the desired spacing transmissions more often than the others, the timing equipment constructed at Millstone does not lend itself to this. An alternate approach is to average with respect to height at these lags. In the F Mode, this is carried out at altitudes  $h \geq 130$  km (and all altitudes before 30 December 1970) for  $\tau \geq 100 \mu\text{sec}$ . The additional correlations computed are for altitudes  $\pm 3$  km with respect to the wanted one. The values  $t$  and  $\tau$  employed are shown in Fig. 1(a) where the values of delay tabulated are for the first sample of any pair. The location of the second sample is obtained by adding the value of  $\tau$  to

TABLE XI NUMBER N OF NOISE-CORRELATION FUNCTIONS FORMED PER SWEEP IN MODES F, G, AND H					
Mode		Close-Spaced Pair Pulse Spacing $\tau$ ( $\mu\text{sec}$ )			Total in 20 Sweeps
F	$\tau$	0 to 80	100 to 180		
	N	10 (1)	5 (1)		150 (40)
G	$\tau$	0 to 40	60 to 100	120 to 180	
	N	12 (1)	4 (1)	1 (1)	104 (40)
H	$\tau$	0 to 40	50 to 90	100 to 190	
	N	15 (1)	10 (1)	5 (1)	350 (40)

Note: Numbers in parentheses apply to data taken before 6 November 1970.

the corresponding delay. Figure 1(a) shows that correlation functions are obtained every 3 km (6 km before December 1970) between  $106 \leq h \leq 124$  km, and thence every 6 km over  $130 \leq h \leq 166$  km. For the lower group, no height averaging is carried out starting 30 December 1970 in order to preserve the full height resolution of the measurements. For the higher group, the correlation is not computed for  $\tau = 380 \mu\text{sec}$  in order to save some computer time. Figure 1(a) ignores the shift of  $100 \mu\text{sec}$  in the location of the first pulse for  $\tau \geq 200 \mu\text{sec}$ . In practice, this is taken into account.

Since the roles of the frequency channels are commutated every 20 sweeps, it is evident that the close-spaced pair will appear in channel 1 for 20 sweeps, then in channel 2 for 20 sweeps; hence, it is necessary to reverse the roles of  $u$  and  $v$  in Eqs. (14) through (17) every 20 sweeps.

#### 4. Computer Operations - Mode G

Mode G is employed to determine the echo acf over the range  $0 \leq \tau \leq 380 \mu\text{sec}$  [a shorter maximum lag applies at higher altitudes - see Fig. 1(b)] for altitudes  $167 \leq h \leq 317$  km (Table III). This range of altitudes is not normally contaminated by unwanted clutter echoes. Accordingly, no attempt is made to subtract clutter correlation, and, instead, the available computer time is used to compute the full, complex acf in order to obtain the plasma drift information contained in the imaginary part. This imaginary part is calculated only for  $0 \leq \tau \leq 180 \mu\text{sec}$  as the drift information content decreases as the real part becomes small. The difference between the real part and magnitude is ignored for  $200 \leq \tau \leq 380 \mu\text{sec}$ . Also, as no clutter subtraction is needed in this mode, each sweep is processed independently.

Aside from these basic differences, F and G Mode computer operations are largely the same, the remaining differences being those of timing, height averaging, and number of noise acf's calculated as given in Fig. 1 and Tables IX through XI.



The full acf is calculated (once again ignoring channel commutation as in the previous section) as

$$\bar{P}_m(t, \tau) = \sum_i \vec{u}(t)_i \vec{u}^*(t + \tau)_i \quad 0 \leq \tau \leq 180 \mu\text{sec} \quad (18)$$

$$P_m(t, \tau) = \sum_i \text{Re} [\vec{v}(t - 100 \mu\text{sec})_i \vec{v}^*(t + \tau - 100 \mu\text{sec})_i] \quad 200 \leq \tau \leq 380 \mu\text{sec} \quad (19)$$

Commutation of the close- and wide-spaced pulse pairs between frequency channels has the effect of reversing the roles of  $u$  and  $v$  in Eqs. (18) and (19) every 20 sweeps.

As in Mode F,  $P_n(\tau)$  is assumed to be a purely real function as the receiver bandpass was designed to be symmetric about its center frequency. This has been found to be not completely true. Enough asymmetry exists to cause an important systematic distortion in  $\text{Im}[\bar{P}_m(t, \tau)]$ . Appendix A discusses the effect of ignoring the imaginary part of the noise acf upon the data analysis results.

#### 5. Computer Operations - Mode H

Mode H is employed to determine the echo acf over the range  $0 \leq \tau \leq 190 \mu\text{sec}$  [a shorter maximum lag applies at higher altitudes - see Fig. 1(c)] for altitudes  $215 \leq h \leq 515 \text{ km}$  (Table III).

As in Mode G, clutter need not be considered at these altitudes, and the full, complex correlation function is measured [i.e., Eq. (18)] for all lags  $0 \leq \tau < 190 \mu\text{sec}$ . G and H Mode computer operations are largely the same, the differences being those of timing, height averaging, and number of noise acf's calculated as given in Fig. 1 and Tables IX through XI.

#### 6. Computer Operations - Mode I

Mode I is employed to determine the echo power profile over the range  $55 \leq h \leq 140 \text{ km}$  (Table III). I Mode processing follows along the general lines of E Mode processing, but several major differences exist. Most of these differences arise due to the transmission of alternate frequencies on alternate sweeps and measurement of signal-plus-noise and noise-only on opposite frequencies on a given sweep. This necessitates processing of sweeps in groups of four at a time for clutter subtraction purposes to retain in the computer a pair of sweeps on each frequency. Thus, the equation for Mode I corresponding to Eq. (6) for Mode E becomes

$$P_m(t) = \sum_{\substack{i \\ \text{odd}}} S_1(t)_i + \sum_{\substack{i \\ \text{even}}} S_2(t)_i \quad (20)$$

and, corresponding to Eq. (8), we have

$$P_c(t) = 2 \sum_i [\vec{u}(t)_i \vec{u}^*(t)_{i+2} + \vec{v}(t)_{i+1} \vec{v}^*(t)_{i+3}] \quad (i-1)/4 \text{ an integer} \quad (21)$$

As with Mode E, only the real part of  $P_c(t)$  is actually calculated. Clutter is subtracted at all altitudes in the I Mode.

A separate version of the Mode I program was developed in which the transmitter was switched to a frequency outside the receiver passband during four consecutive sweeps out of every eight. The integration was allowed to proceed as normal, except that these sweeps were stored separately from the others. In this way, the recovery of the receiver could be monitored, albeit at

a cost of half the integration time. Using this program, it was found that by an altitude of 60 km the receiver had essentially recovered; hence, the original version of the program, that does not attempt to monitor the receiver recovery, was reverted to.

### C. REAL-TIME COMPUTER OUTPUT

#### 1. General

At the termination of each experimental integration period, the integrated power and acf results are first written onto magnetic tape. A mixed BCD and binary format is employed in which the data heading is in BCD and the results themselves are in binary. Then, for the purpose of providing a real-time printed copy of these results, the computer performs a modest amount of processing to reduce the information to an immediately meaningful form. Also, the computer oscilloscope display provides a real-time visual presentation of the primary results. The following sections discuss these operations in more detail.

#### 2. Computer Output - Modes E and I

At the termination of the integration process, the computer has determined  $P_m(t)$ ,  $P_n(t)$ ,  $P_c(t)$ , and  $P_{n+cal}(t)$  at delays  $t$  given in Table X. These data are saved on magnetic tape. Several calculations are now made for output on the line printer only. The mean receiver noise level  $\bar{P}_n$  is estimated by averaging  $P_n(t)$  over  $t$ , and the mean noise plus calibration-pulse level  $\bar{P}_{n+cal}$  is estimated by averaging  $P_{n+cal}(t)$  over  $t$ .

Ionospheric signal power  $P_s(t)$  is then calculated as

$$P_s(t) = P_m(t) - \bar{P}_n - P_c(t) \quad (22)$$

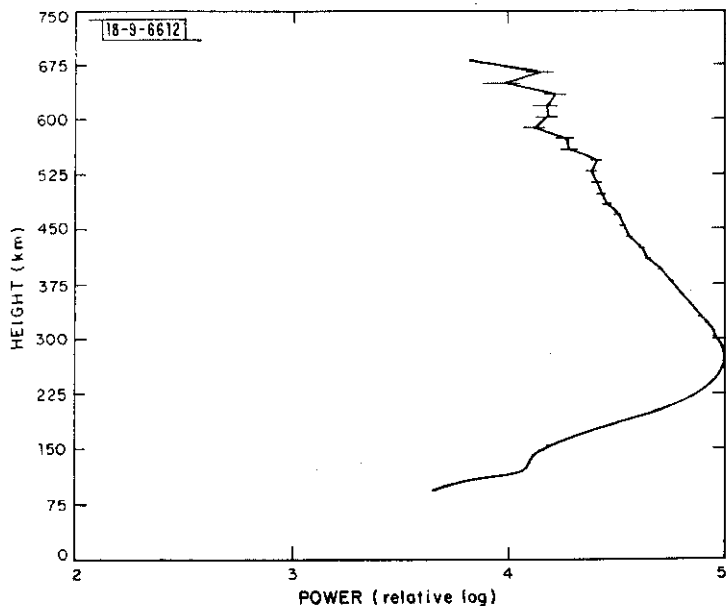
$P_s(t)$  is multiplied by  $h^2$ , the logarithm (base 10) is then taken, and the result is arbitrarily normalized to a maximum value of 5 to yield a height profile of the logarithm of relative scattered power. Error estimates of these power values are calculated from signal-to-noise and integration-time considerations (Appendix B). Signal temperature  $T_s(t)$ , noise-plus-clutter temperature  $T_{n+c}(t)$ , and noise (system) temperature  $T_n$  are calculated from the relationships

$$\begin{aligned} T_s(t) &= P_s(t)/T_n \\ T_{n+c}(t) &= \frac{[P_n(t) + P_c(t)]}{T_n} \\ T_n &= \frac{\bar{P}_{n+cal} - \bar{P}_n}{100 \text{ K}} \quad (23) \end{aligned}$$

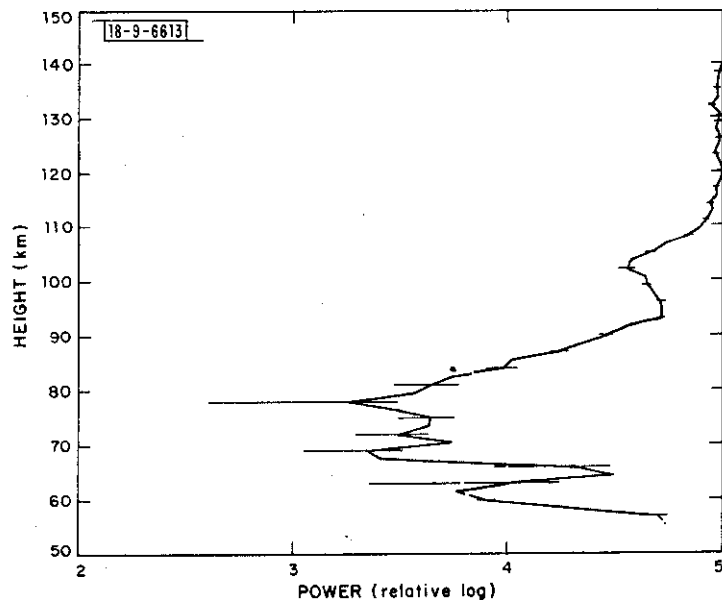
Altitude  $h$  is calculated as

$$h = 150\left(t - \frac{T + D}{2}\right) \quad \text{km} \quad (24)$$

where  $T$  is the radar pulse length and  $D$  is the delay introduced by the receiver ( $\sim 0.03$  msec);  $t$ ,  $T$ , and  $D$  are measured in milliseconds for this equation. The line printer listing consists of header information  $T_n$ , and lists of  $h$ ,  $T_{n+c}$ ,  $T_s$ , and scatter power plus its upper and lower standard-deviation error bounds (relative logarithms) vs  $t$ . The oscilloscope displays  $P_m(t)$



(a) Mode E.



(b) Mode I.

Fig. 9(a-b). Logarithm of scattered power, normalized to a maximum of 5.

and  $P_c(t)$  and scattered power (relative logarithm) vs  $h$ . Figure 9(a) is an example of a scattered-power profile obtained by Mode E; Fig. 9(b) is a Mode I example.

### 3. Computer Output - Mode F

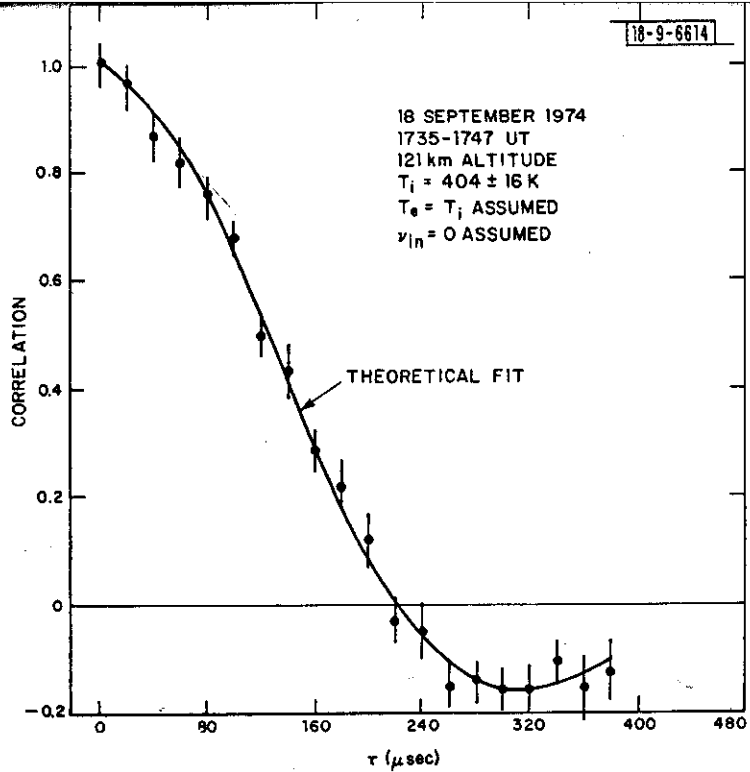
At the termination of the integration process, the computer has determined  $P_m(t, \tau)$ ,  $P_n(t, \tau)$ , and  $P_c(t, \tau)$  at delays  $t$  and  $\tau$  listed in Tables III and X. These data are saved on magnetic tape. Several calculations are now made for output on the line printer only. The mean receiver noise power correlation function  $\bar{P}_n(\tau)$  is estimated by averaging  $P_n(t, \tau)$  over  $t$ . The signal power correlation functions are then calculated as

$$P_s(t, \tau) = P_m(t, \tau) - \bar{P}_n(\tau) - P_c(t, \tau) \quad (25)$$

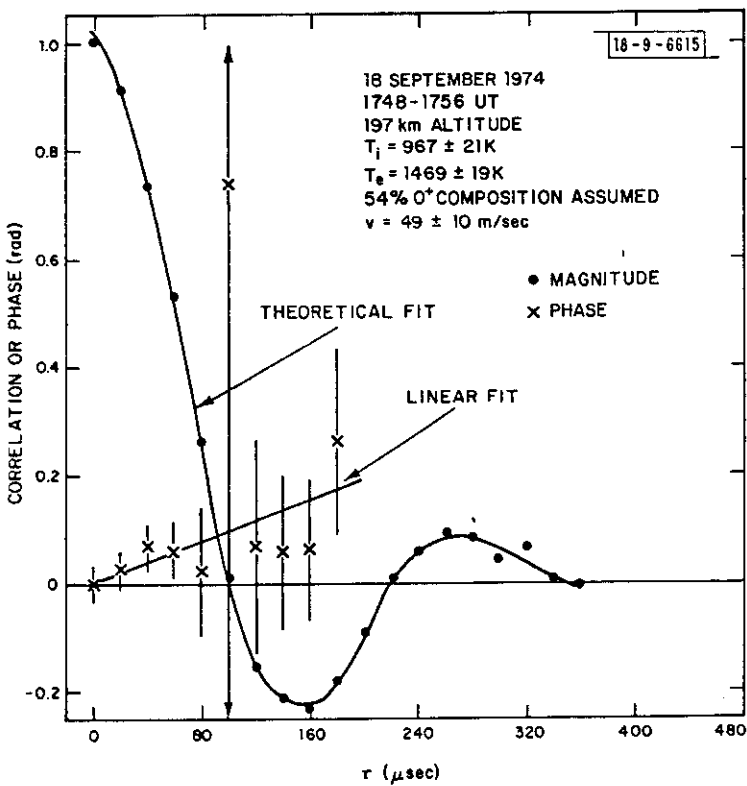
and corrected for instrumental smearing as discussed in Appendix A. Altitude  $h$  is computed via Eq. (24). The line printer listing consists of header information plus tables of  $P_s(t, \tau)/P_s(t, 0)$  and  $P_c(t, \tau)/P_s(t, 0)$  vs  $h$  and  $\tau$ , and a list of  $\bar{P}_n(\tau)/P_n(0)$  vs  $\tau$ . [For these tables, the values of  $P_s$  are those corrected for instrumental smearing (described in Appendix A) and not as given directly by Eq. (25).] Finally, a list of  $h^2 P_s(t, 0)$  vs  $h$ , normalized to a maximum of unity, is printed. This latter list was replaced starting April 1974 by a list vs  $h$  of  $P_s(t, 0)/\bar{P}_n(0)$  (S/N). The oscilloscope displays  $P_s(t, \tau)/P_s(t, 0)$  vs  $\tau$  for each  $t$  used. Figure 9(c) is an example of a measured Mode F acf. The best-fit theoretical function is also shown (see Sec. V).

### 4. Computer Output - Modes G and H

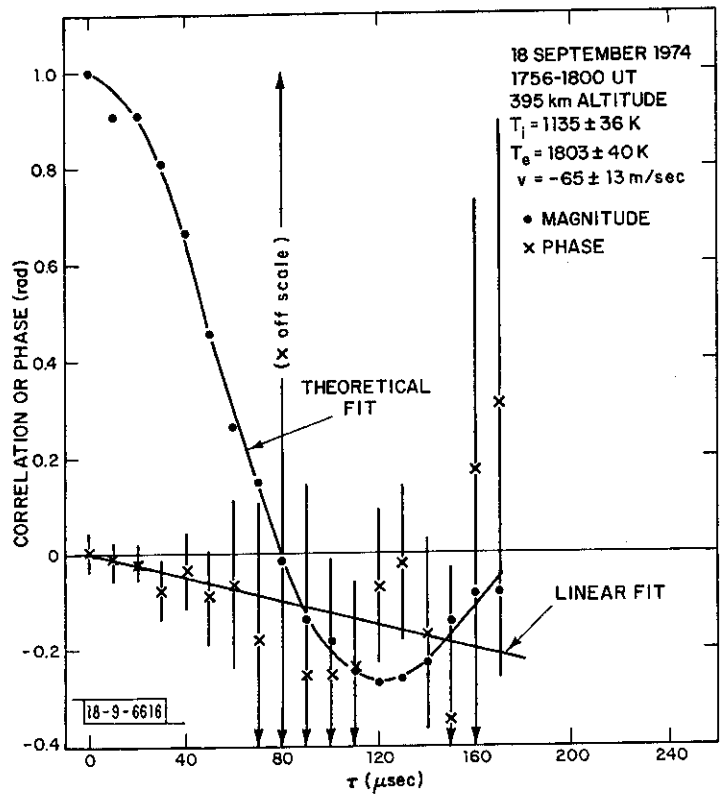
At the termination of the integration process, the computer has determined  $\bar{P}_m(t, \tau)$  for  $\tau \leq 190 \mu\text{sec}$ ,  $R_e[\bar{P}_m(t, \tau)]$  for  $\tau \geq 200 \mu\text{sec}$  (Mode G), and  $P_n(t, \tau)$  at delays  $t$  and  $\tau$  given in Tables III and X. These data are saved on magnetic tape. Several calculations are now made for output on the line printer only. The mean receiver noise power correlation function  $\bar{P}_n(\tau)$



(c) Mode F.



(d) Mode G.



(e) Mode H.

Fig. 9(c-e). Measured correlation function and fitted theoretical function.

is estimated by averaging  $\bar{P}_n(t, \tau)$  over  $t$ . The magnitude  $M(t, \tau)$  and phase  $\phi(t, \tau)$  of the signal power correlation function  $\bar{P}_s(t, \tau)$  are calculated as

$$M(t, \tau) = |\bar{P}_s(t, \tau)| = \left[ \left( \{\text{Re} [\bar{P}_m(t, \tau)]\}^2 + \{\text{Im} [\bar{P}_m(t, \tau)]\}^2 \right)^{1/2} - \bar{P}_n(\tau) \right] \quad (26)$$

$$\phi(t, \tau) = \arctan \left\{ \frac{\text{Im} [\bar{P}_s(t, \tau)]}{\text{Re} [\bar{P}_s(t, \tau)]} \right\} \quad (27)$$

choosing  $\phi$  to lie in the quadrant  $\pm\pi/2$ .

$\text{Im} [\bar{P}_s(t, \tau)]$  is assumed to be zero for  $\tau \geq 200 \mu\text{sec}$  (Mode G).  $\phi$  is then interpreted as a velocity at each altitude via

$$v = \frac{\lambda}{4\pi} \frac{d\phi}{d\tau} \quad (28)$$

where  $d\phi/d\tau$  is taken to be the slope of the line passing through  $\phi(t) = 0$ ,  $\tau = 0$ , and the weighted center of the remaining points<sup>16</sup>

$$\frac{d\phi}{d\tau} = \frac{\sum_{\tau} \tau \phi(\tau) M^2(\tau)}{\sum_{\tau} \tau^2 M^2(\tau)} \quad (29)$$

This equation approximates the uncertainty in  $\phi(\sigma_\phi)$  by  $1/M$  to avoid the complicated rigorous calculation of  $\sigma_\phi$  (Appendix B).

$M$  is corrected for instrumental smearing as discussed in Appendix A. Altitude  $h$  is calculated via Eq. (24).

The line printer listing consists of header information plus tables of  $M(t, \tau)/M(t, 0)$  and  $\text{Im} [\bar{P}_s(t, \tau)]/M(t, 0)$  vs  $h$  and  $\tau$ , plus a list of  $\bar{P}_n(\tau)/\bar{P}_n(0)$  vs  $\tau$ , where, again, the values of  $M$  used are those corrected for instrumental effects. Finally, lists of  $v$  and  $h^2 M(t, 0)$  (normalized to a maximum of unity) vs  $h$  are printed. This latter list was replaced in April 1974 by a list of  $M(t, 0)/\bar{P}_n(0)$  vs  $h$  (S/N). Figures 9(d) and (e) are examples of measured Mode G and H acf's. Fitted theoretical functions are also shown (see Sec. V).

## V. ANALYSIS

### A. GENERAL

The real-time magnetic-tape output from a 2-pulse experiment consists of signal, noise, and clutter power as a function of time base and correlation delays. A separate program is used to analyze these data to determine the physical quantities of the ionosphere such as electron density  $N_e$ , electron and ion temperature  $T_e$  and  $T_i$ , percentage atomic ions  $[O^+]/N_e$ , vertical drift  $V_d$ , and ion-neutral collision frequency  $\nu_{in}$ . The program also calculates from these a number of parameters concerning the neutral atmosphere, namely, the abundance of molecular nitrogen  $[N_2]$ , atomic oxygen  $[O]$ , and the neutral temperature  $T_n$ . The results of this analysis are saved on magnetic tape, and a library of such results is available for distribution to the scientific community. The following sections describe the analysis procedures applied to the 2-pulse data.

One note will be entered here for completeness. The analysis program was written to analyze F Modes containing 14 heights, but prior to 30 December 1970 only 11 heights were measured (Sec. II-H). For the 11-height F Modes, the three missing altitudes are created in the analysis program by averaging the two neighboring altitudes. These created heights [second, fourth, and sixth in Fig. 1(a)] do not yield additional independent information. It should also be realized that as the first 7 heights in the 14-height F Mode are at 3-km intervals whereas  $\Delta h = 6$  km at best (Table III), these same three altitudes (second, fourth, and sixth) have only a small degree of independence, and that due to independent noise estimates, not additional echo-signal measurements.

### B. POWER-PROFILE ANALYSIS

#### 1. Mode E - Routine Analysis

Mode E is used to measure the power profile, from which  $N_e(h)$  is deduced. The analysis program first calculates  $h$  via Eq. (24) and  $P_s(h)$  via Eq. (22).  $P_s$  and electron density  $N_e$  are related via a radar equation which, in the case of a monostatic radar system employing a conventional vertically directed parabolic antenna, may be written<sup>9</sup>

$$P_s = \frac{0.76 P_t A L c T}{16\pi} \frac{N_e \sigma}{h^2} \quad (30)$$

where

- $P_t$  = peak transmitter power,
- $A$  = effective antenna aperture,
- $L$  = waveguide and other losses, and
- $\sigma$  = scattering cross section per electron.

As discussed in Ref. 9, provided  $T_e/T_i \leq 3.0$ , the scattering cross section per electron may be written

$$\sigma = \frac{\sigma_e}{(1 + \alpha^2)(1 + T_e/T_i + \alpha^2)} \quad (31)$$

$$\sigma = \frac{4\pi D_e}{\lambda} \quad (32)$$

$$D_e = 69 \sqrt{T_e/N_e} \quad \text{m} \quad (33)$$

In Eq. (31),  $\sigma_e$  is the radar cross section for a free electron, which, in the case of back-scattering, is  $\sigma_e \approx 10^{28} \text{ m}^2$  (Ref. 9).

From these expressions, it may be seen that

$$P_s \propto \frac{N_e}{(1 + \alpha^2)(1 + T_e/T_i + \alpha^2)} \quad (34)$$

For typical  $N_e$  and  $T_e$ ,  $D_e \leq 1 \text{ cm}$  for heights below about 500 km. Thus at our wavelength  $\alpha^2 \leq 0.03$  and may be ignored, yielding

$$P_s \propto \frac{N_e}{1 + T_e/T_i} \quad h \leq 500 \text{ km} \quad (35)$$

This approximation breaks down at higher altitudes, and allowance must then be made for the altitude variation of  $\alpha$  (Ref. 1), but Eq. (35) is used in the present 2-pulse data analysis.

Equation (35) shows that it is necessary to correct the power profile for  $T_e/T_i$  profile variation to find  $N_e(h)$ . These temperature data are obtained from Modes F, G, and H following Mode E, ignoring the time difference between mode measurements. As the power profile is generally much smoother than the  $T_e/T_i$  profile, the temperature data are edited to remove unreasonable values (requiring  $0.5 \leq T_e/T_i \leq 4$ ) and some profile smoothing is applied (the smoothing algorithm has changed during development of the analysis program — basically, a 2- or 3-point smoothing has been used) to try to maintain a smooth  $N_e$  profile. Linear interpolation between these smoothed  $T_e/T_i$  values to the heights of  $N_e$  measurement is used. Application of the  $T_e/T_i$  correction yields an unnormalized density profile.

The constant of proportionality in Eq. (35) must also be determined to derive the absolute density profile from the unnormalized density profile. It has been the practice to determine this constant through simultaneous measurements of the critical frequency  $f_oF2$  of the F2-region from which the peak density  $N_{\text{max}}^{F2}$  may be established via

$$N_{\text{max}}^{F2} = 1.24(f_oF2)^2 \times 10^{10} \quad \text{m}^{-3} \quad (36)$$

where  $f_oF2$  is in megahertz. These critical frequency measurements are made using an on-site vertical-incidence ionosonde; similar measurements from Ottawa, Wallops Island, Billerica (Massachusetts), and Maynard (Massachusetts) have been considered when available to correct faulty local readings.<sup>17</sup> All these readings are plotted vs time, and a curve is drawn by hand through them. From this smooth curve, values are read off at half-hour intervals. Linear interpolation in time between these half-hour values is used to normalize the E Mode  $N_e$  profile at the midpoint of its integration time.

Statistical uncertainties in the power measurements, the still larger uncertainties in the  $T_e/T_i$  corrections applied to them, plus the use of discrete-height measurement cause some uncertainty in determining the exact point on the unnormalized  $N_e$  profile to which  $f_oF2$  normalization should be applied. This is resolved by fitting a parabola to the  $\log_{10} N_e$  (unnormalized) profile over the eight consecutive heights for which the sum of these logarithms maximizes. The vertex of the parabola marks the desired point of normalization, specifying the height  $h_{\text{max}}$  of the peak and the unnormalized  $N_e$  value corresponding to the density  $N_{\text{max}}^{F2}$ . Occasionally,

bad points (due to satellite echoes, ground clutter, etc.) cause this method to go astray, and occasional instances of improperly normalized profiles occur.

At the higher Mode E altitudes, the signal sometimes becomes so weak that the data are quite scattered. As the topside ionosphere  $N_e$  profile is expected to decrease nearly exponentially with increasing  $h$ , with its scale height increasing only slowly as temperatures increase and mean ion mass and the pull of gravity decrease, it has been felt that the true high-altitude densities could be more accurately represented by a parabola fit to the logarithm of the data in this region. A straight line is fitted instead of a parabola if the slope of the parabola appears to decrease with altitude (decreasing scale height) or the parabola vertex is below the maximum height of measurement. The lowest altitude for which the parabola fit is substituted for the data is set at 150 km above the F2 peak in some program versions and 516 km (i.e., just above highest Mode H altitude) in others. The parabola fit also takes into account the data up to 50 km below this lowest height to insure smooth transition from the real data profile to the smoothed fit, but the original data in this 50-km interval are retained and not replaced by the fit.

Occasionally, a satellite echo causes this high-altitude smoothing scheme to yield unreasonable results. Efforts made to cull out these bad points have not been very successful, and, occasionally, a distorted profile smoothing results.

## 2. Mode E - RASEM Analysis

RASEM analysis is identical to the routine Mode E analysis just described except for certain facets of data smoothing, temperature correction, and normalization.

No profile smoothing is applied to RASEM data, but because the integration time is short, smoothing in time is applied to reduce run-to-run fluctuations. For the  $i^{\text{th}}$  run in time, the signal power  $P_s(h)_i$  is replaced by a weighted time average  $\bar{P}_s(h)_i$

$$\bar{P}_s(h)_i = \frac{\sum_{j=i-n}^{i+n} W_j P_s(h)_i}{\sum_{j=i-n}^{i+n} W_j}$$

$$W_j = 2(n - |j - i|) + 1$$

$$\sum_{j=i-n}^{i+n} W_j = (n + 1)^2 + n^2 \quad . \quad (37)$$

This provides a triangular weighting over  $2n + 1$  points. Values  $n = 0, 1, 2, 5,$  and  $10$  have been employed. This smoothing process truncates the data series somewhat, since the first possible weighted average that can be formed is for  $i = n + 1$  and the last is for  $i = N - (n + 1)$  for a total of  $N$  runs.

As no temperature data are gathered during a RASEM experiment, the density-profile temperature correction is modeled:

$$(a) \quad T_e/T_i = 1 \quad h \leq 130 \text{ km}$$

$$(b) \quad T_e/T_i \text{ increases linearly to } 2 \quad 130 \leq h \leq 300 \text{ km}$$

$$(c) \quad T_e/T_i \text{ decreases linearly to } 1.2 \quad 300 \leq h \leq 2000 \text{ km}$$



As in the regular Mode E analysis, a parabola fit determines the point for profile normalization to ionosonde readings. However, the ionosonde readings are taken every half-hour while RASEM measurements are made much more frequently (e.g., every 2 min.). Rather than attempt to determine  $N_{\max}^{F2}$  [Eq. (36)] for each profile, we make use of the inherent stability of the radar. This should serve to maintain  $\log_{10} N_{\max}^{F2} - \log_{10} P_s(h_{\max})$  approximately constant from run-to-run. Thus, the difference

$$r = \log_{10} N_{\max}^{F2} - \log_{10} P_s(h_{\max}) \quad (38)$$

is formed for all the available values of  $N_{\max}^{F2}$  throughout the run (i.e., every half-hour).

As the radar sensitivity is likely to drift slowly with time, a least-mean-square straight line is fitted to the available values of  $r$  to yield the time variation of this parameter  $\bar{r}(t)$ . The electron density profile at any time  $t$  is then obtained using

$$\log_{10} N_e(h) = \log_{10} P_s(h) + \log_{10} \left[ \frac{1 + (T_e/T_i)(h)}{1 + (T_e/T_i)(h_{\max})} \right] + \bar{r}(t) \quad (39)$$

Contour plots of  $\log_{10} N_e$  vs  $h$  and  $t$  can be provided by the processing program.

Difficulties have been encountered with the program when the F1-layer has been pronounced (usually following a magnetic storm in summer). It is then possible for the F1 peak to be mistaken for the F2 both in obtaining  $r$  and  $h_{\max}$ . These events are sufficiently infrequent that attempts to make the program cope with them have not been made.

### 3. Mode I

The Mode I results are converted to an  $N_e$  profile in much the same manner as the routine Mode E results, except that it is assumed that  $T_e = T_i$  at all altitudes and the normalization is made with respect to the E-region critical frequency in place of the F-region. The E-region density profile usually contains no well-defined peak, making it difficult to decide the location and magnitude of normalization. Accordingly, the average of the values of  $\log_{10} P_s(h)$  between 125 and 135 km is employed as the value of power corresponding to E-region maximum density  $N_{\max}^E$ .

The  $N_e$  profile results must, in the case of Mode I, be corrected for the influence of the clutter subtraction scheme. This is because an appreciable fraction of the echo power lies at the center frequency and, hence, in the notch of the filter function  $H(f)$  [Eq. (13)]. Stated otherwise, at low altitudes the echo amplitude becomes correlated over intervals as long as 10 msec owing to the very high collision frequency. That is, the echo power  $P_I$  remaining after clutter subtraction becomes

$$P_I = P_s [1 - \rho(\tau_c)] \quad (40)$$

where  $\rho(\tau_c)$  is the correlation over the interval (10 msec) at which the clutter subtraction is carried out. D. T. Farley (private communication) has pointed out that the expression for the autocorrelation function in the collision-dominated case, based on taking the Fourier transform of the spectrum equation of Dougherty and Farley (Ref. 18 - see Sec. C below), becomes

$$P(\tau) = e^{-\tau/\tau_n} \quad (41)$$

$$\tau_n = \tau(2\pi\Delta f_i/\lambda) \quad (42)$$

$$\Psi = \nu_{in} / (2\pi \Delta f_i / \lambda) \quad (43)$$

Adopting  $\lambda = 0.68$  m,  $m_i = 31$  amu, yields

$$\rho(\tau_c) = \exp[-1820 T_i / \nu_{in}] \quad (44)$$

In order to use this result, we have computed the function

$$K(h) = 1 - \rho(\tau_c)_h \quad (45)$$

for model atmospheric conditions. Adopting  $T_i(h)$  and  $[N_2](h)$  from the CIRA 1965 (Ref. 19) and U.S. Standard Atmosphere 1962 (Ref. 20) models and the simple expression of Wand and Perkins,<sup>21</sup> based on the work of Banks,<sup>22</sup> relating  $\nu_{in}$  and  $[N_2]$

$$\nu_{in} = 0.9 \times 10^{-15} [N_2] \quad \text{sec}^{-1} \quad (46)$$

one computes  $K(h)$  as listed in Table XII and plotted in Fig. 10. The definition of  $\nu_{in}$  employed by Banks differs from that of Dougherty and Farley by a factor of 2 so that the value of  $\nu_{in}$  to be employed in Eq. (44) is half that given by Eq. (46).

TABLE XII COMPUTATION OF THE EFFECT OF CLUTTER SUBTRACTION ON THE MODE I ELECTRON DENSITY PROFILE					
Height (km)	Temperature (K)	$N(N_2)$ ( $m^{-3}$ )	$\nu_{in}$ ( $\text{sec}^{-1}$ )	$K(h)$	Source
120	381	$4.01 \times 10^{17}$	$1.80 \times 10^2$	1.0	Ref.19
110	263	$1.62 \times 10^{18}$	$7.23 \times 10^2$	1.0	Ref.19
100	213	$8.18 \times 10^{18}$	$3.68 \times 10^3$	1.0	Ref.19
90	186	$4.96 \times 10^{19}$	$2.23 \times 10^4$	1.0	Ref.19
80	186	$2.96 \times 10^{20}$	$1.33 \times 10^5$	0.92	Ref.19
70	219	$1.41 \times 10^{21}$	$6.35 \times 10^5$	0.47	Ref.20
60	243	$4.95 \times 10^{21}$	$2.22 \times 10^6$	0.18	Ref.20

The final electron density profile is therefore obtained from the expression

$$\begin{aligned} \log_{10} N_e(h) = & \log_{10} [P_s(h)] - \log_{10} [\bar{P}_s(h)] \\ & + \log_{10} N_{\max}^E - \log_{10} [K(h)] \end{aligned} \quad (47)$$

where  $\bar{P}_s(h)$  is the aforementioned average value over the interval  $125 \leq h \leq 135$  km.

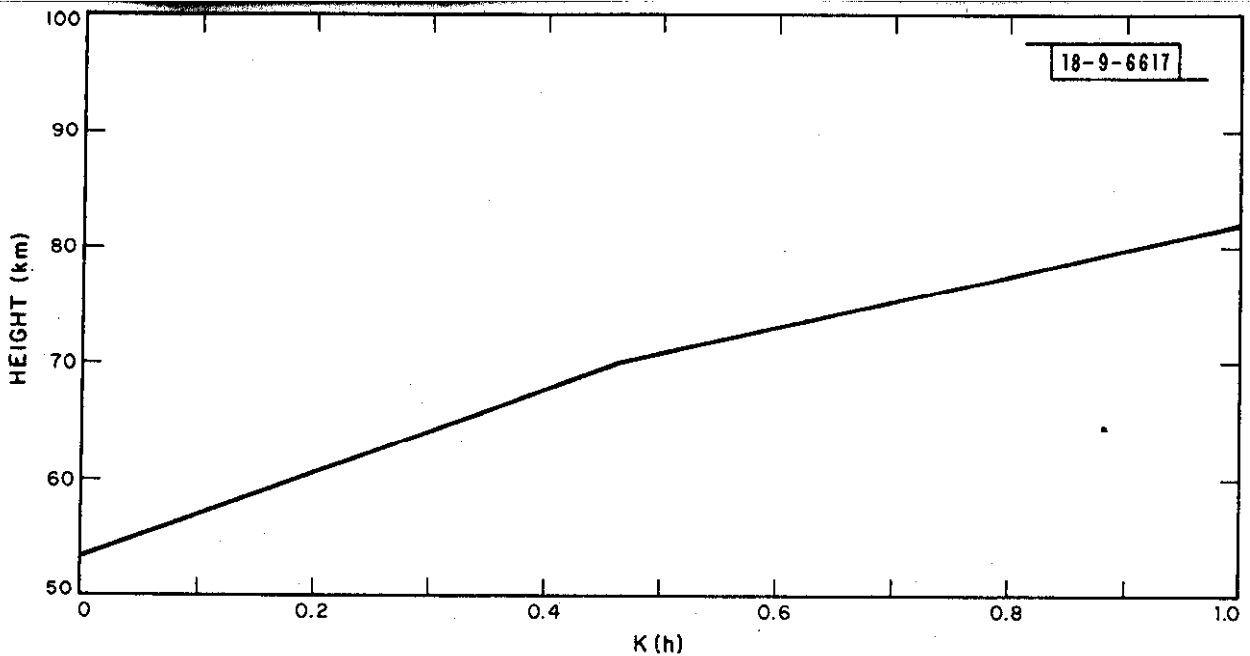


Fig. 10. Altitude variation of fraction of echo power remaining after clutter subtraction operation has been conducted in computer.

As discussed in Ref. 14, the results obtained using the Mode I program are open to serious doubt at altitudes below about 75 to 80 km and may be in error even higher. The cause of the difficulty appears to be the presence of an additional scattering mechanism, as yet unidentified, which may be clutter returns from aircraft. The additional power observed at these low altitudes causes the  $N_e$  profile to depart progressively from the expected curve below about 80 km, as illustrated in Fig. 9(b). Thus, in the I Mode profile plotting program the plot is halted at the first altitude below 80 km at which the density appears to be increasing as the altitude is decreased. In practice, this is usually close to 80 km so that the correction applied to the results for the effect of the filter [Eq. (47)] is rarely larger than a factor of 2.

## C. CORRELATION-FUNCTION ANALYSIS

### 1. General

Each measured acf is analyzed independently of all other data. The analysis program first calculates the real part or magnitude and phase of an acf as described in Secs. IV-C-3 and -4 [Eqs. (25) through (27)].  $M(\tau)$  is not corrected at this point in the analysis program for instrumental effects (as was done to obtain a real-time printout of the data -- see Sec. IV-C), but is analyzed directly in its uncorrected form. The statistical uncertainties in these real parts, magnitudes, and phases are calculated for purposes of weighting and subsequent temperature error calculations (Appendix B).

### 2. Phase Analysis

The phase  $\phi$  of an acf is analyzed as in Sec. IV-C-4 [Eqs. (28) and (29)] to determine a velocity, using now the true estimate of  $\sigma_\phi$  instead of the approximation  $\sigma_\phi = 1/M$  for weighting, i.e., replacing  $M$  by  $1/\sigma_\phi$  in Eq. (29). Lags are eliminated from this fitting procedure if the data variance estimate is negative (statistical fluctuation due to near-zero signal-to-noise) or the phase estimate is greater than half a radian (unreasonable velocity). The velocity estimates are systematically in error due to failure to account for the asymmetry of the receiver spectrum, i.e., failure to calculate the imaginary part of the noise acf. The effect of this neglect

is examined in Appendix A, where the velocity bias due to transmitter frequency chirp is also discussed. Figures 9(d) and (e) show examples of velocity determinations.

### 3. Magnitude Analysis - Library Search

The magnitude  $M$  (set equal to the real part in Mode F and for  $\tau \geq 200$   $\mu$ sec in Mode G as the imaginary part of the acf is not measured) is analyzed through comparison with a library of theoretical acf magnitudes. The library is 3-dimensional (two independent variables); it has been felt that additional independent parameters could not be reliably deduced from the data. A  $(T_i, \nu_{in})$  library is used at lower altitudes, a  $(T_i, T_e/T_i)$  library at higher altitudes. The general method used for performing the 2-parameter library regression and the estimation of errors by this technique is presented in Appendix B.

A coarse-grid library search is followed by a fine-grid search centered about the minimum point in the coarse grid. The coarse search covers the entire grid space to find the proper area for closer scrutiny by the fine search. The grid limits and step sizes for each search are tailored to the expected values and ranges of variation of the physical parameters under investigation. Table XIII gives the  $T_i$  grid limits, step sizes, and number of grid points used for the coarse and fine searches. The  $T_e/T_i$  grid values are given in Table XIV. The  $\nu_{in}$  grid values are stored in terms of normalized collision frequency  $\psi$  as defined in Eq. (43). The  $\psi$  grid values also are given in Table XIV.

At each grid point  $[(T_i, T_e/T_i)$  or  $(T_i, \nu_{in})]$  a theoretical acf magnitude is stored. These functions are direct calculations from the equations given by Farley<sup>23</sup> and by Dougherty and Farley<sup>18</sup> for a monoionic plasma without the presence of a magnetic field for the limiting cases of small Debye length and electron-to-ion-mass ratio. This zero-Debye-length assumption causes  $T_e$  to be systematically underestimated. Moorcroft<sup>24</sup> has developed a simple method for correction of this error after analysis of the acf (see Sec. E below). The zero-electron-mass assumption causes a very slight systematic error in all determined parameters. The greatest error occurs in  $T_e/T_i$  determination (-2 percent for  $O^+$  plasma, -1.4 percent for  $O_2^+$  plasma); other errors are not more than 1 percent. This zero-electron-mass assumption was made in order that one library formulation would suffice for all ion species.

These theoretical acf's are stored as a function of normalized correlation delay  $\tau_n$  as defined in Eq. (42). The library stores 187 points per acf for each  $T_e/T_i$  grid point, 240 per acf for each  $\psi$  grid point;  $\tau_n$  in each case starts at zero and increases in steps of 0.05. The lengths of these functions are sufficient for reasonable ionospheric values; the functions are assumed to be zero if greater lags are needed. The library acf's are calibrated in lag simply by dividing  $\tau_n$  by the coefficient of  $\tau$  in Eq. (42). To obtain the lags needed for direct comparison with the data, parabolic interpolation in lag is used.

To account for the instrumental smearing of the data, each library acf, before comparison with the data, is mathematically smeared by the computer in the same manner in which the data were smeared by the equipment (Appendix A).

For each comparison between a measured and a theoretical acf, the data are multiplicatively normalized such that the comparison yields closest fit in a weighted, least-squares sense. This type of normalization is addressed in Appendix B.

Figures 9(c) through (e) show examples of theoretical acf magnitudes fitted to measured data.

TABLE XIII  
T<sub>i</sub> GRID LIMITS (K)

Mode	Altitude* (km)	Fine Grid† (13 grid points)			Coarse Grid (8 grid points)	
		Step Size	Lower Limit	Upper Limit	Lower Limit	Upper Limit
F	106	12	78	522	150	450
	109	12	78	522	150	450
	112	12	128	572	200	500
	115	12	128	572	200	500
	118	12	128	572	200	500
	121	18	92	758	200	650
	124	18	92	758	200	650
	130	18	192	858	300	750
	136	18	192	858	300	750
	142	18	142	808	250	700
	148	18	192	858	300	750
	154	18	242	908	350	800
	160	18	292	958	400	850
166	18	342	1008	450	900	
G	167	18	342	1008	450	900
	182	18	392	1058	500	950
	197	18	492	1158	600	1050
	212	18	492	1158	600	1050
	227	30	420	1530	600	1350
	242	30	420	1530	600	1350
	257	30	420	1530	600	1350
	272	30	420	1530	600	1350
	287	30	420	1530	600	1350
	302	36	384	1716	600	1500
317	36	384	1716	600	1500	
H	215	36	384	1716	600	1500
	245	36	384	1716	600	1500
	275	36	384	1716	600	1500
	305	36	384	1716	600	1500
	335	36	384	1716	600	1500
	365	36	384	1716	600	1500
	395	36	384	1716	600	1500
	425	36	384	1716	600	1500
	455	36	384	1716	600	1500
	485	36	384	1716	600	1500
515	36	384	1716	600	1500	

\* See Table III regarding altitude variations.

† Fine-grid search uses 13 grid points centered on coarse-grid-search optimum fit (but not allowed to extend beyond grid limits).

TABLE XIV									
$T_e/T_i$ AND NORMALIZED COLLISION FREQUENCY $\psi$ GRID POINTS									
$T_e/T_i$									
<u>0.62</u>	0.75	0.87	<u>1.00</u>	1.12	1.25	1.37	1.50	1.62	<u>1.75</u>
1.87	2.00	<u>2.12</u>	2.25	2.37	<u>2.50</u>	2.62	2.75		
<u>2.87</u>	3.00	3.12	<u>3.25</u>	3.37	3.50				
$\psi$									
<u>0.00</u>	0.05	0.10	<u>0.15</u>	0.20	0.25	<u>0.30</u>	0.35	0.40	
0.45	0.50	0.55	<u>0.60</u>	0.65	0.70	<u>0.80</u>	1.00	1.20	
<u>1.40</u>	1.60	1.80	<u>2.20</u>	3.00					
<p>Notes: Coarse-grid-search points are underlined.</p> <p>Fine-grid search uses nine consecutive grid points centered about coarse-grid-search optimum fit (but not allowed to extend beyond grid limits).</p>									

Different altitude ranges are analyzed in different manners according to the physical parameters expected to be influential in different regions. Following a discussion of ion-composition problems in incoherent scatter data analysis, these altitude regions are discussed in detail. Table XV is a summary of the analysis process in different regions to be referred to in the next few sections.

#### 4. Ion-Composition Problem

The major ions likely to be encountered in the altitude range of these 2-pulse experiments are  $O^+$ ,  $NO^+$ ,  $O_2^+$ ,  $H^+$ , and occasionally sporadic-E metallic ions. As plasma-wave description depends upon  $T_i$  and  $m_i$  only as a ratio, ion identification is not possible from a given incoherent scatter acf (e.g.,  $O_2^+$  at 1000 K and  $O^+$  at 500 K would be indistinguishable). Such identification could be a problem in certain circumstances, e.g., near 200 km where we have mostly  $O^+$  by day and  $NO^+$  and  $O_2^+$  by night, or in a sporadic-E layer in which the ambient ions are well-outnumbered by the metallic ions. However, in general, one knows the identities of the major species expected, and the major task is the determination of the relative composition if a mixture is present.

When the plasma contains two ion species of very different mass (e.g.,  $O^+$ ,  $H^+$ ), contributions from each species can be easily seen in the incoherent scatter spectrum.<sup>24</sup> If the mass ratio is a factor of 2 or less (e.g.,  $O^+ - O_2^+ - NO^+$  or  $F_e^+ - O_2^+ - NO^+$ ), however, the spectrum so closely approximates the monoionic shape that essentially error-free data are required for composition determination from a given measured spectrum (or acf).<sup>25</sup> This quality is not approached with Millstone Hill data. In previous papers,<sup>11,12</sup> we have shown how analysis of an entire profile of data simultaneously can be used to deduce this composition. Application of this profile type of analysis to the 2-pulse data is discussed in Sec. D below.

TABLE XV  
SUMMARY OF ASSUMED AND MEASURED PARAMETERS  
IN THE DATA ANALYSIS

Height Range (km)	Assume	Measure
106 to 118	$T_e = T_i = T_n$ $p = 0$	$T_i, \nu_{in}$
118 to 130*	$T_e = T_i = T_n$ $p = 0$ $\nu_{in} = 0$	$T_i$
130 to 166 <sup>†</sup>	$T_i = T_n$ from Eq.(48) $\nu_{in} = 0$	$T_e, p$
166 <sup>†</sup> to 225	$T_i = T_n$ from Eq.(48) $\nu_{in} = 0$	$T_e, p, V_d$
225 to 515	$p = 1$ $\nu_{in} = 0$	$T_e, T_i, V_d$
92 to $\leq 700$	-	$N_e$

\* See text for discussion of special analyses at these altitudes.  
<sup>†</sup> This altitude break corresponds to the change from F to G Mode; the actual height was a little higher for some early data (see Table III).

At the lowest altitudes covered by the 2-pulse experiments,  $O_2^+$  and  $NO^+$  ions predominate in the daytime, except occasionally in sporadic-E layers. These molecular masses are so similar (30 and 32 amu) that they cannot be distinguished. As the  $NO^+ - O_2^+$  composition is variable and unknown a priori, the temperatures determined from data in this region are always uncertain within a  $\pm 3$ -percent range if one assumes a mean mass of 31 amu.  $NO^+$ , however, is generally the more abundant of these species, but assumption of a mean mass of 30.5 may lead to errors of  $+2/-5$  percent, i.e., possibly a larger systematic error.

Above 130 km, a sufficient proportion of  $O^+$  ions may appear to cause further uncertainty. This transition from  $NO^+$  and  $O_2^+$  to  $O^+$  ions has been studied by Oliver<sup>26</sup> from available ion mass spectrometer data from rocket experiments. This summary shows that the altitude range of this transition region is variable, but that in its extreme cases of midlatitude measurements the range extends from 130 km (winter day) to 260 km (summer night) - a sufficient number of minor ions may exist at certain times within this range to cause a 3- to 100-percent error in temperature determination from incoherent scatter data. It is possible that extremely unusual conditions (e.g., trough passage over Millstone) may cause molecular ions to be more important at even higher altitudes.

The question of ion composition below 200 km at night is moot, as the electron density is too low for useful acf measurement. At night, the region of transition from molecular to atomic ions takes place in a narrow region on the sharp underside of the F2-layer. Both the rate of ambipolar diffusion and the lifetime of  $O^+$  decrease exponentially as an ion descends from the F2 peak, creating a very sharp  $O^+$  gradient. The ion-composition transition is, in fact, so sharp that a wide range of composition mixtures may well exist in the volume responsible for the lowest altitude of usable returns; this occurrence could cause significant distortion of the spectrum (giving very low  $T_e/T_i$  ratios in analysis, assuming a fixed composition), but this problem has not been addressed for these data.

$H^+$  does not seem to cause significant effects in the acf's during the day, but may comprise a sizable portion ( $> 10$  percent) of the ion content near 500 km at night. Its neglect may cause serious nighttime temperature overestimates.

#### 5. Collisional Region - $h < 118$ km

In the lower E-region, the shape of the incoherent scatter spectrum is significantly affected by the influence of ion-neutral collisions.<sup>9</sup> At the Millstone Hill radar wavelength these effects are consistently seen below 118 km and may be significant as high as 130 km, though the smallness of the effects here precludes consistent, reliable determinations. Above 130 km, collisional effects are undetectable. In addition, in the region below 130 km there is no evidence from Millstone Hill data that  $T_e$  is significantly higher than  $T_i$ . Analysis for  $h < 118$  km therefore assumes  $T_i = T_e$ , and seeks to determine  $T_i$  and  $\nu_{in}$ . An ion mass of 30.5 amu is assumed.

Figure 11 shows an example of  $T_i$  and  $\nu_{in}$  values determined from measured data.

#### 6. Temperature Equality Region - $118 < h < 130$ km

As was mentioned in the previous section, no consistent, reliable  $\nu_{in}$  information is obtained in the 118- to 130-km region; also, there is no evidence from Millstone Hill data<sup>9</sup> or theory<sup>27</sup> that there is a significant  $T_e - T_i$  difference below 130 km. This altitude range is analyzed to find  $T_i$  with  $T_e = T_i$  and  $\nu_{in} = 0$ , assuming an ion mass of 30.5 amu.



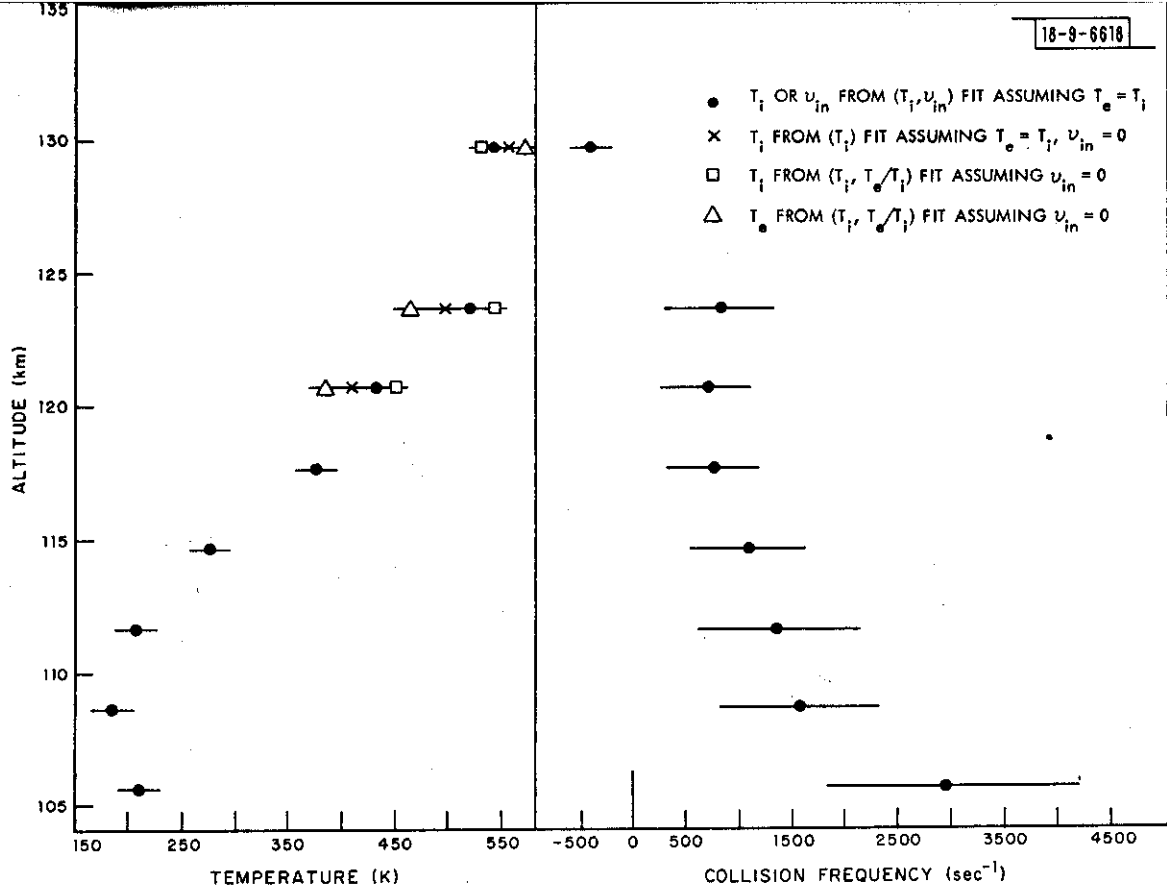


Fig. 11. Lower F Mode results on 18 September 1974, 1735-1747 UT.

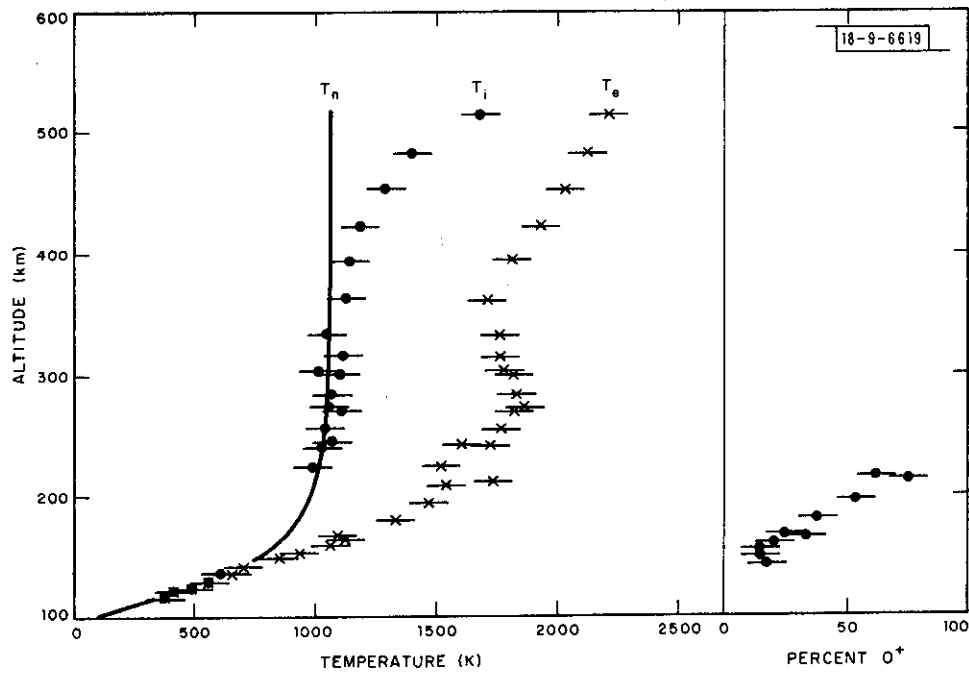


Fig. 12. Profile analysis for data on 18 September 1974, 1731-1800 UT. Thermosphere results yield:  $T_{\infty} = 1052 \pm 17$  K;  $s = 0.0262 \pm 0.0041$  km<sup>-1</sup>;  $T_{120} = 408 \pm 13$  K; and  $[O]_{400} = (2.46 \pm 0.99) \times 10^8$  cm<sup>-3</sup>.

Some additional calculations have been made for this region to test the adequacy of the assumptions  $T_e = T_i$  and  $\nu_{in} = 0$ , i.e., a  $(T_i, \nu_{in})$  and a  $(T_i, T_e/T_i)$  search has also been performed on data in this region.

Figure 11 shows results from these various analyses performed on measured data.

#### 7. Ion-Composition Transition Region - $130 < h < 225$ km

$T_e$  and  $T_i$  differ in this region, and a  $(T_i, T_e/T_i)$  library search is thus performed. In this region, the ion content may consist of significant amounts of both molecular- and atomic-ion species and, as their proportions cannot be reliably obtained from analysis of a measured acf (Sec. 4 above), all acf's in this altitude range are analyzed under the assumption of a pure  $O^+$  ionosphere. The temperature values so obtained are systematically too low, but can be corrected when an estimate of the ion-composition profile is obtained. Section D-2 below explains how this estimate is derived and how corrections to  $T_e$  and  $T_i$  are then applied.

#### 8. $O^+$ Region - $225$ km $< h$

Only  $O^+$  ions are assumed to be important in this region, and a  $(T_i, T_e/T_i)$  library search is performed. Because significant amounts of molecular ions may on occasion exist up to 250 km during the day and possibly beyond 260 km at night, there is the possibility of underestimating  $T_i$  and  $T_e/T_i$  in these height intervals. The  $H^+$  abundance is also assumed to be negligible. This is not always true at night and can cause the temperature to be overestimated above 400 km, the error increasing with altitude.

Figure 12 includes some sample results from this height region from an analysis of measured data.

### D. NEUTRAL-ATMOSPHERE DEDUCTIONS AND ION-COMPOSITION PROFILE

#### 1. General

Although the incoherent scatter technique measures ionospheric properties, a number of deductions can be made concerning the neutral atmosphere. In some cases, ionic and neutral properties are equal.  $\nu_{in}$ , which is measurable below 130 km, is essentially proportional to  $[N_2]$ , as  $N_2$  is the predominant constituent in this region. Also,  $T_i$  and  $T_n$  are thought to be equal below 200 km and can reliably be assumed equal whenever  $T_e$  is found to be equal to  $T_i$ .

Other deductions concerning the neutral atmosphere can be made by considering an entire profile of data and invoking appropriate profile-continuity constraints. (Further information may be obtainable by invoking additional time-continuity constraints, but this has not been done with these data.) In this way, information has been obtained on the  $[O]$  and  $T_n$  profiles. This  $T_n$  profile estimate can then be used to estimate the ion composition in the F1-region.

#### 2. $T_n$ , $[O]$ Profile

Bauer *et al.*<sup>28</sup> have shown how one may determine  $T_n$  from incoherent scatter data in regions where the ion composition is known and  $T_e > T_i > T_n$  through use of the ion heat-balance equation. Their analysis assumes  $T_n$  to follow the Bates<sup>29</sup> profile shape above  $h = 120$  km

$$T_n(h) = T_\infty - (T_\infty - T_{120}) \exp[-s(h - 120)]$$

and [O] to be in diffusive equilibrium above 225 km. The abundance of O at some reference altitude (usually specified 400 km) and  $T_n(h)$  then define [O] (h). In the original analysis scheme of Bauer *et al.*, the parameters  $T_\infty$ ,  $s$ , and  $[O]_{400}$  were determined from the data, assuming a model value for  $T_{120}$  and using a two-step procedure. First,  $T_\infty$  and  $[O]_{400}$  were determined from the data above 300 km altitude with  $s = 0.024 \text{ km}^{-1}$ . Then, retaining the just-determined  $[O]_{400}$  value,  $T_\infty$  and  $s$  were determined from the data above 225 km.

For analysis of Millstone Hill 2-pulse data, a variation of the above analysis is used. Data from 116 to 135 km are used and help to establish  $T_{120}$ . In some cases, this lower-altitude range has been set at 120 to 130 km. A second difference is that all four unknowns are solved for simultaneously. While this requires only a one-step procedure, additional calculations are made with certain parameters held fixed if the uncertainty of an initial result is too great or more than 20 nonlinear least-squares iterations are needed in the fitting procedure (nonconvergence). If  $[O]_{400}$  has more than 75-percent uncertainty, it is fixed using the Jacchia 1971 model<sup>30</sup> and the remaining free parameters are sought. If no E-region data are available for the fit (e.g., at night), both  $T_{120}$  and  $[O]_{400}$  are initially set to their Jacchia model values before solving to find  $T_\infty$  and  $s$ ; then, automatically, the data are refitted with  $s$  additionally held fixed at  $0.02 \text{ km}^{-1}$  to find only  $T_\infty$ . Only the results of the last fit made are preserved on magnetic tape, although all fitting results are output onto the line printer.

The need for multiple fitting contingencies for profile analysis raises questions concerning the reliability of the results. The fitting procedure is indeed often unsuccessful in determining consistent and reasonable values of anything but  $T_\infty$  and  $T_{120}$ . The  $[O]_{400}$  and  $s$  parameters are not thought to yield consistently useful results when determined simultaneously, although tests have produced good  $[O]_{400}$  results when  $s$  is fixed in the analysis.

Figure 12 is an example of this profile fitting procedure, showing the deduced  $T_n$  profile.

### 3. Ion-Composition Profile

The  $T_n(h)$  estimate discussed in the previous section is derived from E- and F2-region data as the unknown ion composition of the F1-region prevents unambiguous temperature measurement in that region. For analysis of Millstone Hill 2-pulse data, this  $T_n$  profile estimate [Eq. (48)] is assumed to be valid through the F1-region also. As the ion and neutral temperatures are equal in this region,<sup>27</sup> the F1-region ion-temperature-composition ambiguity can be solved. This approach has been used in some previous Millstone Hill investigations.<sup>11,12</sup> Because the ambiguity is so nearly complete, it is possible to derive simple mapping relations for the correspondence of relative ion and electron temperatures to relative ion composition.<sup>31</sup> These relations are given in Table XVI. Shown here is A(p), the ratio of ion temperature one would deduce assuming an arbitrary ion composition  $p = [O^+]/N_e$  to the ion temperature one would deduce assuming  $p = 1$ . A similar relation B(p) is shown for the  $T_e/T_i$  determination. Linear interpolation between these tabulated points is used in 2-pulse data analysis. The exact value of A(0) is somewhat uncertain due to the slight (perhaps 5 percent) uncertainty in E-region mean molecular-ion mass ( $O_2^+/NO^+$ ) ratio (see Sec. C-4 above). Moreover, there is, in fact, a family of such relations for A and B for differing values of  $T_e/T_i$ , but each one is tightly packed such that little accuracy is lost by choosing a central member of each family. This has been done to obtain Table XVI.

The 2-pulse data in the 130- to 225-km region are initially analyzed under the assumption of  $p = 1$ , yielding profiles of  $T_i(p = 1)$  and  $T_e/T_i(p = 1)$ . Once the independent  $T_i$  estimate

TABLE XVI		
VALUES OF A(p) AND B(p) RELATING RELATIVE F1-REGION ION COMPOSITION AND RELATIVE ION AND ELECTRON TEMPERATURES		
p	A(p)	B(p)
0.0	1.937	1.000
0.1	1.744	1.065
0.2	1.570	1.123
0.3	1.427	1.165
0.4	1.308	1.188
0.5	1.218	1.192
0.6	1.146	1.177
0.7	1.092	1.146
0.8	1.052	1.106
0.9	1.021	1.056
1.0	1.000	1.000

$T_i$ (model) has been formed in this region (see previous section), one finds the ion composition simply by finding the value of  $p$  in Table XVI corresponding to  $A(p) = T_i(\text{model})/T_i(p = 1)$ . The statistical error in  $p$  is similarly found by mapping the  $T_i(\text{model})/[T_i(p = 1) \pm \Delta T_i(p = 1)]$  confidence interval onto the  $p$ -axis ( $\Delta$  here denotes  $T_i$  uncertainty). In addition to the statistical errors in  $p$ , there may be large systematic errors due to the assumptions necessary in deriving the independent model  $T_i$  estimate. Once  $p$  is found, one finds the final estimate of  $T_e/T_i$  by mapping from the  $p$ - to the  $B$ -axis to find  $B(p)$ , then estimating  $T_e/T_i = B(p)(T_e/T_i)(p = 1)$ .

On occasion, this composition estimation procedure yields composition values outside of the physical range (0 – 100-percent  $O^+$ ). In such cases, the 0 or 100-percent limit is assumed and the temperatures corresponding to this composition limit are adopted.

Due to the possibility of large systematic uncertainties in the independent  $T_i$  estimate in the F1-region, the other F1-region results (composition,  $T_e$ ) are also subject to sizable systematic errors, with the exception perhaps of  $T_e/T_i$  which is less than 20-percent uncertain even in the worst-case situation. To date, these F1-region results have not been extensively used.

Figure 12 shows an example of the  $T_e$  and composition values deduced from measured data.

#### 4. Electron-Density-Profile Corrections

As explained in Sec. B-1 above,  $(T_e/T_i)(h)$  is needed before  $N_e(h)$  can be calculated from  $P_s(h)$ . The final estimate of  $(T_e/T_i)(h)$  in the region of unknown ion composition (130 to 225 km) cannot be made until the ion-composition profile is determined (Sec. 3 above), and thus  $N_e(h)$  evaluation in this region must also await ion-composition determination. Once this final estimate of  $(T_e/T_i)(h)$  is made, the final estimate of  $N_e(h)$  is made via the method explained in Sec. B-1 above. A large uncertainty in ion composition is not so detrimental to  $(T_e/T_i)(h)$  (see Sec. 3 above), and thus to  $N_e(h)$  determination. A maximum of 10- to 20-percent error in  $N_e(h)$  may result if ion composition is grossly in error.

#### E. DEBYE-LENGTH CORRECTIONS

All acf analysis employs a library of theoretical acf's calculated for the limiting case of small Debye length (Sec. C-3 above). This assumption is never quite true, but only affects the results appreciably when  $N_e$  is very low, in which case the  $T_e$  estimate is low and the  $N_e$  estimate is also low due to the  $T_e/T_i$  correction employed in its calculation from  $P_s$  (Sec. B-1 above). Moorcroft<sup>24</sup> has shown how one can correct these  $T_e$  and  $N_e$  values in a simple but iterative manner, but this correction has not been applied to the Millstone Hill 2-pulse data.

#### ACKNOWLEDGMENTS

In addition to the authors of this report, several people have been instrumental in the development of the "two-pulse" program at Millstone Hill. Wallace A. Reid has been the engineer in charge of development, modification, and maintenance of the radar equipment. Leonard B. Hanson has been the engineer in charge of the development, modification, and maintenance of the radar-computer interface and maintenance of the computer. Glenn W. Armistead was responsible for much of the real-time computer program development. Richard A. Brockelman, Tor Hagfors, Robert A. Power, John K. Upham, Arnold D. Kaminsky, Alice R. Freeman, John M. Holt, Ralph F. Julian, and Gary A. Bullock provided programming and data analysis support.

## REFERENCES

1. J. V. Evans, R. F. Julian, and W. A. Reid, "Incoherent Scatter Measurements of F-Region Density, Temperatures, and Vertical Velocity at Millstone Hill," Technical Report 477, Lincoln Laboratory, M.I.T. (6 February 1970), DDC AD-706863.
2. J. V. Evans and M. Loewenthal, *Planet. Space Sci.* 12, 915 (1964).
3. J. V. Evans, *Planet. Space Sci.* 13, 1031 (1965), DDC AD-616607.
4. \_\_\_\_\_, *J. Geophys. Res.* 70, 1175 (1965), DDC AD-614310.
5. \_\_\_\_\_, *Planet. Space Sci.* 15, 1387 (1967).
6. \_\_\_\_\_, *Planet. Space Sci.* 18, 1225 (1970), DDC AD-716056.
7. \_\_\_\_\_, *Planet. Space Sci.* 21, 763 (1973), DDC AD-772137/6.
8. \_\_\_\_\_, *Planet. Space Sci.* 23, 1461 (1975), DDC AD-A024177/8.
9. \_\_\_\_\_, *Proc. IEEE* 57, 496 (1969), DDC AD-694192.
10. \_\_\_\_\_, *J. Geophys. Res.* 72, 3343 (1967), DDC AD-658912.
11. J. V. Evans and L. P. Cox, *J. Geophys. Res.* 75, 159 (1970), DDC AD-703492.
12. L. P. Cox and J. V. Evans, *J. Geophys. Res.* 75, 6271 (1970), DDC AD-722911.
13. J. V. Evans, *J. Geophys. Res.* 77, 2341 (1972), DDC AD-752948.
14. G. W. Armistead, J. V. Evans, and W. A. Reid, *Radio Sci.* 7, 153 (1972), DDC AD-742616.
15. J. V. Evans, Editor, "The Millstone Hill Propagation Study: Progress in FY 1970," Technical Note 1970-20, Lincoln Laboratory, M.I.T. (2 December 1970), DDC AD-717156.
16. J. V. Evans, R. A. Brockelman, R. F. Julian, W. A. Reid, and L. A. Carpenter, *Radio Sci.* 5, 27 (1970), DDC AD-704631.
17. J. V. Evans, "Millstone Hill Thomson Scatter Results for 1967," Technical Report 482, Lincoln Laboratory, M.I.T. (22 July 1971), DDC AD-735727.
18. J. P. Dougherty and D. T. Farley, *J. Geophys. Res.* 68, 5473 (1963).
19. COSPAR International Reference Atmosphere (North-Holland, Amsterdam, 1965).
20. U.S. Standard Atmosphere (U.S. Government Printing Office, Washington, D.C., 1962).
21. R. H. Wand and F. W. Perkins, *J. Geophys. Res.* 73, 6370 (1968).
22. P. M. Banks, *Planet. Space Sci.* 14, 1105 (1966).
23. D. T. Farley, *J. Geophys. Res.* 71, 4091 (1966).
24. D. R. Moorcroft, *J. Geophys. Res.* 69, 955 (1964).
25. H. Carru, R. Benoit, and M. Petit, *LaNature*, No. 3330, 422 (1962).
26. W. L. Oliver, *J. Atmos. Terr. Phys.* 37, 1065 (1975).
27. P. M. Banks, *Proc. IEEE* 57, 258 (1969).
28. P. Bauer, P. Waldteufel, and D. Alcayde, *J. Geophys. Res.* 75, 4825 (1970).
29. D. R. Bates, *Proc. Roy. Soc. (London)* A253, 451 (1959).
30. L. G. Jacchia, "Revised Static Models of the Thermosphere and Exosphere with Empirical Temperature Profiles," Smithsonian Astrophysical Observatory Special Report 332 (1971).
31. P. Waldteufel, *J. Geophys. Res.* 76, 6995 (1971).

APPENDIX A  
SYSTEMATIC DISTORTIONS IN CORRELATION-FUNCTION MEASUREMENTS

The techniques employed at Millstone Hill to measure the ionospheric correlation function cause a number of systematic distortions to appear in the measurements. These distortions may be grouped into two categories. First, there are those distortions intrinsic to any monostatic, incoherent scatter experiment – namely, those due to use of a finite-width receiver passband and transmitter gating. Second, we have those distortions introduced by inaccuracies, improper calibrations, and errors introduced by the hardware. Allowance for these distortions is of great importance in the analysis of the measurements. Such analysis consists in comparison between undistorted theoretical correlation functions and the distorted measurements. Calculation of the distortion is thus required before comparison is possible. Definition and evaluation of these distortions are the objects of this appendix.

I. FINITE-WIDTH RECEIVER PASSBAND AND TRANSMITTER GATING

The effects of finite-width receiver bandpass and transmitter gating upon ionospheric incoherent scatter correlation-function measurements have been considered for the general incoherent scatter experiment by D.T. Farley.<sup>†</sup> His basic result is that the ionospheric autocorrelation function is first multiplied by the autocorrelation function of the transmitter waveform, and the spectrum of the resulting backscattered signal is then multiplied by the receiver bandpass spectrum. If we let  $\rho_m(\tau)$  be the autocorrelation function measured at correlation time delay  $\tau$ ,  $\rho(\tau)$  be the autocorrelation function of the ionospheric plasma density fluctuations,  $\rho_w(\tau)$  be the autocorrelation function of the gated transmitter waveform, and  $\rho_n(\tau)$  be the autocorrelation function of the impulse response of the receiver (or, equivalently, the autocorrelation function of white noise passed through the receiver), then Farley's result in the time domain can be written

$$\begin{aligned} \langle \rho_m(\tau) \rangle &\propto [\rho(\tau) \rho_w(\tau)] * \rho_n(\tau) \\ &= \int_{-\infty}^{\infty} \rho(\tau - x) \rho_w(\tau - x) \rho_n(x) dx \end{aligned} \quad (A-1)$$

where  $\langle \rangle$  denotes expected value, and  $*$  denotes convolution.  $\rho_w(\tau)$  and  $\rho_n(\tau)$  are known functions for a given experiment.

Analysis of measured functions  $\rho_m(\tau)$  at Millstone Hill uses a library of theoretical functions  $\rho_t(\tau)$  covering the range of functions over which  $\rho(\tau)$  may reasonably be expected to vary. To be able to compare the measurements  $\rho_m(\tau)$  with the theory  $\rho_t(\tau)$ , we must follow one of two approaches:

- (a) Correction approach – solve Eq. (A-1) for  $\rho(\tau)$  in terms of  $\rho_m(\tau)$ , and then compare  $\rho(\tau)$  and  $\rho_t(\tau)$  directly.
- (b) Convolution approach – apply the convolution effects of Eq. (A-1) to  $\rho_t(\tau)$  as

$$\rho_{tc}(\tau) \equiv [\rho_t(\tau) \rho_w(\tau)] * \rho_n(\tau) \quad (A-2)$$

<sup>†</sup>D.T. Farley, Radio Sci. 4, 935 (1969).



and then compare  $\rho_m(\tau)$  and  $\rho_{tc}(\tau)$  directly. Each method has been used for some facet of Millstone Hill 2-pulse data analysis; implementation of these methods is discussed below.

#### A. Correction Approach

In this approach, we attempt to solve Eq. (A-1) for  $\rho(\tau)$ . This problem was originally considered by T. Hagfors at Millstone Hill; a brief description of his approach is given here.

A necessary assumption to solve Eq. (A-1) for  $\rho(\tau)$  is that  $\langle \rho_m(\tau) \rangle$  is well approximated by  $\rho_m(\tau)$ . The next step is to expand  $\rho(\tau - x)$  of Eq. (A-1) as

$$\rho(\tau - x) = \rho(\tau) + \frac{d\rho(\tau)}{d\tau} (-x) + \frac{d^2\rho(\tau)}{d\tau^2} \frac{(-x)^2}{2} + \dots \quad (A-3)$$

in which case we may write Eq. (A-1) as

$$\begin{aligned} \rho_m(\tau) \approx & \rho(\tau) [\rho_w(\tau) * \rho_n(\tau)] + \frac{d(\tau)}{d\tau} \{ \rho_w(\tau) * [-\tau \rho_n(\tau)] \} \\ & + \frac{d^2\rho(\tau)}{d\tau^2} \left\{ \rho_w(\tau) * \left[ \frac{\tau^2}{2} \rho_n(\tau) \right] \right\} + \dots \end{aligned} \quad (A-4)$$

or

$$\begin{aligned} \rho_m(\tau) \approx & \rho(\tau) F_0(\tau) + \frac{d\rho(\tau)}{d\tau} F_1(\tau) + \frac{d^2\rho(\tau)}{d\tau^2} F_2(\tau) \\ F_k(\tau) = & \rho_w(\tau) * \left[ \frac{(-\tau)^k}{k!} \rho_n(\tau) \right] \quad k = 0, 1, 2 \end{aligned} \quad (A-5)$$

only three terms of the expansion being retained. Hagfors calculated  $F_0(\tau)$ ,  $F_1(\tau)$ , and  $F_2(\tau)$  analytically using an appropriate Gaussian waveform for  $\rho_n(\tau)$  and the actual transmitter waveforms used in the Millstone Hill experiments. An iterative procedure is then used to solve Eq. (A-5) for  $\rho(\tau)$ . The first-iteration estimate of  $\rho(\tau)$  is calculated ignoring the derivative terms of Eq. (A-5)

$$\rho_1(\tau) = \frac{\rho_m(\tau)}{F_0(\tau)}$$

The  $i^{\text{th}}$ -iteration estimate of  $\rho(\tau)$  is estimated as

$$\rho_i(\tau) = \frac{\rho_m(\tau)}{F_0(\tau)} - \frac{d\rho_{i-1}(\tau)}{d\tau} \frac{F_1(\tau)}{F_0(\tau)} - \frac{d^2\rho_{i-1}(\tau)}{d\tau^2} \frac{F_2(\tau)}{F_0(\tau)} \quad (A-6)$$

$\rho_i(\tau)$  is derived from measured data and is therefore noisy. As the calculation of derivatives from noisy data is undesirable, the derivatives required in Eq. (A-6) are replaced in practice by the derivatives of a parabola fit to five points in the neighborhood of  $\tau$ . Tests with noiseless functions  $\rho_{tc}(\tau)$  for  $\rho_m(\tau)$  show that  $i = 5$  iterations were required to yield an imperceptible difference between plots of  $\rho_i(\tau)$  and  $\rho_1(\tau)$ . A somewhat larger number of iterations is required for noisy data. The procedure does not break down upon addition of random noise to  $\rho(\tau)$ ; noise magnitudes of up to  $\rho(0)/5$  have been tested.

This correction approach to the finite-width receiver passband and transmitter gating distortions is used in Millstone Hill 2-pulse data analysis to obtain an initial look at the corrected data on the real-time computer printout; it is not applied to the real-time data stored on magnetic tape, nor is it used in the final data analysis since it is felt that the calculation of derivatives from noisy data necessitated by Eq. (A-6) is not sufficiently reliable, especially as the problem can be entirely avoided (albeit at the expense of computer time) by use of the convolution approach to the problem.

### B. Convolution Approach

In this approach, we perform the calculation of Eq. (A-2). Two methods have been used to perform this calculation. Discrepancies between the two methods are small.

The first of these methods calculates Eq. (A-2) directly through numerical integration using sampled functions, leaving the resulting correlation function normalized to unity at zero lag, i.e.,

$$\begin{aligned} \rho_{tc}(\tau) &= f_{\tau}(\tau)/f_0(0) \\ f_{\tau}(x) &= E_{\tau} [\rho_t(x) \rho_{w(\tau)}(x)] * \rho_n(x) \end{aligned} \quad (A-7)$$

where  $E_{\tau}$  represents the energy of the waveform  $w(\tau)$ , which, in general, may vary with  $\tau$ . These convolution calculations are intrinsically quite time consuming, and to speed up the calculation Eq. (A-7) has, in practice, been replaced by the simple approximation

$$\rho_{tc}(\tau) = \rho_t(\tau) \quad (A-8)$$

at lags such that  $\tau$  is greater than the sum of  $T$  (the width of the transmitted pulse) and  $\tau_n$  [the half-width of  $\rho_n(\tau)$ ]. Calculations have shown this approximation to be quite good. With  $\tau_n \approx 30 \mu\text{sec}$  and  $T = 40, 100, \text{ and } 200 \mu\text{sec}$  for Modes F, G, and H, respectively, we see that  $\tau > T + \tau_n$  allows most of the convolutions to be avoided in Modes F and G, for which  $0 \leq \tau \leq 380 \mu\text{sec}$ , but all must still be performed for Mode H, for which  $0 \leq \tau \leq 190 \mu\text{sec}$ . In practice, the convolutions were performed out through  $100 \mu\text{sec}$  for Mode F and  $150 \mu\text{sec}$  for Mode G. Approximation of Eq. (A-7) by Eq. (A-8) for these longer lags produced errors of about  $+1 \text{ K}$  in ion temperature  $T_i$  and  $+10 \text{ sec}^{-1}$  in collision frequency  $\nu_{in}$  for Mode F, and  $0 \text{ K}$  in  $T_i$  and  $+10 \text{ K}$  in electron temperature  $T_e$  for Mode G. These errors have been ignored in the data analysis.

The actual implementation of this convolution calculation contained a small error which, fortunately, did not greatly affect the final results. Equation (A-7) was erroneously calculated as

$$\rho_{tc}(\tau) = f_{\tau}(\tau)/f_{\tau}(0)$$

i.e., a different normalizing factor was applied for each lag. The errors resulting were about  $0 \text{ K}$  in  $T_i$  and  $+2 \text{ sec}^{-1}$  in  $\nu_{in}$  for Mode F,  $+6 \text{ K}$  in  $T_i$  and  $-5 \text{ K}$  in  $T_e$  for Mode G, and  $-10 \text{ K}$  in  $T_i$  and  $+5 \text{ K}$  in  $T_e$  for Mode H. These errors have also been ignored in the data analysis. The main effect of this error, however, was that a different normalization factor had to be calculated for each lag instead of the one normalization constant actually needed; this essentially doubled the number of convolution computations required.

In October 1976, a second method for performing the convolution of Eq. (A-2) was instituted to save computation time. This method uses the results of Hagfors' calculations as described in Sec. A above [Eqs. (A-3) through (A-5)] to write Eq. (A-2) as

$$\rho_{tc}(\tau) = \rho_t(\tau) F_0(\tau) + \frac{d\rho_t(\tau)}{d\tau} F_1(\tau) + \frac{d^2\rho_t(\tau)}{d\tau^2} F_2(\tau) \quad . \quad (A-9)$$

Whereas Hagfors originally calculated  $F_0(\tau)$ ,  $F_1(\tau)$ , and  $F_2(\tau)$  from analytical representations of  $\rho_n(\tau)$  and  $\rho_w(\tau)$ , the present approach has used sampled functions of actual measurements of  $\rho_n(\tau)$  and  $\rho_w(\tau)$  for this calculation. Hagfors' original use of Eq. (A-9) was in an attempt to deconvolve the measured data before comparison with theoretical ionospheric correlation functions; Eq. (A-9) is presently used to convolve the theoretical functions for direct comparison with the measured data. The only advantage that the present method has over Hagfors' original method is that the derivatives required by Eq. (A-9) are now calculated from smooth, theoretical functions instead of noisy, measured data. In general, comparison of the original, unmodified data with theoretical calculations is highly desirable.

The functions  $\rho_n(\tau)$  and  $F_0(\tau)$ ,  $F_1(\tau)$ , and  $F_2(\tau)$  of Eqs. (A-5) and (A-9) for the Millstone Hill 2-pulse experiments are tabulated in Table A-1. These functions are presently used for data analysis. The derivatives required by Eq. (A-9) are calculated as the derivatives of a parabola passed through three points in the neighborhood of  $\tau$ .

Adoption of Eq. (A-9) to approximate Eq. (A-2) has decreased the number of computations necessary from 6 additions and 14 multiplications, to 6 additions and 4 multiplications per lag - a large savings. Accuracy is better than 0.001 (relative to  $\rho_{tc}(0) = 1$ ).

## II. HARDWARE INACCURACIES

The development presented in Sec. I above for the effects of finite receiver bandwidth and transmitter gating upon the ionospheric correlation function is valid for any receiver and pulse scheme employed. Of course, there are always discrepancies between the hardware implementation and the proposed experimental design. These discrepancies for the 2-pulse experiments at Millstone Hill consist in hardware inaccuracies, miscalibrations, and errors, and have been found to be of significant importance in a number of instances. Those cases for which important measurement distortion results are discussed here.

### A. Receiver Inaccuracies

The receiver was designed to be symmetric about its center frequency and to have a fixed bandwidth of some 45 kHz. Receiver asymmetry was not evaluated until some six years of data had already been collected. It was then noticed that there was a small but important tilt in the receiver spectrum at the center of the spectrum. This tilt has the effect of applying a bias to all ionospheric drifts calculated from data passed through the receiver. This bias can be measured and allowed for in the data analysis, but the fear that receiver asymmetries had changed with time (evidence of receiver characteristics variation with time is presented in the next paragraph) has led us to consider these 2-pulse drift data to be of dubious worth.

In addition to the discovery of receiver asymmetries, discovery of bandwidth variation with time has also recently been made. Such a variation could be important in data interpretation, since the amount of instrumental smearing of the ionospheric spectrum (see Sec. I above) depends upon receiver bandwidth. The correlation function of the noise output from the receiver is measured during the 2-pulse experiments each time an altitude profile of ionospheric correlation functions is measured; an average of a large number of such measurements from the earlier days of 2-pulse data taking produced the adopted function  $\rho_n$  in Table A-1. More recent

TABLE A-1  
 $\rho_n$  AND THE FUNCTIONS  $F_0$ ,  $F_1$ , AND  $F_2$  FOR MODES F, G, AND H

Delay ( $\mu\text{sec}$ )	$\rho_n$	Mode F			Mode G			Mode H		
		$F_0$	$F_1$	$F_2$	$F_0$	$F_1$	$F_2$	$F_0$	$F_1$	$F_2$
0	1.00	1.000	0.000	30.6	1.000	0.000	38.7	1.000	0.000	41.0
10	0.48							1.028	-0.330	43.2
20	0.09	1.193	-2.623	50.2	1.067	-0.890	45.6	1.032	-0.430	44.3
30	0.01							1.033	-0.445	44.5
40	0.00	1.158	-1.680	48.5	1.068	-0.920	46.0	.	.	.
50	.							.	.	.
60	.	1.003	-0.077	31.8	1.068	-0.920	46.0	.	.	.
70	.									
80		1.000	0.000	30.6	1.068	-0.920	46.0			
90		.	.	.						
100		.	.	.	1.068	-0.920	46.0			
110		.	.	.						
120					1.001	-0.030	39.2			
130										
140					1.000	0.000	38.7			
150					.	.	.			
160					.	.	.			
170					.	.	.			
180										
190										
200										

$F_0$  is dimensionless;  $F_1$  has dimensions of microseconds;  $F_2$  has dimensions of  $(\mu\text{sec})^2$ .

A column of periods means that the function continues unchanged through the maximum delay for the mode.

measurements have shown that the receiver spectrum has narrowed in time, the  $\rho_n$  (10- $\mu$ sec) value changing from 0.48 to 0.54. Since much data from several years had already been analyzed with the  $\rho_n$  of Table A-1 before this time variation was discovered, it was decided to continue to analyze all data with this same  $\rho_n$  for consistency. The effects upon the temperatures deduced from the data due to these inaccuracies in the adopted  $\rho_n$  have not been evaluated, but are probably small.

### B. Pulse-Shape Distortions

The pulse waveforms employed in the 2-pulse experiments are designed to be perfectly rectangular and flat. Rise and fall times in the equipment are, of course, finite, and the main-power capacitor-bank discharge during pulse transmission causes the pulse shapes to droop with time. In addition, significant pulse timing errors have been identified. All these factors directly enter into the calculation of the correlation function of the pulse waveform  $\rho_w$  of Eq. (A-1) needed for calculation of the effects of instrumental smearing upon measurement of the ionospheric correlation function.

The droop in the pulse waveforms due to main-power capacitor-bank discharge affects all transmission schemes. Experimentation with the equipment has shown that this power droop is well described as  $dP/P = dt/15$ , where  $P$  is power and  $t$  is time in milliseconds. Since 0.4 msec is the longest pulse transmitted in the 2-pulse experiments, this distortion is small but significant. Correction for this effect should rigorously be made by using the true, drooping waveform to calculate the true  $\rho_w$  of Eq. (A-1). Since the correction is small, however, it was decided to make the simple correction for power variation vs time and ignore the slight distortion in waveform shape, which should be a second-order effect. In making this correction, the real pulse-transmission scheme using close- and wide-spaced pulse pairs on different frequencies must be accounted for. The result for the droop correction is that the measured autocorrelation function should be multiplied by the correction factor  $f$

$$f = 1 + \tau/15000 \quad \tau \leq 190 \mu\text{sec}$$

$$f = 1 + (\tau - 200)/15000 \quad \tau \geq 200 \mu\text{sec}$$

for lag  $\tau$  in microseconds.

The finite slopes of the leading and trailing edges of the transmitted pulses, due to the finite rise and fall times of the pulse-generating equipment, seem to be important only for Mode F because of the shortness of the F-Mode pulse. The rise and fall times cannot be considered very short compared with the 40- $\mu$ sec F-Mode pulse length; a rounding of the leading edge is especially apparent. Were all F-Mode pulses of the same length, this rounding would be of small importance. The 20- and 40- $\mu$ sec lag waveforms, however, use 60- and 80- $\mu$ sec pulses, and the effect of leading-edge rounding is relatively different for these lags compared with other lag waveforms.

Investigation of the leading-edge pulse rounding for Mode F uncovered timing errors in this mode which were much more serious than the pulse edge-rounding. First, the basic 40- $\mu$ sec pulse length was discovered to be 39  $\mu$ sec instead. This difference, in itself, is not detrimental since  $\rho_w$  of Eq. (A-1) is easily modified to account for it were this basic pulse length used consistently. Measurements of waveforms for other lags, however, have shown that a 58- $\mu$ sec, not a 59- $\mu$ sec, pulse is used for the 20- $\mu$ sec lag, and that two 36- $\mu$ sec pulses separated by a 6- $\mu$ sec gap are used instead of two 39- $\mu$ sec pulses separated by a 1- $\mu$ sec gap for the 40- $\mu$ sec lag.

Furthermore, this 6- $\mu$ sec gap appears to be more triangular than rectangular in shape and, due to the shortness of the pulses, the pulse edges appear to be significantly slanted. These discrepancies in the F-Mode pulse waveforms have been seen to produce quite detrimental effects in the measured autocorrelation functions, and even correction for the major timing errors in the waveforms was not successful in sufficiently removing observed discrepancies. Due to the complexities, uncertainties, and discrepancies encountered in accounting and correcting for these errors and distortions of the transmitted waveforms, the 20- and 40- $\mu$ sec lags have been completely ignored in analyzing F-Mode data.

### C. Transmitter Chirp

Although all the frequencies employed in the transmitter and receiver are derived from a single stable frequency standard, the RF phase difference between a pair of transmitter pulses differs from that expected due to transmitter chirp. This arises because the transit time of the electron beam in the transmitter klystron amplifier changes during the course of the pulse. This effect is open to direct experimental investigation, or may be calculated from first principles.

To a first approximation, the voltage  $V_t$  applied to the klystron varies during the pulse as

$$\frac{dV_t}{dt} = -I_t/C \quad (\text{A-10})$$

where  $I_t$  is klystron current, and  $C$  is the capacity of the high-voltage condenser that stores the energy for the pulse. Equation (A-10) assumes that  $I_t$  remains constant during the pulse, though, in reality, this is not precisely true. The electrons in the beam are accelerated between the cathode and ring anode by the potential  $V_t$ , and thereby achieve a speed  $V_e$  given in

$$\frac{1}{2} M_e V_e^2 = V_t e$$

where  $e$  and  $M_e$  are the charge and mass of an electron, respectively. It follows that

$$V_e = \left( \frac{2eV_t}{M_e} \right)^{1/2}$$

If  $d$  is the distance between the input and output cavities in the klystron, there will be a phase shift between the two of

$$\begin{aligned} \phi &= -\frac{2\pi f d}{V_e} \\ &= -2\pi f d \left( \frac{M_e}{2eV_t} \right)^{1/2} \quad \text{radian} \end{aligned}$$

where  $f$  is the radar frequency. The change in  $V_t$  during the pulse produces a change in  $\phi$  at a rate

$$\begin{aligned} \frac{d\phi}{dt} &= 2\pi f d \sqrt{\frac{M_e}{2e}} \frac{1}{2} \frac{1}{V_t^{3/2}} \frac{dV_t}{dt} \\ &= -\pi f d \sqrt{\frac{M_e}{2eV_t^3}} \frac{I_t}{C} \end{aligned}$$

This, in turn, leads to a frequency shift in the transmitted pulse of

$$\begin{aligned}\Delta f &= \frac{1}{2\pi} \frac{d\phi}{dt} \\ &= -\frac{1}{2} fd \sqrt{\frac{M_e}{2eV_t^3}} \frac{I_t}{C} .\end{aligned}\tag{A-11}$$

For the case of the Millstone Hill UHF transmitter (employing Elmax X626 klystrons),  $d = 108$  cm,  $C = 24$   $\mu$ F so that Eq. (A-11) reduces to

$$\Delta f = -1.67 \times 10^7 \frac{I_t}{V_t^{3/2}} .$$

In practice,  $\Delta f$  is typically of the order of  $-23$  Hz. This corresponds to an apparent doppler shift which, unless corrected, will be interpreted as a plasma drift away from the radar of  $\sim 8$  m/sec. To compensate for this, a correction must be applied to any drift velocities obtained from Modes G and H.

APPENDIX B  
STATISTICAL ERRORS IN CORRELATION-FUNCTION MEASUREMENTS

I. EXPRESSIONS FOR UNNORMALIZED CORRELATION FUNCTIONS

The correlation functions are estimated from digital samples of orthogonal receiver outputs (sine and cosine channels). In practice, pulse transmission may be made on two frequencies during the same sweep, and the returns separated into two pairs of orthogonal outputs. For our purposes, this may be taken as being equivalent to two separate sweeps and one orthogonal receiver.

Samples from sweep  $i$  at time  $t$  (measured from the commencement of the sweep) are denoted by  $Y_i(t)$  for the sine output and  $U_i(t)$  for the cosine output. Primes are used (i.e.,  $Y_i', U_i'$ ) to distinguish samples taken in the noise region of the sweep (near the end) from samples taken in the signal-plus-noise region. In calculating the autocorrelation function of the incoherent scatter signal, the computer forms certain products of the samples in real time and averages over a number of sweeps.

In general, the unnormalized real part of the autocorrelation function  $A_R(\tau)$  for time lag  $\tau$  is calculated according to the expression

$$\begin{aligned}
 A_R(\tau) = & \frac{1}{2MK_s} \sum_{i=1}^{K_s} \sum_{j=0}^{M-1} [Y_i(t+j\epsilon) Y_i(t+\tau+j\epsilon) + U_i(t+j\epsilon) U_i(t+\tau+j\epsilon)] \\
 & - \frac{1}{2K_n} \sum_{i=1}^{K_n} [Y_i'(t) Y_i'(t+\tau) + U_i'(t) U_i'(t+\tau)] \\
 & - \frac{1}{MK_s} \sum_{i=1}^{K_s/2} \sum_{j=0}^{M-1} [Y_{2i-1}(t+j\epsilon) Y_{2i}(t+\tau+j\epsilon) \\
 & \quad + U_{2i-1}(t+j\epsilon) U_{2i}(t+\tau+j\epsilon)] \quad . \quad (B-1)
 \end{aligned}$$

The corresponding unnormalized imaginary part of the autocorrelation function  $A_I(\tau)$  is given by

$$\begin{aligned}
 A_I(\tau) = & \frac{1}{2MK_s} \sum_{i=1}^{K_s} \sum_{j=0}^{M-1} [Y_i(t+j\epsilon) U_i(t+\tau+j\epsilon) - Y_i(t+\tau+j\epsilon) U_i(t+j\epsilon)] \\
 & - \frac{1}{2K_n} \sum_{i=1}^{K_n} [Y_i'(t) U_i'(t+\tau) - Y_i'(t+\tau) U_i'(t)] \\
 & - \frac{1}{MK_s} \sum_{i=1}^{K_s/2} \sum_{j=0}^{M-1} [Y_{2i-1}(t+j\epsilon) U_{2i}(t+\tau+j\epsilon) \\
 & \quad - Y_{2i}(t+\tau+j\epsilon) U_{2i-1}(t+j\epsilon)] \quad . \quad (B-2)
 \end{aligned}$$



In Eqs. (B-1) and (B-2),  $K_s$  is the number of sweeps for which samples are taken in the signal-plus-noise region,  $K_n$  is the number of sample pairs taken in the noise region.  $M$  pairs of sine and cosine samples separated by  $\tau$  are used to calculate the first and third terms. If  $M \neq 1$ , the separation of one pair of samples from the next is taken to be a constant,  $\epsilon$ .

The first terms in Eqs. (B-1) and (B-2) contain contributions from incoherent scatter signal, system noise, and possibly also clutter returns from distant hills and airplanes. The purpose of the second term is to subtract the system noise contribution. Each pair of noise-region samples in this term may not necessarily be taken in different sweeps or sweeps where the separation of the transmitted pulses is  $\tau$ . It is assumed, however, that noise samples with different subscripts are uncorrelated, i.e.,  $\langle Y_i Y_j \rangle = \langle Y_i \rangle \langle Y_j \rangle$  for  $i \neq j$ . The brackets  $\langle \rangle$  denote an ensemble average or expected value.

The third terms in Eqs. (B-1) and (B-2) effect a clutter subtraction. These terms are only present in F-Mode calculations, but are included here for generality. Each pair of samples used in forming products in these terms is taken from consecutive sweeps with a pulse spacing of  $\tau$ . There are only half as many products used in calculating term three as compared with term one.

## II. EVALUATION OF PRODUCTS INVOLVING RECEIVER SAMPLES

In order to evaluate the expectation and variance of terms in Eqs. (B-1) and (B-2), the basic assumption is made that the samples  $Y_i(t)$  and  $U_i(t)$  are normal variables with zero mean and variance  $\sigma^2$ . Furthermore, each pair of variables  $[Y_i(t), Y_i(t + \tau)]$ ,  $[Y_i(t), U_i(t + \tau)]$ ,  $[U_i(t), U_i(t + \tau)]$ , and  $[U_i(t), Y_i(t + \tau)]$  is taken to have a bivariate normal distribution. The correlation coefficients  $\rho_R(\tau)$  and  $\rho_I(\tau)$  for these distributions are defined by

$$\begin{aligned} \langle Y_i(t) Y_i(t + \tau) \rangle &= \langle U_i(t) U_i(t + \tau) \rangle = \sigma^2 \rho_R(\tau) \\ \langle Y_i(t) U_i(t + \tau) \rangle &= -\langle U_i(t) Y_i(t + \tau) \rangle = \sigma^2 \rho_I(\tau) \end{aligned} \quad (B-3)$$

In complex notation, samples  $X_i(t)$  of the receiver output are written

$$X_i(t) = Y_i(t) - IU_i(t) \quad (B-4)$$

where  $I = \sqrt{-1}$ . The complex correlation function is given by

$$\langle X_i(t) X_i^*(t + \tau) \rangle = 2\sigma^2 [\rho_R(\tau) + I\rho_I(\tau)] = 2\sigma^2 \rho(\tau) \quad (B-5)$$

Thus,  $\rho_R(\tau)$  and  $\rho_I(\tau)$  represent the real and imaginary parts of the complex correlation function of the receiver output in the signal-plus-noise region.  $\rho_R(\tau)$  is an even function of  $\tau$ ,  $\rho_I(\tau)$  is an odd function of  $\tau$ , and we have  $\rho_R(0) = 1$ ,  $\rho_I(0) = 0$ .

Adopting the notation

$$Z_i = Y_i(t + \tau) \quad , \quad V_i = U_i(t + \tau) \quad (B-6)$$

we may summarize the following properties of samples in the signal-plus-noise region

$$\begin{aligned}
\langle Y_i \rangle &= \langle Z_i \rangle = \langle U_i \rangle = \langle V_i \rangle = 0 \\
\langle Y_i^2 \rangle &= \langle Z_i^2 \rangle = \langle U_i^2 \rangle = \langle V_i^2 \rangle = \sigma^2 \\
\langle Y_i Z_i \rangle &= \langle U_i V_i \rangle = \sigma^2 \rho_R(\tau) \\
\langle Y_i V_i \rangle &= -\langle U_i Z_i \rangle = \sigma^2 \rho_I(\tau) \quad . \quad (B-7)
\end{aligned}$$

More complicated relationships involving the expectation value of products of four samples may be evaluated using the theorem,

$$\langle X_1 X_2 X_3 X_4 \rangle = \langle X_1 X_2 \rangle \langle X_3 X_4 \rangle + \langle X_1 X_3 \rangle \langle X_2 X_4 \rangle + \langle X_1 X_4 \rangle \langle X_2 X_3 \rangle \quad (B-8)$$

which applies when  $X_1, X_2, X_3,$  and  $X_4$  are jointly normal random variables with zero mean. For example,

$$\langle Y_i Z_i U_i V_i \rangle = \sigma^4 [\rho_R^2(\tau) - \rho_I^2(\tau)] \quad (B-9)$$

$$\langle Y_i^2 Z_i^2 \rangle = \sigma^4 [1 + 2\rho_R^2(\tau)] \quad . \quad (B-10)$$

In the noise region, the variance and complex correlation function of the receiver output are denoted by  $\sigma_n^2$  and  $\rho_n(\tau) = \rho_{nR}(\tau) + j\rho_{nI}(\tau)$ . Defining

$$Z_i' = Y_i'(t + \tau) \quad , \quad V_i' = U_i'(t + \tau) \quad (B-11)$$

we obtain similar relationships between the primed samples as in Eq. (B-7) by substituting  $\sigma_n^2$  and  $\rho_n$  for  $\sigma$  and  $\rho$ .

The clutter term in Eqs. (B-1) and (B-2) subtracts any correlation that exists from sweep-to-sweep. In evaluating the variances of  $A_R(\tau)$  and  $A_I(\tau)$ , the assumption is made that there is, in fact, no correlation from sweep-to-sweep, i.e., for  $i \neq j$

$$\begin{aligned}
\langle Y_i(t_1) Y_j(t_2) \rangle &= \langle Y_i(t_1) \rangle \langle Y_j(t_2) \rangle = 0 \\
\langle U_i(t_1) U_j(t_2) \rangle &= \langle U_i(t_1) \rangle \langle U_j(t_2) \rangle = 0 \quad . \quad (B-12)
\end{aligned}$$

Under this assumption, the presence of the clutter term does not affect the expected values of  $A_R(\tau)$  and  $A_I(\tau)$ , but it does affect their variances and so must be retained. The effect of non-zero clutter is evaluated in an empirical manner in Appendix A.

### III. VARIANCES OF THE UNNORMALIZED COMPLEX CORRELATION FUNCTIONS

We may now proceed with the computation of the variances of the unnormalized correlation functions  $A_R(\tau)$  and  $A_I(\tau)$  defined in Eqs. (B-1) and (B-2). Adopting the notation

$$\begin{aligned}
Y_{ij} &= Y_i(t + j\epsilon) \quad , \quad Z_{ij} = Y_i(t + \tau + j\epsilon) \\
U_{ij} &= U_i(t + j\epsilon) \quad , \quad V_{ij} = U_i(t + \tau + j\epsilon) \\
C_{ij} &= Y_{ij} Z_{ij} + U_{ij} V_{ij} \quad , \quad D_{2i,j} = Y_{2i-1,j} Z_{2i,j} + U_{2i-1,j} V_{2i,j} \\
E_{ij} &= Y_{ij} V_{ij} - Z_{ij} U_{ij} \quad , \quad F_{2i,j} = Y_{2i-1,j} V_{2i,j} - Z_{2i,j} U_{2i-1,j} \\
C_i' &= Y_i' Z_i' + U_i' V_i' \quad , \quad E_i' = Y_i' V_i' - Z_i' U_i' \quad (B-13)
\end{aligned}$$

we may write,

$$A_R(\tau) = \frac{1}{2MK_s} \sum_{i=1}^{K_s} \sum_{j=0}^{M-1} C_{ij} - \frac{1}{2K_n} \sum_{i=1}^{K_n} C_i' - \frac{1}{MK_s} \sum_{i=1}^{K_s/2} \sum_{j=0}^{M-1} D_{2i,j} \quad (B-14)$$

$$A_I(\tau) = \frac{1}{2MK_s} \sum_{i=1}^{K_s} \sum_{j=0}^{M-1} E_{ij} - \frac{1}{2K_n} \sum_{i=1}^{K_n} E_i' - \frac{1}{MK_s} \sum_{i=1}^{K_s/2} \sum_{j=0}^{M-1} F_{2i,j} \quad (B-15)$$

The complex correlation function after system noise and clutter subtraction will be referred to as the measured correlation function  $\rho_m(\tau)$ , i.e.,  $\langle A_R(\tau) \rangle - I \langle A_I(\tau) \rangle = \sigma_m^2 \rho_m(\tau)$ .  $\rho_m(\tau)$  is related to the correlation function of the incoherent scatter signal (see Sec. VII below, and also Appendix A).

Taking expected values in Eqs. (B-14) and (B-15),

$$\begin{aligned} \langle A_R(\tau) \rangle &= \sigma^2 \rho_R(\tau) - \sigma_n^2 \rho_{nR}(\tau) = \sigma_m^2 \rho_{mR}(\tau) \\ \langle A_I(\tau) \rangle &= \sigma^2 \rho_I(\tau) - \sigma_n^2 \rho_{nI}(\tau) = \sigma_m^2 \rho_{mI}(\tau) \end{aligned} \quad (B-16)$$

The variance of  $A_R(\tau)$ , the variance of  $A_I(\tau)$ , and the covariance of  $A_R(\tau)$  and  $A_I(\tau)$  are given by

$$\sigma_R^2(\tau) = \langle A_R^2(\tau) \rangle - \langle A_R(\tau) \rangle^2 \quad (B-17)$$

$$\sigma_I^2(\tau) = \langle A_I^2(\tau) \rangle - \langle A_I(\tau) \rangle^2 \quad (B-18)$$

$$\sigma_{R,I}(\tau) = \langle A_R(\tau) A_I(\tau) \rangle - \langle A_R(\tau) \rangle \langle A_I(\tau) \rangle \quad (B-19)$$

To calculate  $\sigma_R^2$ , we square the right-hand side of Eq. (B-14) for  $A_R$ , take expected values, and then subtract  $\langle A_R \rangle^2$ . A great many of the resulting terms disappear because no pair of the three variables  $C_{ij}$ ,  $C_i'$ , and  $D_{2i,j}$  is correlated. Also, there is no correlation between any pair of  $C_{ij}$  variables, or any pair of  $C_i'$  variables, or any pair of  $D_{2i,j}$  variables for which the subscript  $i$  (sweep number) is different. With these simplifications,  $\sigma_R^2(\tau)$  may be written

$$\begin{aligned} \sigma_R^2(\tau) &= \frac{1}{4MK_s} \left\{ \langle C_{ij}^2 \rangle - \langle C_{ij} \rangle^2 + \frac{2}{M} \sum_{k=1}^{M-1} (M-k) [\langle C_{ij} C_{i,j+k} \rangle - \langle C_{ij} \rangle \langle C_{i,j+k} \rangle] \right\} \\ &\quad + \frac{1}{4K_n} [\langle C_i'^2 \rangle - \langle C_i' \rangle^2] \\ &\quad + \frac{1}{2MK_s} \left\{ \langle D_{2i,j}^2 \rangle - \langle D_{2i,j} \rangle^2 + \frac{2}{M} \sum_{k=1}^{M-1} (M-k) \right. \\ &\quad \left. \times [\langle D_{2i,j} D_{2i,j+k} \rangle - \langle D_{2i,j} \rangle \langle D_{2i,j+k} \rangle] \right\} \quad (B-20) \end{aligned}$$

The expressions in Eq. (B-20) involving the variables  $C_{ij}$ ,  $C_i'$ , and  $D_{2i,j}$  may readily be evaluated in terms of the autocorrelation functions and variances of the receiver output in the signal-plus-noise region ( $\rho_R$ ,  $\rho_I$ , and  $\sigma^2$ ) and in the noise region ( $\rho_{nR}$ ,  $\rho_{nI}$ , and  $\sigma_n^2$ ). These results are

$$\begin{aligned}
\langle C_{ij} \rangle &= 2\sigma^2 \rho_R(\tau) \quad , \quad \langle C_{ij}^2 \rangle = 2\sigma^4 [1 + 3\rho_R^2(\tau) - \rho_I^2(\tau)] \\
\langle C_{ij} C_{i,j+k} \rangle &= 2\sigma^4 [2\rho_R^2(\tau) + \rho_R^2(k\epsilon) + \rho_I^2(k\epsilon) + \rho_R(\tau + k\epsilon) \\
&\quad \times \rho_R(\tau - k\epsilon) + \rho_I(\tau + k\epsilon) \rho_I(\tau - k\epsilon)] \\
\langle C_i' \rangle &= 2\sigma_n^2 \rho_{nR}(\tau) \quad , \quad \langle C_i'^2 \rangle = 2\sigma_n^4 [1 + 3\rho_{nR}^2(\tau) - \rho_{nI}^2(\tau)] \\
\langle D_{2i,j} \rangle &= 0 \quad , \quad \langle D_{2i,j}^2 \rangle = 2\sigma^4 \quad , \\
\langle D_{2i,j} D_{2i,j+k} \rangle &= 2\sigma^4 [\rho_R^2(k\epsilon) + \rho_I^2(k\epsilon)] \quad . \quad (B-24)
\end{aligned}$$

The general result for  $\sigma_R^2(\tau)$  is then

$$\begin{aligned}
\sigma_R^2(\tau) &= \frac{\sigma^4}{2MK_S} \left\{ S + \rho_R^2(\tau) - \rho_I^2(\tau) \right. \\
&\quad + \frac{2}{M} \sum_{k=1}^{M-1} (M-k) [S\rho_R^2(k\epsilon) + S\rho_I^2(k\epsilon) + \rho_R(\tau + k\epsilon) \rho_R(\tau - k\epsilon) \\
&\quad \quad \quad \left. - \rho_I(\tau + k\epsilon) \rho_I(\tau - k\epsilon)] \right. \\
&\quad \left. + \frac{\sigma_n^4}{\sigma^4} \frac{MK_S}{K_n} [1 + \rho_{nR}^2(\tau) - \rho_{nI}^2(\tau)] \right\} \quad (B-22)
\end{aligned}$$

where  $S = 1$  if no clutter subtraction is used in calculating  $A_R(\tau)$ , and  $S = 3$  if a clutter term is used. The summation term must be omitted if  $M = 1$ , i.e., if only one product is formed per sweep.

The calculation of the variance of  $A_I(\tau)$  follows along similar lines to the calculation of the variance of  $A_R(\tau)$ .  $\sigma_I^2(\tau)$  is given by Eq. (B-20) if the variables  $E_{ij}$ ,  $F_{2i,j}$ , and  $E_i'$  are substituted for  $C_{ij}$ ,  $D_{2i,j}$ , and  $C_i'$ , respectively.

The general result for  $\sigma_I^2(\tau)$  is

$$\begin{aligned}
\sigma_I^2(\tau) &= \frac{\sigma^4}{2MK_S} \left\{ S + \rho_I^2(\tau) - \rho_R^2(\tau) \right. \\
&\quad + \frac{2}{M} \sum_{k=1}^{M-1} (M-k) [S\rho_R^2(k\epsilon) + S\rho_I^2(k\epsilon) - \rho_R(\tau + k\epsilon) \rho_R(\tau - k\epsilon) \\
&\quad \quad \quad \left. + \rho_I(\tau + k\epsilon) \rho_I(\tau - k\epsilon)] \right. \\
&\quad \left. + \frac{\sigma_n^4}{\sigma^4} \frac{MK_S}{K_n} [1 + \rho_{nI}^2(\tau) - \rho_{nR}^2(\tau)] \right\} \quad . \quad (B-23)
\end{aligned}$$

An equation for the covariance of  $A_R(\tau) A_I(\tau)$  may be derived in a similar manner as Eq. (B-20),

$$\begin{aligned}
\sigma_{R,I}(\tau) = & \frac{1}{4MK_s} \left\{ \langle C_{ij} E_{ij} \rangle - \langle C_{ij} \rangle \langle E_{ij} \rangle + \frac{1}{M} \sum_{k=1}^{M-1} (M-k) \right. \\
& \times [ \langle C_{ij} E_{i,j+k} \rangle - \langle C_{ij} \rangle \langle E_{i,j+k} \rangle \\
& + \langle E_{ij} C_{i,j+k} \rangle - \langle E_{ij} \rangle \langle C_{i,j+k} \rangle ] \left. \right\} \\
& + \frac{1}{4K_n} [ \langle C'_i E'_i \rangle - \langle C'_i \rangle \langle E'_i \rangle ] \\
& + \frac{1}{2MK_s} \left\{ \langle D_{2i,j} F_{2i,j} \rangle - \langle D_{2i,j} \rangle \langle F_{2i,j} \rangle + \frac{1}{M} \sum_{k=1}^{M-1} (M-k) \right. \\
& \times [ \langle D_{2i,j} F_{2i,j+k} \rangle - \langle D_{2i,j} \rangle \langle F_{2i,j+k} \rangle \\
& + \langle F_{2i,j} D_{2i,j+k} \rangle - \langle F_{2i,j} \rangle \langle D_{2i,j+k} \rangle ] \left. \right\} . \tag{B-24}
\end{aligned}$$

The terms required to evaluate this are

$$\begin{aligned}
\langle C_{ij} E_{ij} \rangle &= 8\sigma^4 \rho_I(\tau) \rho_R(\tau) \\
\langle C_{ij} E_{i,j+k} \rangle &= \langle E_{ij} C_{i,j+k} \rangle \\
&= \sigma^4 \{ 4\rho_R(\tau) \rho_I(\tau) + [\rho_R(\tau + k\epsilon) + \rho_R(\tau - k\epsilon)] \\
&\quad \times [\rho_I(\tau + k\epsilon) + \rho_I(\tau - k\epsilon)] \} \\
\langle C'_i E'_i \rangle &= 8\sigma_n^4 \rho_{nI}(\tau) \rho_{nR}(\tau) \\
\langle D_{2i,j} F_{2i,j+k} \rangle &= \langle F_{2i,j} D_{2i,j+k} \rangle = 0 \tag{B-25}
\end{aligned}$$

and the result of substituting these terms into Eq. (B-24) is

$$\begin{aligned}
\sigma_{R,I}(\tau) = & \frac{\sigma^4}{2MK_s} \left\{ 2\rho_R(\tau) \rho_I(\tau) + \frac{1}{M} \sum_{k=1}^{M-1} (M-k) [\rho_R(\tau + k\epsilon) + \rho_R(\tau - k\epsilon)] \right. \\
& \times [\rho_I(\tau + k\epsilon) + \rho_I(\tau - k\epsilon)] \\
& + \frac{\sigma_n^4}{\sigma^4} \frac{2MK_s}{K_n} \rho_{nR}(\tau) \rho_{nI}(\tau) \left. \right\} . \tag{B-26}
\end{aligned}$$

#### IV. MAGNITUDE OF NOISE SUBTRACTION TERM

The last terms in Eqs. (B-22), (B-23), and (B-26) (for  $\sigma_R^2$ ,  $\sigma_I^2$ , and  $\sigma_{R,I}$ ) result from the system noise subtraction. This term is of order  $K_n^{-1}$  compared with order  $(MK_s)^{-1}$  for the other terms. The values of  $M$  and the ratio  $K_n/K_s$  for Modes F, G, and H are given in Table B-1.

TABLE B-1 VALUES OF $K_n/K_s$ AND $M$ FOR THE 2-PULSE MODES		
Mode	$K_n/K_s$	$M$
F	75 (20)*	1 or 3
G	52 (20)	1, 3, or 5
H	175 (20)	1, 3, or 5

\*Numbers in parentheses apply to data taken prior to 6 November 1970. See also Fig. 1 and Table XI in main text.

Noting that  $\sigma^2 \geq \sigma_n^2$  and using the values in Table B-1, it is seen that the noise subtraction term is always at least an order-of-magnitude smaller than the other terms and may be safely neglected.

#### V. CORRELATION OF ESTIMATES AT DIFFERENT LAGS

The unnormalized correlation estimates at different lags [i.e.,  $A_R(\tau_1)$ ,  $A_R(\tau_2)$ ] are calculated using signal-plus-noise samples from different (and hence independent) sweeps, but they are still correlated because the noise subtraction terms in Eqs. (B-1) and (B-2) use samples from the same sweeps for all lags.

The covariance of  $A_R(\tau_1)$ ,  $A_R(\tau_2)$  is

$$\sigma_{RR}(\tau_1, \tau_2) = \frac{1}{4K_n^2} \left[ \left\langle \sum_{i=1}^{K_n} C_i'(\tau_1) \sum_{i=1}^{K_n} C_i'(\tau_2) \right\rangle - \left\langle \sum_{i=1}^{K_n} C_i'(\tau_1) \right\rangle \left\langle \sum_{i=1}^{K_n} C_i'(\tau_2) \right\rangle \right] \quad (\text{B-27})$$

which may be evaluated to

$$\sigma_{RR}(\tau_1, \tau_2) = \frac{\sigma_n^4}{2K_n} [\rho_{nR}(\tau_2 - \tau_1) + \rho_{nR}(\tau_1) \rho_{nR}(\tau_2) - \rho_{nI}(\tau_1) \rho_{nI}(\tau_2)] \quad (\text{B-28})$$

Similarly, the covariance of  $A_R(\tau_1)$ ,  $A_I(\tau_2)$  is

$$\sigma_{RI}(\tau_1, \tau_2) = \frac{\sigma_n^4}{K_n} [\rho_{nI}(\tau_2 - \tau_1) + \rho_{nR}(\tau_2) \rho_{nI}(\tau_1) + \rho_{nR}(\tau_1) \rho_{nI}(\tau_2)] \quad (B-29)$$

The covariance of the estimates at different lags is of order  $K_n^{-1}$ , while the variances are of order  $(MK_s)^{-1}$ . In the noise subtraction method used,  $K_n$  is always an order-of-magnitude larger than  $MK_s$  (Table B-1), and the covariance may always be neglected without serious error.

## VI. VARIANCE IN THE AMPLITUDE OF THE UNNORMALIZED COMPLEX CORRELATION FUNCTION

The unnormalized amplitude  $B(\tau)$  of the complex correlation function after noise and clutter subtraction [Eqs. (B-1), (B-2)] is

$$B(\tau) = [A_R^2(\tau) + A_I^2(\tau)]^{1/2} \quad (B-30)$$

We wish to derive an estimate of the expectation of  $B(\tau)$  and its variance  $\sigma_B^2(\tau)$  for later use.

Approximate expressions for evaluating the expectation and variance of a general function  $f(\chi_1, \chi_2)$  of two random variables  $\chi_1, \chi_2$  are

$$\langle f \rangle = \langle f(\chi_1, \chi_2) \rangle \approx f(\langle \chi_1 \rangle, \langle \chi_2 \rangle) \quad (B-31)$$

$$\begin{aligned} \sigma_f^2 = \langle f^2(\chi_1, \chi_2) \rangle - \langle f(\chi_1, \chi_2) \rangle^2 \approx & \sigma_1^2 \left( \frac{\partial f}{\partial \chi_1} \right)^2 + 2\sigma_{1,2} \left( \frac{\partial f}{\partial \chi_1} \right) \left( \frac{\partial f}{\partial \chi_2} \right) \\ & + \sigma_2^2 \left( \frac{\partial f}{\partial \chi_2} \right)^2 \end{aligned} \quad (B-32)$$

where  $\sigma_1^2$ ,  $\sigma_2^2$ , and  $\sigma_{1,2}$  are, respectively, the variances of  $\chi_1$  and  $\chi_2$  and the covariance of  $\chi_1$  and  $\chi_2$ . The partial differential coefficients are evaluated at  $\chi_1 = \langle \chi_1 \rangle$ ,  $\chi_2 = \langle \chi_2 \rangle$ . In the present applications, Eq. (B-31) neglects terms of the order  $K_s^{-2}$ . Since  $K_s$  is large, these approximations are adequate for our purposes.

The expectation of  $B(\tau)$  is then

$$\begin{aligned} \langle B(\tau) \rangle &= [\langle A_R(\tau) \rangle^2 + \langle A_I(\tau) \rangle^2]^{1/2} \\ &= \sigma_m^2 [\rho_{mR}^2(\tau) + \rho_{mI}^2(\tau)]^{1/2} \end{aligned} \quad (B-33)$$

The variance of  $B(\tau)$

$$\begin{aligned} \sigma_B^2(\tau) &= \langle B(\tau) \rangle^{-2} [\langle A_R(\tau) \rangle^2 \sigma_R^2(\tau) + \langle A_I(\tau) \rangle^2 \sigma_I^2(\tau) + 2\langle A_R(\tau) \rangle \\ &\quad \times \langle A_I(\tau) \rangle \sigma_{R,I}(\tau)] \\ &= [\rho_{mR}^2(\tau) + \rho_{mI}^2(\tau)]^{-1} [\rho_{mR}^2(\tau) \sigma_R^2(\tau) + \rho_{mI}^2(\tau) \sigma_I^2(\tau) \\ &\quad + 2\rho_{mR}(\tau) \rho_{mI}(\tau) \sigma_{R,I}(\tau)] \end{aligned} \quad (B-34)$$

where  $\sigma_R^2$ ,  $\sigma_I^2$ , and  $\sigma_{R,I}$  are given in Eqs. (B-22), (B-23), and (B-26).

## VII. RELATION BETWEEN MEASURED AND INCOHERENT SCATTER CORRELATION FUNCTIONS

The unnormalized complex correlation function obtained after system noise and clutter subtraction is denoted by  $\sigma_m^2 \rho_m(\tau)$ .

$$\sigma_m^2 \rho_m(\tau) = \langle A_R(\tau) \rangle + I \langle A_I(\tau) \rangle \quad (B-35)$$

Using Eq. (B-16),

$$\sigma_m^2 \rho_m(\tau) = \sigma^2 \rho(\tau) - \sigma_n^2 \rho_n(\tau) \quad (B-36)$$

As both the signal-plus-noise correlation function  $\rho(\tau)$  and the noise correlation function  $\rho_n(\tau)$  are Hermitian, so also is  $\rho_m(\tau)$ , i.e.,  $\rho_m(\tau) = \rho_m^*(-\tau)$ . Assuming the system noise has the same statistics in the signal-plus-noise region as in the noise region, the measured correlation function  $\rho_m(\tau)$  may be written in terms of the incoherent scatter correlation function  $\rho_s(\tau) \exp[i\omega_0 \tau]$  (Appendix A)

$$\rho_m(\tau) = \frac{[\rho_w(\tau) \rho_s(\tau)] * \rho_n(\tau)}{\{[\rho_w(\tau) \rho_s(\tau)] * \rho_n(\tau)\}_{\tau=0}} \quad (B-37)$$

where  $\omega_0$  is the transmitter frequency. The weighting function  $\rho_w(\tau)$  is the autocorrelation of the transmitter waveform  $V(t)$

$$\rho_w(\tau) = \frac{V(\tau) * V^*(-\tau)}{[V(\tau) * V^*(-\tau)]_{\tau=0}} \quad (B-38)$$

For the experiments being considered, the variance  $\sigma_m^2$  is only estimated when single pulses of the basic length are transmitted ( $\tau = 0$ ). This basic single-pulse variance is denoted by  $\sigma_b^2$ . It is desirable to express the variance  $\sigma_m^2$  for other pulse transmissions in terms of  $\sigma_b^2$

$$\sigma_m^2 = \alpha_\tau \sigma_b^2 \quad (B-39)$$

where

$$\alpha_\tau = \frac{[V_\tau(t) * V_\tau^*(-t)]_{t=0}}{[V_0(t) * V_0^*(-t)]_{t=0}} \quad (B-40)$$

$V_0(t)$  being the transmitted waveform when lag zero is measured, and  $V_\tau(t)$  the transmitted waveform when lag  $\tau$  is measured.  $\alpha_\tau$  is just the ratio of the total transmitted energy for the two waveforms.

It is adequate for our error calculation to simplify Eq. (B-38) by taking  $\rho_s(\tau)$  outside the convolution. More complicated deconvolution procedures are used in practice (Appendix A). Defining a new weighting function  $\rho'_w(\tau)$  by

$$\rho'_w(\tau) = \frac{\rho_w(\tau) * \rho_n(\tau)}{[\rho_w(\tau) * \rho_n(\tau)]_{\tau=0}} \quad (B-41)$$

we may now express the incoherent scatter correlation function in terms of the estimates  $A_R(\tau)$  and  $A_I(\tau)$ ,

$$\rho_s(\tau) = \frac{\langle A_R(\tau) \rangle + I \langle A_I(\tau) \rangle}{\sigma_b^2 \beta(\tau)} \quad (B-42)$$



with

$$\beta(\tau) = \alpha_{\tau} \rho'_{\text{w}}(\tau) \quad . \quad (\text{B-43})$$

Because our aim is to estimate the incoherent scatter correlation function  $\rho_{\text{S}}(\tau)$ , it is preferable to use  $\rho_{\text{S}}(\tau)$  in place of the signal-plus-noise correlation function  $\rho(\tau)$  in the expressions for the variances and covariances of  $A_{\text{R}}(\tau)$  and  $A_{\text{I}}(\tau)$ . It is also preferable to use the estimated quantity  $\sigma_{\text{b}}^2$  rather than  $\sigma^2$  which is not directly estimated. The required substitutions are

$$\sigma^2 = \sigma_{\text{m}}^2 + \sigma_{\text{n}}^2 = \alpha_{\tau} \sigma_{\text{b}}^2 + \sigma_{\text{n}}^2 = \sigma_{\text{b}}^2 (\alpha_{\tau} + x) \quad (\text{B-44})$$

$$\rho(\tau) = \frac{\sigma_{\text{m}}^2 \rho_{\text{m}}(\tau) + \sigma_{\text{n}}^2 \rho_{\text{n}}(\tau)}{\sigma_{\text{m}}^2 + \sigma_{\text{n}}^2} = \frac{\beta(\tau) \rho_{\text{S}}(\tau) + x \rho_{\text{n}}(\tau)}{\alpha_{\tau} + x} \quad (\text{B-45})$$

where the basic-pulse noise-to-signal ratio is  $x$ ,

$$x = \sigma_{\text{n}}^2 / \sigma_{\text{b}}^2 \quad . \quad (\text{B-46})$$

Some additional simplifications may be made in relation to F, G, and H Mode experiments because the lag  $\tau$  at which  $A_{\text{R}}(\tau)$  and  $A_{\text{I}}(\tau)$  [Eqs. (B-1) and (B-2)] are measured is the same as the pulse separation. In this case, and assuming perfect rectangular pulses and no transmitter chirp,

$$\rho_{\text{w}}(\tau) = 1/\alpha_{\tau} \quad (\text{B-47})$$

and

$$\begin{aligned} \alpha_{\tau} &= 1 + \tau/\tau_{\text{B}} && \text{for } \tau \leq \tau_{\text{B}} \\ &= 2 && \text{for } \tau > \tau_{\text{B}} \end{aligned} \quad (\text{B-48})$$

where  $\tau_{\text{B}}$  is the basic pulse length. A further simplification, which should be adequate for error calculations, is  $\rho'_{\text{w}}(\tau) \approx \rho_{\text{w}}(\tau)$ . Thus,  $\beta(\tau) \approx 1$  and Eq. (B-45) becomes

$$\rho(\tau) = \frac{\rho_{\text{S}}(\tau) + x \rho_{\text{n}}(\tau)}{\alpha_{\tau} + x} \quad . \quad (\text{B-49})$$

## VIII. SUMMARY OF RESULTS FOR UNNORMALIZED FUNCTIONS

The results for the expectation and variance of the unnormalized correlation functions  $A_{\text{R}}(\tau)$ ,  $A_{\text{I}}(\tau)$  [Eqs. (B-1) and (B-2)], and the unnormalized amplitude  $B(\tau)$  [Eq. (B-34)] are now summarized. The noise subtracted term is neglected and  $\beta(\tau)$  is taken as unity.

$$\langle A_{\text{R}}(\tau) \rangle = \sigma_{\text{b}}^2 \rho_{\text{SR}}(\tau) \quad (\text{B-50})$$

$$\begin{aligned} \sigma_{\text{R}}^2(\tau) &= \frac{\sigma_{\text{b}}^4}{2\text{MK}_{\text{S}}} \left\{ S(\alpha_{\tau} + x)^2 + p^2(\tau) - q^2(\tau) + \frac{2}{M} \sum_{k=1}^{M-1} (M-k) [\text{Sp}^2(k\epsilon) \right. \\ &\quad \left. + \text{Sq}^2(k\epsilon) + p(\tau + k\epsilon) p(\tau - k\epsilon) - q(\tau + k\epsilon) q(\tau - k\epsilon)] \right\} \quad (\text{B-51}) \end{aligned}$$

$$\langle A_I(\tau) \rangle = \sigma_b^2 \rho_{SI}(\tau) \quad (B-52)$$

$$\sigma_I^2(\tau) = \frac{\sigma_b^4}{2MK_S} \left\{ S(\alpha_\tau + x)^2 + q^2(\tau) + p^2(\tau) + \frac{2}{M} \sum_{k=1}^{M-1} (M-k) [Sq^2(k\epsilon) + Sp^2(k\epsilon) + q(\tau + k\epsilon)q(\tau - k\epsilon) - p(\tau + k\epsilon)p(\tau - k\epsilon)] \right\} \quad (B-53)$$

$$\sigma_{R,I}^2(\tau) = \frac{\sigma_b^4}{2MK_S} \left\{ 2p(\tau)q(\tau) + \frac{1}{M} \sum_{k=1}^{M-1} (M-k) [p(\tau + k\epsilon) + p(\tau - k\epsilon)] \times [q(\tau + k\epsilon) + q(\tau - k\epsilon)] \right\} \quad (B-54)$$

$$\langle B(\tau) \rangle = \sigma_b^2 [\rho_{SR}^2(\tau) + \rho_{SI}^2(\tau)]^{1/2} \quad (B-55)$$

$$\sigma_B^2(\tau) = \frac{[\rho_{SR}^2(\tau)\sigma_R^2(\tau) + \rho_{SI}^2(\tau)\sigma_I^2(\tau) + 2\rho_{SI}(\tau)\rho_{SR}(\tau)\sigma_{R,I}(\tau)]}{[\rho_{SR}^2(\tau) + \rho_{SI}^2(\tau)]} \quad (B-56)$$

where

$$\begin{aligned} p(\tau) &= \rho_{SR}(\tau) + x\rho_{nR}(\tau) \\ q(\tau) &= \rho_{SI}(\tau) + x\rho_{nI}(\tau) \end{aligned} \quad (B-57)$$

The various quantities appearing in these expressions are:

$\rho_s(\tau) = \rho_{SR}(\tau) + I\rho_{SI}(\tau)$	The incoherent scatter correlation function
$\rho_n(\tau) = \rho_{nR}(\tau) + I\rho_{nI}(\tau)$	The system noise correlation function. $\rho_s(\tau)$ and $\rho_n(\tau)$ are both Hermitian, i.e., $\rho_s(\tau) = \rho_s^*(-\tau)$ , $\rho_n(\tau) = \rho_n^*(-\tau)$
x	Noise-to-signal power at the measurement altitude using the basic pulse length $\tau_B$ [Eq. (B-46)]
$\alpha_\tau$	Ratio of total transmitted energy when lag $\tau$ is measured to the total transmitted energy when lag 0 is measured [see Eq. (B-48)]
S	Clutter subtraction constant; $S = 3$ when a clutter subtraction term is used (Mode F), $S = 1$ when no clutter subtraction is made (Modes G and H)

TABLE B-2			
VALUES OF $\tau_B$ , S, AND $C_s$ FOR THE 2-PULSE MODES			
Mode	$\tau_B$ ( $\mu$ sec)	$C_s$ (sec)	S
F	40	0.08	3
G	100	0.08	1
H	200	0.16	1

TABLE B-3				
VALUES OF M AND $\epsilon$ VS ALTITUDE AND LAG FOR THE 2-PULSE MODES				
Mode	Center Altitude* (km)	Lag $\tau$ ( $\mu$ sec)	M	$\epsilon$ ( $\mu$ sec)
F	106 (N/A) to 124 (N/A)	All	1	-
	130 (106) to 166	0 to 80	1	-
	130 (106) to 166	100 to 380	3	20
G	All	0 to 40	1	-
		60 to 100	3	20
		120 to 380	5	20
H	All	0 to 40	1	-
		50 to 90	3	20
		100 to 190	5	20

\*Numbers in parentheses apply to data collected prior to 30 December 1970. See note in Table III of main text regarding altitude changes prior to 16 December 1971; see also Fig. 1 and Table III in main text.

M	Number of products formed in <u>each</u> sweep for a particular lag and altitude
$\epsilon$	Time shift between successive products for a particular lag and altitude, only defined if $M > 1$
$K_s$	Number of sweeps for which lag $\tau$ is measured $K_s = t_s/C_s$ , where $t_s$ is the integration time in seconds and $C_s$ is a constant
$\sigma_b^2$	Variance (power) of incoherent scatter signal at the measurement altitude for the basic pulse transmission

Table B-2 gives  $\tau_B$ ,  $S$ , and  $C_s$  for Modes F, G, and H, while Table B-3 gives  $M$  and  $\epsilon$  as functions of altitude and lag for Modes F, G, and H.

To evaluate the variances we need to have values of  $\rho_s(\tau)$ ,  $\rho_n(\tau)$ , and  $x$ . Since we do not know these functions exactly, the best that can be done is to use quantities whose expectations are the required values. Thus, we may use  $A_R(\tau)/A_R(0)$  for  $\rho_{sR}(\tau)$ ,  $A_I(\tau)/A_R(0)$  for  $\rho_{sI}(\tau)$ ,  $A_{nR}(\tau)/A_{nR}(0)$  for  $\rho_{nR}(\tau)$ ,  $A_{nI}(\tau)/A_{nR}(0)$  for  $\rho_{nI}(\tau)$ , and  $A_{Rn}(0)/[A_R(0) - A_{Rn}(0)]$  for  $x$ , where

$$A_{nR}(\tau) = \frac{1}{2K_n} \sum_{i=1}^{K_n} [Y_i^*(\tau) Y_i^*(t + \tau) + U_i^*(\tau) U_i^*(t + \tau)]$$

$$A_{nI}(\tau) = \frac{1}{2K_n} \sum_{i=1}^{K_n} [Y_i^*(\tau) U_i^*(t + \tau) - Y_i^*(t + \tau) U_i^*(\tau)] \quad (B-58)$$

$A_R(0)$  could be used for the remaining quantity  $\sigma_b^2$ . However,  $\sigma_b^2$  drops out of the expressions for the variances of the normalized correlation function (see next section) and this substitution is not required.

## IX. NORMALIZATION OF CORRELATION-FUNCTION ESTIMATES

Final estimates of the amplitude of the incoherent scatter correlation function may be obtained by dividing the unnormalized estimates Eqs. (B-50), (B-52), or (B-55) by an estimate of  $\sigma_b^2$ . Two methods of deriving an estimate of  $\sigma_b^2$  are considered; one method uses the zero lag measurement, the other uses a theoretical incoherent scatter correlation function. Either  $A_R(\tau)$  or  $B(\tau)$  has to be normalized, depending on the mode of the experiment. The covariances of  $A_R(\tau_1)$  and  $A_R(\tau_2)$  and of  $A_I(\tau_1)$  and  $A_I(\tau_2)$  are ignored, as discussed in Sec. V of this appendix.

### A. Normalization Using Zero Lag

$A_R(0)$ , the unnormalized real part of the measured correlation function at zero lag, is an estimate of  $\sigma_b^2$  and may be used to normalize the estimates at all other lags.

#### 1. Normalization of Real Part of Correlation Function

In Mode F only the real correlation function  $A_R(\tau)$  is measured, and the incoherent scatter correlation-function estimate is  $\hat{\rho}_R(\tau)$  where

$$\hat{\rho}_R(\tau) = \frac{A_R(\tau)}{A_R(0)} \quad (B-59)$$

The mean and variance of  $\hat{\rho}_R(\tau)$  are calculated using Eqs. (B-31) and (B-32), ignoring the covariance of  $A_R(\tau)$  and  $A_R(0)$ .

$$\langle \hat{\rho}_R(\tau) \rangle = \frac{\langle A_R(\tau) \rangle}{\langle A_R(0) \rangle} = \rho_{sR}(\tau) \quad (B-60)$$

$$\begin{aligned} \sigma_{\hat{\rho}_R}^2(\tau) &= \langle \hat{\rho}_R(\tau) \rangle^2 \left[ \frac{\sigma_{A_R(0)}^2}{\langle A_R(0) \rangle^2} + \frac{\sigma_{A_R(\tau)}^2}{\langle A_R(\tau) \rangle^2} \right] \\ &= \sigma_b^{-4} [\sigma_{A_R(\tau)}^2 + \rho_{sR}^2(\tau) \sigma_{A_R(0)}^2] \end{aligned} \quad (B-61)$$

Note that as  $\rho_{sI}(\tau)$  and  $\rho_{nI}(\tau)$  are not estimated, we may take them as zero in the expressions for  $\sigma_{A_R(\tau)}^2$  and  $\sigma_{A_R(0)}^2$  [Eq. (B-51)].

## 2. Normalization When Complex Correlation Function Is Measured

In Modes G and H both real and imaginary correlations are measured, and the amplitude of the incoherent scatter correlation function may be estimated using

$$\hat{\rho}_A(\tau) = \frac{[A_R^2(\tau) + A_I^2(\tau)]^{1/2}}{A_R(0)} = \frac{B(\tau)}{A_R(0)} \quad (B-62)$$

The expectation and variance of  $\hat{\rho}_A(\tau)$  are

$$\langle \hat{\rho}_A(\tau) \rangle = [\rho_{sR}^2(\tau) + \rho_{sI}^2(\tau)]^{1/2} \quad (B-63)$$

$$\begin{aligned} \sigma_{\hat{\rho}_A}^2(\tau) &= \langle \hat{\rho}_A(\tau) \rangle^2 \left[ \frac{\sigma_{A_R(0)}^2}{\langle A_R(0) \rangle^2} + \frac{\sigma_{B(\tau)}^2}{\langle B(\tau) \rangle^2} \right] \\ &= \sigma_b^{-4} \{ \sigma_{B(\tau)}^2 + [\rho_{sR}^2(\tau) + \rho_{sI}^2(\tau)] \sigma_{A_R(0)}^2 \} \end{aligned} \quad (B-64)$$

## B. Normalization Using a Theoretical Function

In this case, we assume that a theoretical incoherent scatter correlation function  $\rho_t(\tau)$  is available. This would be the situation when searching through a library of theoretical functions to find the one which is the best fit to the measured function. This approach allows all the measured values of  $A_R(\tau)$ ,  $A_I(\tau)$  to play a part in determining the estimate of  $\sigma_b^2$  rather than just  $A_R(0)$ .

The theoretical function  $\rho_t(\tau)$  is for zero doppler shift and is wholly real.  $\rho_t(\tau)$  is used directly for F-Mode analysis, since imaginary correlations are not calculated and are assumed to be zero. For G- and H-Mode analysis, the complete theoretical function is  $|\rho_t(\tau)| e^{i\phi(\tau)}$ , where the amplitude is  $|\rho_t(\tau)|$  and phase is  $\phi(\tau)$ .

1. Normalization When Only Real Part of Correlation Function Is Measured

The estimate of  $\sigma_b^2$  is taken as the value "a" which minimizes the sum

$$\sum_i w_i [A_R(\tau_i) - a\rho_t(\tau_i)]^2 \quad . \quad (B-65)$$

The sum is over all measured values of  $\tau_i$ , and the weights  $w_i$  are proportional to  $\sigma_R^{-2}(\tau_i)$ . It is convenient to use

$$w_i = \frac{\sigma_b^4}{\sigma_R^2(\tau_i)}$$

which makes  $w_i$  independent of  $\sigma_b$  because  $\sigma_R^2(\tau_i)$  contains a term  $\sigma_b^4$ . Solving for "a,"

$$a = \frac{\sum w_i \rho_t(\tau_i) A_R(\tau_i)}{\sum w_i \rho_t^2(\tau_i)} \quad . \quad (B-66)$$

The expected value of a is given by

$$\begin{aligned} \langle a \rangle &= \frac{\sum w_i \rho_t(\tau_i) \langle A_R(\tau_i) \rangle}{\sum w_i \rho_t^2(\tau_i)} \\ &= \sigma_b^2 \frac{\sum w_i \rho_t(\tau_i) \rho_{sR}(\tau_i)}{\sum w_i \rho_t^2(\tau_i)} \\ &\approx \sigma_b^2 \quad \text{when } \rho_t(\tau_i) \approx \rho_{sR}(\tau_i) \quad . \end{aligned} \quad (B-67)$$

Thus, a is an unbiased estimate of  $\sigma_b^2$  if the theoretical function  $\rho_t$  is close to the true function  $\rho_{sR}$ , as will be assumed.

The variance of a is  $\sigma_a^2$

$$\begin{aligned} \sigma_a^2 &= \frac{\sum w_i^2 \rho_t^2(\tau_i) \sigma_R^2(\tau_i)}{\left[ \sum w_i \rho_t^2(\tau_i) \right]^2} \\ &= \frac{\sigma_b^4}{\sum w_i \rho_t^2(\tau_i)} \quad . \end{aligned} \quad (B-68)$$

Since a is an estimate of  $\sigma_b^2$ , the normalized autocorrelation function  $\check{\rho}_R(\tau_i)$  may be defined as

$$\check{\rho}_R(\tau_i) = \frac{A_R(\tau_i)}{a} \quad . \quad (B-69)$$

Expressions for the expectation and variance of  $\check{\rho}_R(\tau_i)$  are

$$\langle \check{\rho}_R(\tau_i) \rangle = \rho_{sR}(\tau_i) \quad (B-70)$$

$$\sigma_{\hat{\rho}_R}^2(\tau_i) = \sigma_b^{-4} \sigma_R^2(\tau_i) \left[ 1 - \frac{\rho_{sR}^2(\tau_i)}{\sigma_R^2(\tau_i) \sum_j \rho_{sR}^2(\tau_j) \sigma_R^{-2}(\tau_j)} \right] \quad (B-71)$$

The method of normalization using a theoretical function has an advantage in that it produces a small correlation between the statistical errors of different lags. This means that the parameters (such as ion or electron temperature or ion-neutral collision frequency) which characterize the best-fit theoretical function are more accurately determined (i.e., have smaller variances). Directly comparing the covariances for the estimates  $\hat{\rho}_R$  and  $\check{\rho}_R$  gives

$$\frac{\langle \hat{\rho}_R(\tau_i) - \rho_{sR}(\tau_i) \rangle \langle \hat{\rho}_R(\tau_j) - \rho_{sR}(\tau_j) \rangle}{\langle \check{\rho}_R(\tau_i) - \rho_{sR}(\tau_i) \rangle \langle \check{\rho}_R(\tau_j) - \rho_{sR}(\tau_j) \rangle} \approx 3\sigma_R^2(0) \sum_i \rho_{sR}^2 \sigma_R^{-2}(\tau_i) \quad (B-72)$$

Typically, the RHS of Eq. (B-72) is about 20, clearly making it more desirable to use  $\check{\rho}_R(\tau)$  in least-squares fitting than  $\hat{\rho}_R(\tau)$ .

## 2. Complete Correlation Function Measured

The method used is similar to that just described, except that  $B(\tau)$  is used instead of  $A_R(\tau)$ . The estimate of  $\sigma_b^2$  is the value which minimizes the sum

$$\sum_i w_i [B(\tau_i) - b |\rho_t(\tau_i)|]^2 \quad (B-73)$$

with

$$w_i = \frac{\sigma_b^2}{\sigma_B^2(\tau_i)} \quad (B-74)$$

As before,

$$b = \frac{\sum_i w_i |\rho_t(\tau_i)| B(\tau_i)}{\sum_i w_i \rho_t^2(\tau_i)}$$

and

$$\langle b \rangle \approx \sigma_b^2 \quad (B-75)$$

The normalized amplitude  $\check{\rho}_A(\tau_i)$  is defined as

$$\check{\rho}_A(\tau_i) = \frac{B(\tau_i)}{b} \quad (B-76)$$

and

$$\langle \check{\rho}_A(\tau_i) \rangle = \rho_{sA}(\tau_i) = [\rho_{sR}^2(\tau_i) + \rho_{sI}^2(\tau_i)]^{1/2} \quad (B-77)$$

$$\sigma_{\check{\rho}_A}^2(\tau_i) = \sigma_b^{-4} \sigma_B^2(\tau_i) \left[ 1 - \frac{\rho_{sA}^2(\tau_i)}{\sigma_B^2(\tau_i) \sum_j \rho_{sA}^2(\tau_j) \sigma_B^{-2}(\tau_j)} \right] \quad (B-78)$$

For the same reason as discussed in the last section, it is desirable to use  $\gamma_A$  instead of  $\hat{\rho}_A$  when deriving the best-fit theoretical function.

## X. ERROR IN PHASE OF CORRELATION FUNCTION

The phase of the complex correlation function measured in Modes G and H is

$$\phi(\tau) = \arctan \left[ \frac{A_I(\tau)}{A_R(\tau)} \right] \quad . \quad (\text{B-79})$$

The expectation and variance of  $\phi(\tau)$  are derived using the approximate Eqs. (B-31) and (B-32),

$$\langle \phi(\tau) \rangle = \arctan \left[ \frac{\rho_{SI}(\tau)}{\rho_{SR}(\tau)} \right] \quad (\text{B-80})$$

$$\begin{aligned} \sigma_\phi^2(\tau) = & \left[ \frac{\rho_{SI}^2(\tau)}{\rho_{SR}^2(\tau)} \right] \left[ \frac{\sigma_I^2(\tau)}{\rho_{SI}^2(\tau)} + \frac{\sigma_R^2(\tau)}{\rho_{SR}^2(\tau)} - \frac{2\sigma_{RI}(\tau)}{\rho_{SI}(\tau)\rho_{SR}(\tau)} \right] \\ & \times \left[ 1 + \frac{\rho_{SI}(\tau)^2}{\rho_{SR}(\tau)} \right]^{-2} \quad . \quad (\text{B-81}) \end{aligned}$$

## XI. ERROR IN DRIFT VELOCITY

The plasma drift velocity  $v_d$  is related to the phase  $\phi(\tau)$  of the incoherent scatter correlation function by

$$v_d = \frac{\lambda}{4\pi} \frac{d\phi}{d\tau} \quad (\text{B-82})$$

where  $\lambda$  is the transmitted wavelength. The G- and H-Mode experiments yield phase values  $\phi(\tau_i)$  at a number of lags  $\tau_i$  from which  $v_d$  may be estimated.

The estimate of  $d\phi/d\tau$  is the slope  $S$  of a straight line fitted to the measured phases in a weighted least-squares sense, i.e.,  $S$  is chosen to minimize

$$\sum_i W_i [\phi(\tau_i) - S\tau_i]^2 \quad (\text{B-83})$$

with  $W_i = \sigma_\phi^{-2}(\tau_i)$ .

The solution for  $S$  is

$$S = \frac{\sum_i W_i \tau_i \phi(\tau_i)}{\sum_i W_i \tau_i^2} \quad (\text{B-84})$$

and its variance  $\sigma_S^2$  is

$$\sigma_S^2 = \left( \sum_i W_i \tau_i^2 \right)^{-1} \quad . \quad (\text{B-85})$$



The drift velocity is estimated using

$$v_d = \frac{\lambda}{4\pi} S \quad (\text{B-86})$$

and its variance  $\sigma_v^2$  is given by

$$\sigma_v^2 = \frac{\lambda^2}{16\pi^2} \sigma_S^2 = \frac{\lambda^2}{16\pi^2} \left[ \sum_i \frac{\tau_i^2}{\sigma_\phi^2(\tau_i)} \right]^{-1} \quad (\text{B-87})$$

## XII. ERRORS IN ACCURACY OF PARAMETERS DETERMINED FROM LIBRARY REGRESSION ON A MEASURED CORRELATION FUNCTION

The magnitude of a measured correlation function is analyzed to determine two physical parameters -  $T_i$  and  $\nu_{in}$  in the lower E-region, and  $T_i$  and  $T_e/T_i$  at other altitudes. This section estimates the errors in these physical parameters according to the goodness-of-fit values obtained in the library regression. For generality, the derivations are given in terms of parameters  $x$  and  $y$  to be determined from data  $d(z_i)$  (measured correlation function) measured at discrete values of the independent variable  $z_i$  (lag  $\tau_i$ ) through comparison with a library of theoretical functions  $f(x, y, z_i)$  (theoretical incoherent scatter correlation functions).

In searching for the best estimates of  $x$  and  $y$ , the deviations between the measured and library functions are squared, weighted, and summed to yield the residual

$$\delta(x, y) = \sum_i W_i [f(x, y, z_i) - ad(z_i)]^2 \quad (\text{B-88})$$

where the weights  $W_i$  and normalization constant  $a$  are given in Sec. IX of this appendix. Next, a function of the form

$$q(x, y) = Ax^2 + By^2 + Cxy + Dx + Ey + F \quad (\text{B-89})$$

is fitted in a least-mean-squares sense to the values  $\delta(x, y)$ . The least-mean-squares estimates of  $x$  and  $y$  are the values  $\hat{x}$  and  $\hat{y}$  which produce a minimum in the function  $\delta(x, y)$ . By making reasonable assumptions, it is possible to estimate the statistical uncertainty in  $\hat{x}$  and  $\hat{y}$  in terms of the coefficients  $A$ ,  $B$ , and  $C$  in Eq. (B-89).

We assume that if  $x$  and  $y$  are given, a measured point  $d(z_i)$  will deviate from the true value  $f(x, y, z_i)$  by an amount  $\delta(z_i)$  which is normally distributed with standard deviation  $\sigma(z_i)$  and zero mean. We also assume that the error is independent of the errors in adjacent points. It follows that the probability of observing a given value  $d(z_i)$  for given  $x$  and  $y$  is

$$P [d(z_i) | x, y] = P [\delta(z_i) | x, y] \propto \exp \left[ \frac{-\delta^2(z_i)}{2\sigma^2(z_i)} \right] \quad (\text{B-90})$$

The joint probability of observing a complete (autocorrelation) function  $d(z)$  given  $x$  and  $y$  is the product of these individual probabilities, viz:-

$$P [d(z) | x, y] \propto \exp \left[ -\sum_i \delta^2(z_i) / 2\sigma^2(z_i) \right] \quad (\text{B-91})$$

If we make various hypotheses regarding the values of  $x$  and  $y$ , Eq. (B-91) gives the resulting probabilities of obtaining the result  $d(z)$ . However, what we really want is the function  $P[x, y|d(z)]$ , which is the probability that  $x, y$  are the correct values given the observed function  $d(z)$ . We have

$$P[x, y|d(z)] = \frac{P(x, y)}{P[d(z)]} P[d(z)|x, y] \quad (B-92)$$

The a priori probability  $P(x, y)$  is essentially unknown, and the best that can be done is to consider all hypotheses as to the true values of  $x, y$  to be equally likely.  $P[d(z)]$  is a constant, independent of  $x, y$ . Thus,

$$P[x, y|d(z)] \approx K e^{-\delta(x, y)/2} \quad (B-93)$$

where  $K$  is a constant.

From Eq. (B-93), we see that the least-squares estimates  $\hat{x}$  and  $\hat{y}$  which minimize  $\delta(x, y)$  also maximize  $P[x, y|d(z)]$ . Thus,  $\hat{x}, \hat{y}$  are identical to the maximum-likelihood estimates of  $x$  and  $y$ .

The exact form of the function  $P[x, y|d(z)]$  is difficult to determine, so the simple assumption is made that it is a bivariate normal distribution in the variables  $x, y$ . The means are taken as  $\hat{x}$  and  $\hat{y}$ , the variances as  $\sigma_x^2$  and  $\sigma_y^2$ , and the correlation coefficient as  $\sigma_{xy}$ . Thus,

$$P[x, y|d(z)] \propto \exp\left\{-\frac{1}{2(1-\sigma_{xy}^2)} \left[ \left(\frac{x-\hat{x}}{\sigma_x}\right)^2 + \left(\frac{y-\hat{y}}{\sigma_y}\right)^2 - \frac{2\sigma_{xy}(x-\hat{x})(y-\hat{y})}{\sigma_x\sigma_y} \right]\right\} \quad (B-94)$$

and, from Eq. (B-93),

$$\delta(x, y) = \frac{(x-\hat{x})^2}{(1-\sigma_{xy}^2)\sigma_x^2} + \frac{(y-\hat{y})^2}{(1-\sigma_{xy}^2)\sigma_y^2} - \frac{2\sigma_{xy}(x-\hat{x})(y-\hat{y})}{(1-\sigma_{xy}^2)\sigma_x\sigma_y} + \text{constant} \quad (B-95)$$

From the fit [Eq. (B-89)] to  $\delta(x, y)$ , it follows that

$$\begin{aligned} \sigma_x &= \left(\frac{4B}{4AB - C^2}\right)^{1/2} \\ \sigma_y &= \left(\frac{4A}{4AB - C^2}\right)^{1/2} \\ \sigma_{xy} &= \frac{-C}{\sqrt{4AB}} \end{aligned}$$

### XIII. ESTIMATION OF THE ERROR INTRODUCED INTO THE F-MODE CORRELATION FUNCTIONS BY CLUTTER ECHOES

#### A. Introduction

Clutter returns are removed through digital filtering, as explained in the main text in Secs. II-A, III-A, IV-B, and IV-C and as indicated by Eqs. (16) and (25). It has been found, in practice, that points that exhibit a large clutter-to-signal ratio often depart considerably from the expected autocorrelation function by an amount not explained by the statistics of the clutter subtraction algorithm. Accordingly, it seems appropriate to give these points less weight than

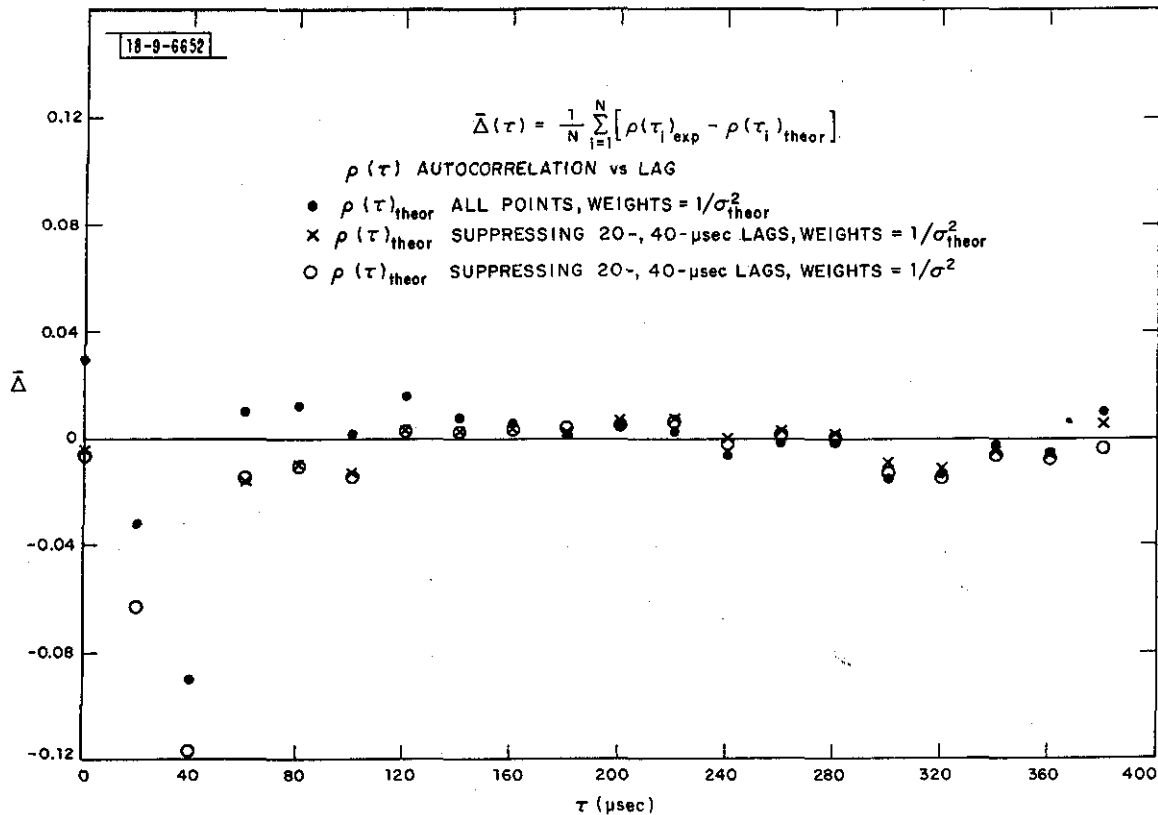


Fig. B-1. Comparison of experimental autocorrelation function and its best-fit theoretical function – average difference vs lag; 14 April 1971,  $c/s < 0.5$ .

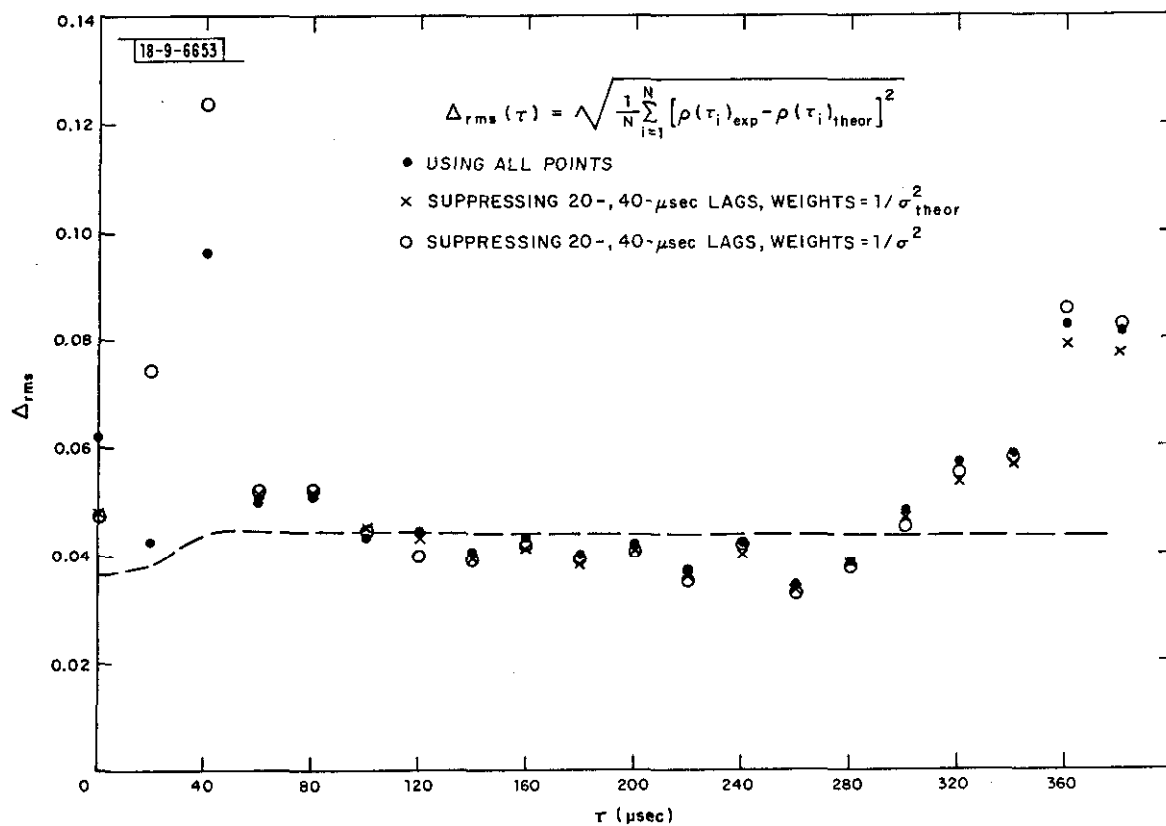


Fig. B-2. Comparison of experimental autocorrelation function and its best-fit theoretical function – rms difference vs lag; 14 April 1971,  $c/s < 0.5$ .

one would otherwise assign to them when matching the observations to theoretical functions. This section outlines the manner in which the appropriate weights are established.

### B. Experimental Study

In order to derive proper weights for the least-squares fit of theoretical to experimental autocorrelation functions in Mode F, the observed correlations on four sample days in 1971 were studied in some detail. The analysis was limited to altitudes below 125 km.

Statistical errors in Mode F autocorrelation functions were estimated theoretically taking account of noise, self-clutter, and a d-c clutter contribution according to Eq. (B-51). However, all points with a clutter-to-signal ratio  $c/s$  of  $\geq 0.5$  were ignored. Using theoretical functions derived in this way, the random and systematic deviations between the theoretical and experimental autocorrelation functions were examined for all points, including those for which  $c/s$  exceeded the threshold value of 0.5.

Figure B-1 shows the mean deviation between the theoretical and experimental points as a function of time lag. Only points where  $c/s < 0.5$  were used in the least-squares fit. An average of 120 points was used at each lag. It is evident that the point at  $\tau = 20 \mu\text{sec}$  and particularly that at  $\tau = 40 \mu\text{sec}$  are systematically too low. The reason for this discrepancy is probably that the actual transmitted pulse shape departs from the perfect square pulse assumed, especially for  $\tau = 40 \mu\text{sec}$  (see Appendix A). A revised fit eliminating the 20- and 40- $\mu\text{sec}$  points shows an average deviation that is generally less than 0.01, indicating that major systematic errors have now been removed for the case when  $c/s < 0.5$ .

The rms difference  $\Delta_{\text{rms}}$  between the experimental and theoretical autocorrelation functions is shown in Fig. B-2 for the same data as in Fig. B-1. Since only points with relatively small  $c/s$  were used,  $\Delta_{\text{rms}}$  is close to the expected value  $\sigma_{\text{theor}}$ , at least for lags shorter than 300  $\mu\text{sec}$ .

The effects of clutter were then obtained by comparing the experimental and theoretical autocorrelation functions. Figure B-3 shows the average deviation calculated as a function of  $c/s$ . The latter parameter was quantized in the following ranges: 0 to 0.2, 0.2 to 0.4, 0.4 to 0.6, 0.6 to 0.8, 0.8 to 1, 1 to 1.5, 1.5 to 2, 2.5 to 3,  $>3$ . A systematic deviation is apparent at  $c/s > 2$ . For the four days studied, the number of samples with  $c/s > 2$  is about 2 percent of the total points. Thus, the effects of systematic errors for  $c/s > 2$  could be removed by eliminating all these points from the fit. The rms deviation as a function of  $c/s$  is shown in Fig. B-4 and is compared with  $\sigma_{\text{theor}}$ . As expected,  $\Delta_{\text{rms}}$  is close to  $\sigma_{\text{theor}}$  for small  $c/s$ . A roughly linear relationship is seen to exist between  $\Delta_{\text{rms}}$  and  $c/s$ , indicating that a simple empirical model will suffice to estimate the additional statistical error introduced by clutter.

### C. Results

The variance in the measured autocorrelation points due to clutter is defined as

$$\sigma_c^2 = \Delta_{\text{rms}}^2 - \sigma_{\text{theor}}^2 \quad . \quad (\text{B-96})$$

Four days of measurements were used in deriving the empirical relationship between  $\sigma_c^2$  and  $c/s$ . Figure B-5 shows the data points on each day, and the average over all days. The straight line fitted to the data gives the empirical relationship

$$\sigma_c^2(\tau) = 0.013 \quad (c/s) \quad . \quad (\text{B-97})$$

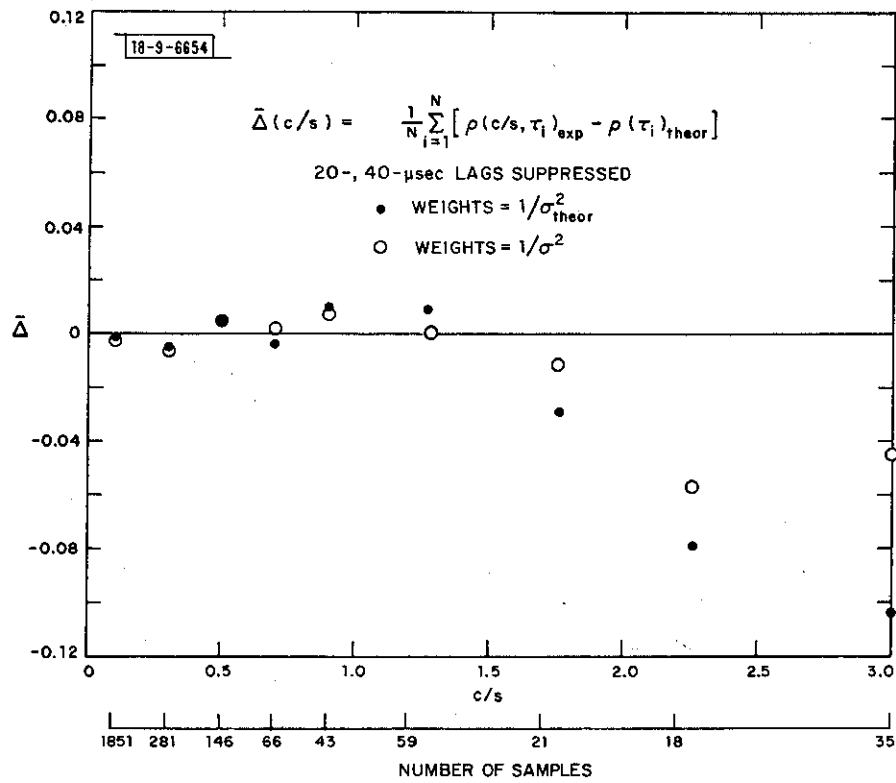


Fig. B-3. Comparison of experimental autocorrelation function and its best-fit theoretical function – average difference vs c/s, 14 April 1971.

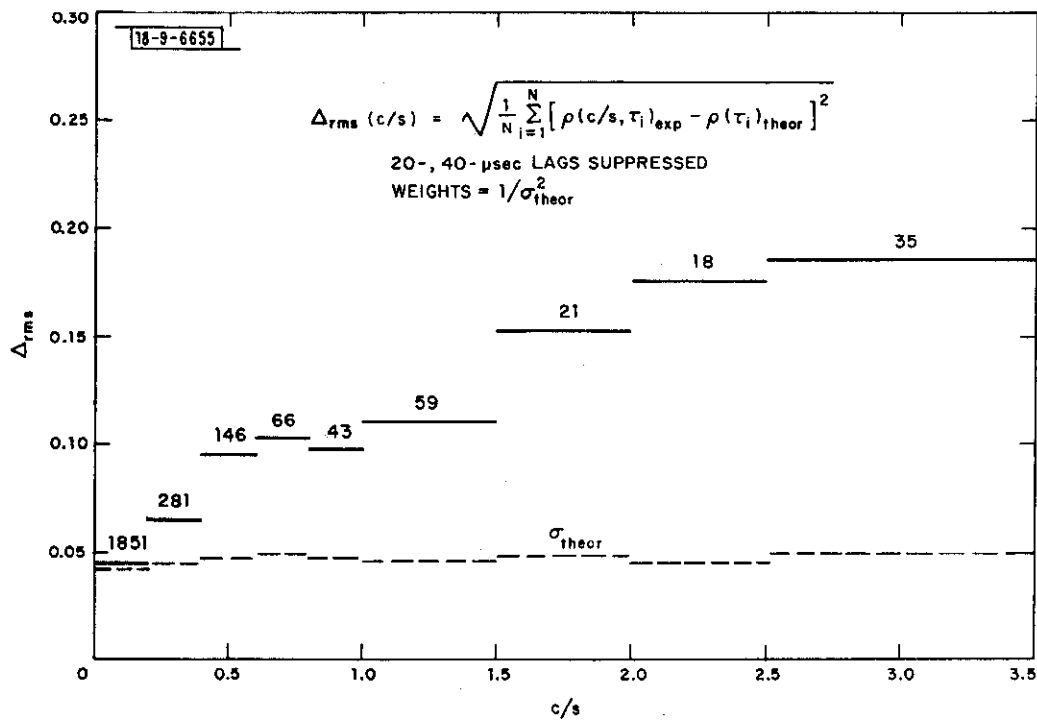


Fig. B-4. Comparison of experimental autocorrelation function and its best-fit theoretical function – rms difference vs c/s, 14 April 1971.

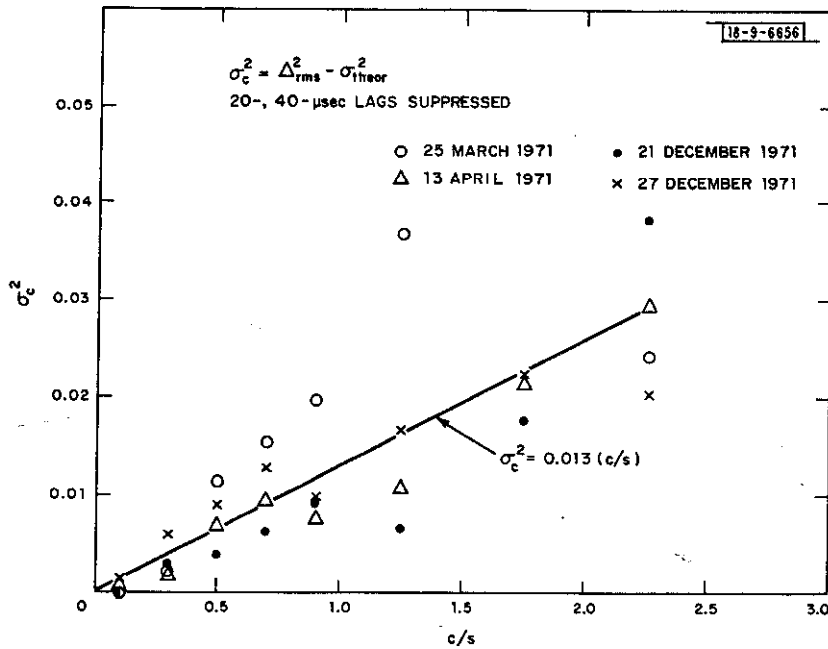


Fig. B-5. Comparison of experimental autocorrelation function and its best-fit theoretical function - variance increase vs  $c/s$ .

Thus, the total error in the autocorrelation function as a function of lag is given by

$$\sigma^2(\tau) = \sigma_{theor}^2(\tau) + \sigma_c^2(\tau) \quad (B-98)$$

where  $\sigma_{theor}^2$  is given by Eq. (B-51) and  $\sigma_c^2$  is given by Eq. (B-97).

Based on the foregoing, it was decided to weight the F-Mode correlation function points by  $1/\sigma^2(\tau)$  instead of  $1/\sigma_{theor}^2(\tau)$ . Also, the 20- and 40- $\mu$ sec lags were omitted from consideration. The elimination of points  $c/s > 2$ , while probably desirable, was not implemented.

<b>BIBLIOGRAPHIC DATA SHEET</b>		1. Report No.	3. Recipient's Accession No.
4. Title and Subtitle Incoherent Scatter Measurements of E- and F-Region Density, Temperatures, and Collision Frequency at Millstone Hill			5. Report Date 23 February 1979
			6.
7. Author(s)	William L. Oliver Ronald H. Wand	Joseph E. Salah John V. Evans	8. Performing Organization Rept. No. Technical Report 531
9. Performing Organization Name and Address Lincoln Laboratory, M. I. T. P.O. Box 73 Lexington, MA 02173			10. Project/Task/Work Unit No.
			11. Contract/Grant No. ATM 75-22193
12. Sponsoring Organization Name and Address National Science Foundation Atmospheric Science Section Washington, DC 20550			13. Type of Report & Period Covered Technical Report
			14.
15. Supplementary Notes			
16. Abstracts  The Millstone Hill incoherent (Thomson) scatter radar system has been operated since 1963 to perform a synoptic study of F2-region electron densities, and electron and ion temperatures. These measurements have been conducted by transmitting single long pulses and performing digital sweep integration and spectrum analysis of the reflected signals. This report describes changes made to the system in 1969 to permit extensions of the measurements to altitudes below 200 km (i.e., the E- and F1-regions). These changes include modifications to the radar timing equipment to permit the transmission of close-spaced pairs of pulses from which the echo autocorrelation function can be determined in the computer by processing appropriately spaced pairs of echo samples. By operating the radar coherently, it has also been possible to subtract the unwanted (stronger) clutter signals from the ionospheric echoes. Samples are presented of the results that can now be obtained from these programs.			
17. Key Words and Document Analysis. 17a. Descriptors Millstone radar E-region F-region diurnal variations electron density ionospheric scatter seasonal variations temperature effects spectrum analyzers			
7b. Identifiers/Open-Ended Terms			
17c. COSATI Field/Group			
18. Availability Statement		19.. Security Class (This Report) U N -	21. No. of Pages 108
		% Security Class (This Page) UNCLASSIFIED	22. Price